The Effect of Quantum-Well Superlattices on the Thermoelectric Figure of Merit

by

Lyndon D. Hicks

B.A., University of Cambridge (1991)
M.A., University of Cambridge (1995)

Submitted to the Department of Physics
in partial fulfillment of the requirements for the degree of

Doctor of Philosophy

at the

MASSACHUSETTS INSTITUTE OF TECHNOLOGY

June 1996

Author ....
Department of Physics
May 1, 1996

Certified by ....
Mildred S. Dresselhaus
Institute Professor
Thesis Supervisor

Accepted by ....
George F. Koster
Chairman, Departmental Committee on Graduate Students

The Effect of Quantum-Well Superlattices on the Thermoelectric Figure of Merit

by

Lyndon D. Hicks

Submitted to the Department of Physics
on May 1, 1996, in partial fulfillment of the
requirements for the degree of
Doctor of Philosophy

Abstract

The thermoelectric figure of merit (Z) is a measure of the usefulness of a material for thermoelectric cooling applications. Presently, the materials with the highest Z are Bi_2Te_3 alloys, with a ZT of 1.0 at $T = 300$ K. Since the 1960s, only slow progress has been made in enhancing Z, either in Bi_2Te_3 alloys or in other thermoelectric materials. So far, all the materials used in applications have been in bulk form. In this thesis, I propose that it may be possible to increase Z in certain materials by preparing them in the form of two-dimensional (2D) quantum-well superlattices. I have done calculations to investigate the potential for such an approach. The calculations show that layering has the potential to increase significantly the Z of a material over its bulk value, and values of Z much higher than the bulk Bi_2Te_3 alloys should be achievable. In addition to improving the Z of good bulk thermoelectric materials, layering may also result in a high Z for some two-band or mixed conduction materials which have a very low Z in bulk form because the electron and hole contributions to the Seebeck coefficient have opposite signs. This result allows the possibility of using a new class of materials as thermoelectric refrigeration elements. Calculations were also done for one-dimensional (1D) materials and they show that 1D materials such as quantum wires may also achieve a high Z, higher than 2D quantum-well superlattices. In order to verify my theoretical predictions experimentally, I did an experimental investigation using $PbTe/Pb_{1-x}Eu_xTe$ quantum-well superlattices grown by molecular beam epitaxy. Thermoelectric and other transport measurements were done as a function of quantum-well thickness and doping. The results were found to be consistent with the theoretical predictions and indicate a significant enhancement of Z within the quantum wells over bulk 3D values. The experimental results further indicate that an increase in Z over the best bulk values may be possible through quantum confinement effects using quantum-well superlattices.

Thesis Supervisor: Mildred S. Dresselhaus
Title: Institute Professor

Acknowledgments

My five years here at M.I.T. have been among the most enjoyable and exciting times of my life. It is rare that one has an opportunity to work on a project just because it is interesting, with few external constraints or restrictions. It is even rarer to have that project open up an important new field of research, a field that can only grow for years to come. That is what happened to me at M.I.T., and I am extremely grateful to the people who helped make it happen.

First I would I like to thank my supervisor Prof. Mildred Dresselhaus for giving me the opportunity to work on this project, for letting me have free rein while things were going well, for being patient and offering sound scientific advice when things were going slow, and for working tirelessly behind the scenes on my behalf to make sure I got the most out my research. She has the most energy and works harder than any person that I have ever known, preferring to lead by example rather than by command.

My thesis research would not have been half as successful without the outstanding contribution of Dr. Ted Harman of M.I.T. Lincoln Laboratory. Dr. Harman must take all the credit for the success of the experimental side of my thesis. His contribution was substantial and invaluable, from his growth of samples of the highest quality to his help with the experimental measurements. I feel extremely fortunate and privileged to have worked with Dr. Harman, one of the true giants of thermoelectricity in the modern era.

Unlimited thanks goes to my dear wife Junko. Her companionship and patience helped me maintain my sense of balance and perspective during the sometimes turbulent days of research at M.I.T. Even when my work was not going well, I would never lose heart since I could always count on returning home to see her at the end of the day.

I would also like to thank my parents and my brother Damien for their support and encouragement, even while sometimes living halfway around the world.

A good part of the fun of being here at M.I.T. was the Dresselhaus group. Joey

Wang and Paul Nguyen were the first people I got to know in the group and I have continued to be good friends with both of them even after they left M.I.T. Joey was always there to provide useful experimental advice, both while he was still a postdoc here and afterwards when he worked at the Magnet Lab. Paul is one of the funniest and wackiest guys I know. Alex Fung was my officemate for most of my stay here, and we always had a great time talking about the NFL and NBA. Boris Pevzner shared my healthy skepticism for certain things in life, and Ibo Matthews was always keeping me on my toes by asking me questions on all things physics. Xiangzhong Sun helped me with some of my thermoelectric experiments and I wish him the best of luck in continuing my research. Nathan Belk, Siegfried Fleischer, James Chen, Gillian Reynolds, Sandra Brown and Ching-Hwa Kiang were all great to be around. I am grateful to Laura Doughty for everything she has done for me, especially for making sure that I got all my money back from credit card companies. Gene Dresselhaus always had plenty of challenging and interesting computer problems for me to solve, and I thank him for training me well for the future!

Others who have been helpful to me during my stay at M.I.T. are Jagadeesh Moodera for helpful experimental suggestions and for letting me have a taste of thin film growth in my first summer here, Jean-Paul Issi for technical tips, Peggy Berkovitz for taking care of all the Physics Department administrative issues, and United States Navy, in particular Charlie Hogg, for providing generous funding and support throughout my 4 years of research.

Contents

List of Figures

List of Tables

Chapter 1

Introduction to Thermoelectricity

1.1 Thermoelectric Effects

1.1.1 The Seebeck Effect

When a temperature gradient is maintained in a material and no electric current is allowed to flow, there will be a steady-state electrostatic potential difference between the high- and low-temperature regions of the specimen. The potential difference ΔV arises from the diffusion of charge carriers from the high- to low-temperature regions, and is directly proportional to the temperature difference ΔT.

$$\Delta V = -S\Delta T. \tag{1.1}$$

The constant of proportionality S is known as the Seebeck coefficient or thermoelectric power of the material. This effect was discovered by Thomas Seebeck in 1821.

1.1.2 The Peltier Effect

If an electric current is driven in a circuit of two dissimilar materials that is maintained at a uniform temperature, then heat will be evolved at one junction and absorbed at the other (Fig. 1-1). This is because an isothermal electric current (I) in a material

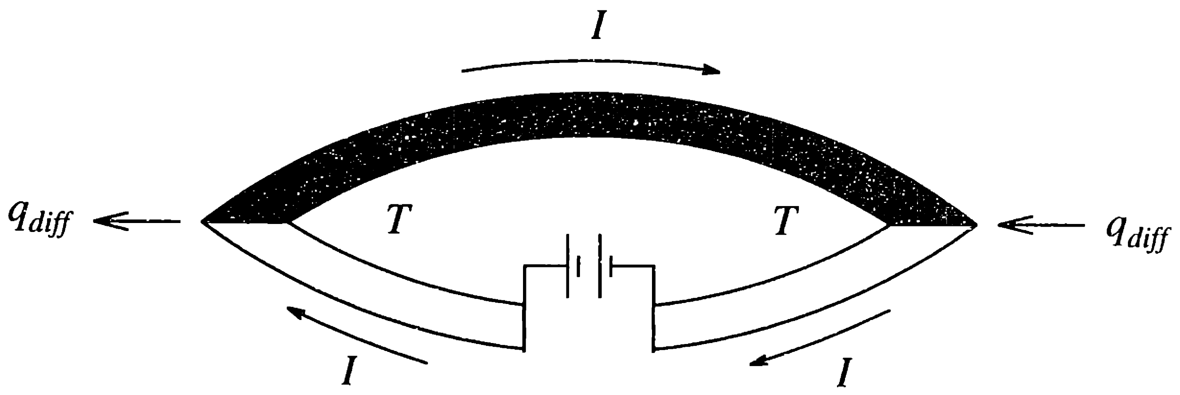

Figure 1-1: The Peltier Effect. A current I flows in a circuit of two dissimilar materials at uniform temperature T. Thermal current q_{diff} is evolved at one junction and supplied at the other.

is accompanied by a thermal current,

$$q = \Pi I, \tag{1.2}$$

where Π is known as the Peltier coefficient. Because the electric current is uniform in the closed circuit and the Peltier coefficient differs from material to material, the thermal current in the two materials will not be equal, and the difference in thermal current q_{diff} must be evolved at one junction and supplied to the other (as shown in Fig. 1-1) if the uniform temperature is to be maintained. This effect was discovered by Jean Peltier in 1834. One of the most common applications of the Peltier effect is the thermocouple, which is used to measure temperature differences.

The application of the theory of thermodynamics [1] leads to the following relation between the Seebeck and Peltier coefficients:

$$\Pi = ST, \tag{1.3}$$

where T is the absolute temperature.

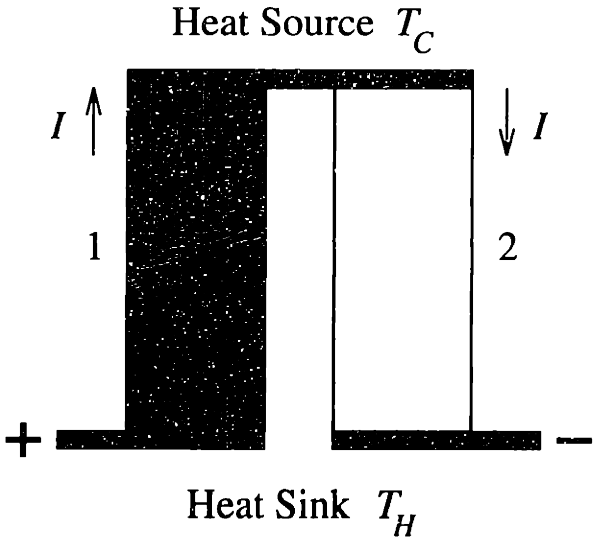

Figure 1-2: Simple thermoelectric refrigerator.

1.2 Theory of Thermoelectric Refrigeration

This section is summarized from chapter 1 of Ref. [2], an excellent book on thermoelectricity. Figure 1-2 shows a simple thermoelectric refrigerator, which consists of a thermocouple with branches having the parameters S_1, σ_1, κ_1 and S_2, σ_2, κ_2, respectively, where S is the Seebeck coefficient, σ is the electrical conductivity and κ is the thermal conductivity. The branches have constant cross-sectional areas A_1 and A_2 and are of length l_1 and l_2. They are joined by a link of zero electrical resistance at the heat source and by a source of emf, which produces a current I at the heat sink. The temperatures of the source and sink are T_C and T_H, respectively. It is assumed that there is no heat transfer to or from the surroundings other than at the source or the sink.

We wish to calculate the coefficient of performance for a given temperature difference between the hot and cold junctions. The coefficient of performance is defined as the ratio of the rate of cooling of the heat source to the rate of expenditure of electrical energy. Another quantity of interest is the maximum temperature difference that can be achieved when no heat has to be extracted from the source.

The rate of heat flow q_i within one of the conductors $i (i = 1 \text{ or } 2)$ at a distance

x from the heat source is given by

$$q_i = \mp S_i IT - \kappa A_i \frac{dT}{dx} \tag{1.4}$$

where T is the absolute temperature at x and the Peltier heat flow ΠI has been expressed as $S_i IT$ using Eq. (1.3). The $\mp$ sign occurs because the electric current I is taken to flow in the -x direction in branch 1, and in the $+x$ direction in branch 2. The rate of heat generation per unit length due to Joule heating is given by

$$\frac{I^2}{\sigma_i A_i} = -\kappa_i A_i \frac{d^2T}{dx^2}. \tag{1.5}$$

It is noted that the thermoelectric effects are not involved in this equation since the rate of change of Peltier heat flow along the conductor is just equal to the rate of working against the Seebeck emf.

Equation (1.5) must be solved with the boundary conditions $(T = T_C)_{x=0}$ and $(T = T_H)_{x=l}$, where l is the length of a branch. Thus it is found that

$$q_i = \frac{I^2[x - (l/2)]}{\sigma_i A_i} - \frac{\kappa_i A_i (T_H - T_C)}{l}. \tag{1.6}$$

The cooling power q_C at the heat source is the sum of the contributions q_1 and q_2 at $x = 0$. Remembering that the current flow is in opposite directions in the two branches (it is assumed that it is in the correct sense to give cooling rather than heating of the source and that $S_2 > S_1$)

$$q_C = (S_2 - S_1)IT_C - \frac{I^2R}{2} - K(T_H - T_C), \tag{1.7}$$

where

$$R = \frac{l_1}{A_1\sigma_1} + \frac{l_2}{A_2\sigma_2} \tag{1.8}$$

is the total electrical resistance of the branches in series and

$$K = \frac{A_1\kappa_1}{l_1} + \frac{A_2\kappa_2}{l_2} \tag{1.9}$$

is the total thermal conductance of the branches in parallel.

The overall rate of expenditure of electrical energy in one branch is given by

$$w_i = \pm \int_{T_C}^{T_H} S_i I dT + \int_0^{l_i} \frac{I^2}{\sigma_i A_i} dx = \mp S_i I (T_H - T_C) + \frac{I^2 l_i}{\sigma_i A_i}. \tag{1.10}$$

Thus for both branches

$$w = (S_2 - S_1) I (T_H - T_C) + I^2 R \tag{1.11}$$

Here we have assumed that S_i and σ_i are temperature-independent for the range T_C to T_H. This is sufficient for the purpose of obtaining criteria for the selection of good thermoelectric materials [2].

The coefficient of performance ϕ equal to q_C/w is found from Eqs. (1.7) and (1.11):

$$\phi = \frac{(S_2 - S_1) I T_C - I^2 R/2 - K(T_H - T_C)}{(S_2 - S_1) I (T_H - T_C) + I^2 R}. \tag{1.12}$$

The electric current I_q for maximum cooling power is obtained by making dq_C/dI in Eq. (1.7) equal to zero. It is then found that

$$I_q = \frac{(S_2 - S_1) T_C}{R} \tag{1.13}$$

and the corresponding coefficient of performance is

$$\phi = \frac{\frac{1}{2} Z T_C^2 - (T_H - T_C)}{Z T_H T_C}, \tag{1.14}$$

where

$$Z = \frac{(S_2 - S_1)^2}{KR}. \tag{1.15}$$

If the heat source is removed, the coefficient of performance falls to zero and the temperature difference rises until

$$(T_H - T_C)_{max} = \frac{1}{2} Z T_C^2. \tag{1.16}$$

Since the quantity Z controls both the maximum temperature difference according to Eq. (1.16) and the coefficient of performance according to Eq. (1.14), it is called the figure of merit of the device.

For a given pair of branch materials, there is a maximum value of Z when the dimensions of the branches are optimized. It can be easily shown that this occurs when

$$\left(\frac{A_1/l_1}{A_2/l_2}\right)_{opt} = \sqrt{\frac{\sigma_2\kappa_2}{\sigma_1\kappa_1}}. \tag{1.17}$$

When the dimensions are optimized using Eq. (1.17), the figure of merit becomes

$$Z = \frac{(S_2 - S_1)^2}{[(\kappa_1/\sigma_1)^{1/2} + (\kappa_2/\sigma_2)^{1/2}]^2}. \tag{1.18}$$

Although the overall Z of a cooling device depends on the properties of the materials in both branches, it is useful to have a measure of the usefulness of a given material for one branch. In practice, in the region of room temperature, advances in positive and negative thermoelectric materials have been made at more or less the same rate, i.e. the values of S_2 and $-S_1$, and of σ_1/κ_1 and σ_2/κ_2 have been almost equal to each other. Under these conditions, it is legitimate to use figures of merit Z_1 and Z_2 for the two branches, where

$$Z_i = \frac{S_i^2\sigma_i}{\kappa_i} \tag{1.19}$$

since

$$Z \simeq \frac{z_1 + z_2}{2} \tag{1.20}$$

Equation (1.19) is the definition of the thermoelectric figure of merit of a material.

1.3 The Thermoelectric Figure of Merit

For a material to be good thermoelectric cooler, it must have a high thermoelectric figure of merit

$$Z = \frac{S^2 \sigma}{\kappa} \tag{1.21}$$

where S is the thermoelectric power (Seebeck coefficient), σ is the electrical conductivity, and κ is the thermal conductivity.

For a material to have a high Z, one requires a high thermoelectric power, S, a high electrical conductivity, σ, and a low thermal conductivity, κ. It is difficult to improve Z in actual systems for the following reasons. Increasing the thermoelectric power S for simple materials also leads to a simultaneous decrease in the electrical conductivity, as will be shown later. Also, an increase in the electrical conductivity leads to a comparable increase in the electronic contribution to the thermal conductivity because of the Wiedemann-Franz law. So with known conventional solids, a limit is rapidly obtained where a modification to any one of these parameters adversely affects the other transport coefficients so that the resulting Z for a given material at a given temperature does not vary significantly. Presently, the materials with the highest Z are isoelectronic Bi_2Te_3 alloys such as $Bi_{0.5}Sb_{1.5}Te_3$, with $ZT \simeq 1.0$ at 300 K [2]. Only a small increase (10%) [3] in Z has been achieved in the last three decades, so it is now felt that the Bi_2Te_3 compounds may be nearing the limit of their potential performance.

In this thesis, I propose that it may be possible to increase Z of some materials significantly by preparing them in the form of quantum-well superlattices. These structures may significantly alter Z since the electrons are now confined to move in 2 dimensions, changing the band structure and the electronic density of states (see Fig. 1-3). In addition to the density of states effect, the layering may reduce the phonon thermal conductivity and therefore increase Z as phonons can now be scattered by the interfaces between layers.

In the next chapter, general expressions for σ, S, κ are derived using the relaxation-time approximation. Chapters 3 onward describe the results of original theoretical

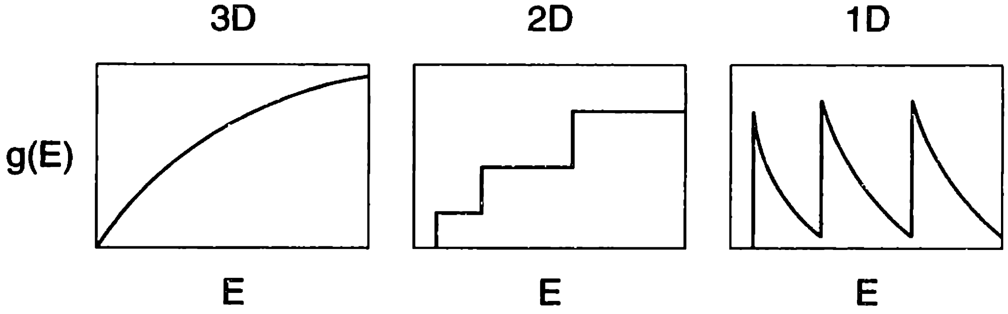

Figure 1-3: The density of states $g(E)$ for 3D, 2D and 1D systems.

and experimental work. The figure of merit is initially calculated for single-band, anisotropic 3D bulk materials. These expressions are then extended to transport in 2D quantum-well superlattices, 1D quantum wire systems, and to mixed conduction 2D systems including both electron and hole carriers. These transport results are then used to calculate values for Z in low-dimensional materials. The calculations show that reduced dimensionality has the potential to increase significantly (by factors of several) the figure of merit. The main reason for this increase is that in 2D, unlike in 3D, one is able to increase σ significantly without changing S. The Seebeck coefficient S is sensitive only to the position of the Fermi level, as described in Ref. [2] and as shown later. In 3D, one can increase the carrier density (and hence σ) only by increasing the Fermi level. This will reduce S as shown in Chapter 3. However, in 2D, because the electrons exist only in two dimensions, one can decrease the quantum well thickness (the 3rd dimension) and cause an increase in carrier density per unit volume without changing the Fermi level. Thus by decreasing the well width, one can increase σ while keeping S constant. In good thermoelectric materials such as semiconductors, since κ is dominated by the phonon contribution and is not affected significantly by the change in electron density, this increase in σ with constant S results in an increase in Z.[1] A similar effect occurs in 1D. This is just a largely hand-waving explanation for the increase in Z in 2D and is not intended to be deeply

---

[1] In practice, because of the finite electronic thermal conductivity, the Fermi level will need to be adjusted slightly as a function of well width to get the maximum Z; however, this does not change the basic effect just described.

analytical - one needs to read and follow the calculations in the next few chapters for a more rigorous understanding of the increase in Z in reduced dimensions.

The last chapter of the thesis describes an experimental investigation of a specific quantum-well superlattice system to test the theoretical predictions. The experimental results are found to be consistent with theory and indicate that quantum-well superlattices may indeed be used increase the thermoelectric figure of merit.

Chapter 2

General expressions for the thermoelectric coefficients

General expressions for S, σ, κ are derived using the relaxation-time approximation. Although the expressions shown are for 3D transport, they are derived in a form which will enable extension to 2D and 1D transport.

2.1 The Relaxation-Time Approximation

The relaxation-time approximation has been used to describe successfully the transport behavior of most metals and semiconductors in the region of room temperature. A detailed treatment can be found in Ref. [4]; a brief summary of that account is given here. The relaxation-time approximation assumes that given a nonequilibrium electron distribution function $g_n(\mathbf{r},\mathbf{k},t)$, such that $g_n(\mathbf{r},\mathbf{k},t)d\mathbf{r}d\mathbf{k}/4\pi^3$ is the number of electrons in the nth band at time t in the phase space volume $d\mathbf{r}d\mathbf{k}$, the distribution of those electrons that emerge from collisions into band n at $\mathbf{r},\mathbf{k}$, is given by

$$dg_n(\mathbf{r},\mathbf{k},t) = \frac{dt}{\tau_n(\mathbf{r},\mathbf{k})} g_n^0(\mathbf{r},\mathbf{k}), \tag{2.1}$$

where $\tau_n(\mathbf{r}, \mathbf{k})$ is defined as the relaxation time and

$$g_n^0(\mathbf{r}, \mathbf{k}) = f(\varepsilon) = \frac{1}{e^{(\varepsilon_n(\mathbf{k}) - \zeta(\mathbf{r}))/k_B T(\mathbf{r})} + 1} \tag{2.2}$$

is the equilibrium distribution Fermi function and ζ is the chemical potential. With this assumption, we can compute the nonequilibrium distribution function in the presence of external electric fields and temperature gradients.

2.2 Calculation of the nonequilibrium distribution function

Consider collisions at time $t' < t$. Using the relaxation-time approximation, it is possible to calculate the nonequilibrium function $g_n(\mathbf{r}, \mathbf{k}, t)$ at time t by an appropriate integration of Eq. (2.1) over t'. Only a fraction $P_n(\mathbf{r}, \mathbf{k}, t; t')$ (calculated below) of particles which suffer collisions at time t' survive until time t. Multiplying the right hand side of Eq. (2.1) by $P_n(\mathbf{r}, \mathbf{k}, t; t')$ and integrating over t' gives[1]

$$g(t) = \int_{-\infty}^{t} \frac{dt'}{\tau} g^0(t') P(t, t'). \tag{2.3}$$

The fraction of electrons that survive from t' to t is less than the fraction that survive from $t' + t$ by the factor $[1 - dt'/\tau]$, which is the probability of an electron colliding between t' and $t' + t$ from Eq. (2.1). Thus

$$P(t, t') = P(t, t' + dt') \left[1 - \frac{dt'}{\tau}\right]. \tag{2.4}$$

In the limit as $dt' \rightarrow 0$, this gives the differential equation

$$\frac{\partial}{\partial t'} P(t, t') = \frac{P(t, t')}{\tau}, \tag{2.5}$$

---

[1] The $\mathbf{r}, \mathbf{k}$ and n dependence of $g(t)$, τ and $P(t, t')$ are temporarily left implicit.

which can be solved to give

$$P(t,t') = e^{-(t-t')/\tau}. \tag{2.6}$$

We may use Eq. (2.5) to integrate Eq. (2.3) by parts, giving

$$g(t) = g^0(t) - \int_{-\infty}^{t} dt' P(t,t') \frac{d}{dt'} g^0(t'). \tag{2.7}$$

To evaluate the time derivative of g^0, note that g^0 in Eq. (2.2) depends on time only through $\varepsilon_n(\mathbf{k}_n(t'))$, $T(\mathbf{r}_n(t'))$, and $\zeta(\mathbf{r}_n(t'))$, so that

$$\frac{dg^0(t')}{dt'} = \frac{\partial g^0}{\partial \varepsilon_n}\frac{\partial \varepsilon_n}{\partial \mathbf{k}} \cdot \frac{d\mathbf{k}_n}{dt'} + \frac{\partial g^0}{\partial T}\frac{\partial T}{\partial \mathbf{r}} \cdot \frac{d\mathbf{r}_n}{dt'} + \frac{\partial g^0}{\partial \zeta}\frac{\partial \zeta}{\partial \mathbf{r}} \cdot \frac{d\mathbf{r}_n}{dt'}. \tag{2.8}$$

If we use the semiclassical equations of motion

$$\begin{aligned} \dot{\mathbf{r}}_n &= \mathbf{v}_n(\mathbf{k}) = \frac{1}{\hbar}\frac{\partial \varepsilon_n(\mathbf{k})}{\partial \mathbf{k}}, & (2.9) \\ \hbar\dot{\mathbf{k}}_n &= -e\mathbf{E}(\mathbf{r}_n, t'), & (2.10) \end{aligned}$$

in Eq. (2.8), where $\mathbf{E}$ is an external electric field, then Eq. (2.7) becomes

$$g(t) = g^0 + \int_{-\infty}^{t} dt' P(t,t') \left[\left(-\frac{\partial f}{\partial \varepsilon} \right) \mathbf{v} \cdot \left(-e\mathbf{E} - \nabla\zeta - \left(\frac{\varepsilon - \zeta}{T} \right) \nabla T \right) \right], \tag{2.11}$$

where f is the Fermi function (Eq. (2.2)).

If we assume a time-independent, spacially-uniform electric field and temperature gradient,[2] then the only t' dependence in the integrand in Eq. (2.11) is in $P(t,t') = e^{-(t-t')/\tau}$. Thus Eq. (2.11) can be integrated to give

$$g(\mathbf{k}) = g^0(\mathbf{k}) + \tau(\mathbf{k}) \left(-\frac{\partial f}{\partial \varepsilon} \right) \mathbf{v}(\mathbf{k}) \cdot \left[-e \left(\mathbf{E} + \frac{\nabla\zeta}{e} \right) + \frac{\varepsilon(\mathbf{k}) - \zeta}{T} (-\nabla T) \right], \tag{2.12}$$

Equation (2.12) is the nonequilibrium distribution function which will be used to calculate all the thermoelectric quantities. Note that in this general form, it can be

---

[2] All the thermoelectric measurements done in this investigation were d.c. measurements in zero magnetic field, so these assumptions are valid.

applied to transport in any number of spacial dimensions. It will first be used to calculate thermoelectric quantities in 3D bulk transport.

2.3 D.C. Electrical Conductivity

The number of electrons per unit volume in the volume element $d\mathbf{k}$ is $g(\mathbf{k})d\mathbf{k}/4\pi^3$, so the current density in a band is

$$\mathbf{j} = -e\int \frac{d\mathbf{k}}{4\pi^3}\mathbf{v}(\mathbf{k})g(\mathbf{k}). \tag{2.13}$$

Each partially filled band makes a contribution to the the current density. The total current density is the sum of these contributions over all bands. At uniform temperature, $\mathbf{j} = \boldsymbol{\sigma}\mathbf{E}$, where the conductivity tensor $\boldsymbol{\sigma}$ is a sum of contributions from each band. So from Eq. (2.12) and Eq. (2.13),[3]

$$\boldsymbol{\sigma} = \sum_n \boldsymbol{\sigma}^{(n)}, \tag{2.14}$$

$$\boldsymbol{\sigma}^{(n)} = e^2\int \frac{d\mathbf{k}}{4\pi^3}\tau_n(\mathbf{k})\mathbf{v}_n(\mathbf{k})\mathbf{v}_n(\mathbf{k})\left(-\frac{\partial f}{\partial \varepsilon}\right)_{\varepsilon=\varepsilon_n(\mathbf{k})}. \tag{2.15}$$

Note that since no current flows in equilibrium, g^0 makes no contribution to $\mathbf{j}$.

2.4 Seebeck Coefficient

From Eq. (2.12) and Eq. (2.13), when there is an electric field $\mathbf{E}$ and a temperature gradient ∇T in a material, there will in general be an electric current density in a band of

$$\mathbf{j} = \mathbf{L}^{11}(\mathbf{E} + \frac{\nabla\zeta}{e}) + \mathbf{L}^{12}(-\nabla T), \tag{2.16}$$

---

[3] Since T is constant, the local electronic density will be constant and hence $\nabla\zeta = 0$.

where the tensors $\mathbf{L}^{ij}$ are

$$\mathbf{L}^{11} = e^2 \int \frac{d\mathbf{k}}{4\pi^3} \left(-\frac{\partial f}{\partial \varepsilon}\right) \tau(\mathbf{k})\mathbf{v}(\mathbf{k})\mathbf{v}(\mathbf{k}), \tag{2.17}$$

$$\mathbf{L}^{12} = \left(-\frac{1}{eT}\right) e^2 \int \frac{d\mathbf{k}}{4\pi^3} \left(-\frac{\partial f}{\partial \varepsilon}\right) \tau(\mathbf{k})\mathbf{v}(\mathbf{k})\mathbf{v}(\mathbf{k})(\varepsilon(\mathbf{k}) - \zeta). \tag{2.18}$$

From Eq. (1.1), the Seebeck coefficient (S) is defined as

$$\Delta V = -S\Delta T. \tag{2.19}$$

when no electric current is allowed to flow. This can also be written as

$$\nabla V = -(\mathbf{E} + \frac{\nabla\zeta}{e}) = S(-\nabla T). \tag{2.20}$$

Since there is no electric current, Eq. (2.16) gives

$$S = \frac{L^{12}}{L^{11}} \tag{2.21}$$

For simplicity, we have taken ∇V and ∇T to be along a principal axis direction x, so that L^{11} and L^{12} are actually the xx components of the tensors $\mathbf{L}^{11}$ and $\mathbf{L}^{12}$, respectively. In general, S will be a tensor

$$\mathbf{S} = (\mathbf{L}^{11})^{-1}\mathbf{L}^{12} \tag{2.22}$$

2.5 Electronic Thermal Conductivity

The electronic thermal current density is analogous to the electrical current density, with thermal energy being carried rather than electric charge.

Consider a small fixed region of the solid within which the temperature is effectively constant. The rate at which heat appears in the region is just T times the rate at which the entropy of the electrons within the region changes ($dQ = TdS$). Thus the thermal current density

$$\mathbf{j}^q = T\mathbf{j}^s, \tag{2.23}$$

where $\mathbf{j}^s$ is the entropy current density. Since the volume of the region is fixed, changes in the entropy in the region are related to changes in the internal energy and number of electrons by the thermodynamic identity

$$TdS = dU - \zeta dN, \tag{2.24}$$

or, in terms of current densities,

$$T\mathbf{j}^s = \mathbf{j}^\epsilon - \zeta \mathbf{j}^n \tag{2.25}$$

where the energy and number current densities are given by[4]

$$\begin{aligned} \mathbf{j}^\epsilon &= \sum_n \int \frac{d\mathbf{k}}{4\pi^3} \varepsilon_n(\mathbf{k}) \mathbf{v}_n(\mathbf{k}) g_n(\mathbf{k}), & (2.26) \\ \mathbf{j}^n &= \sum_n \int \frac{d\mathbf{k}}{4\pi^3} \mathbf{v}_n(\mathbf{k}) g_n(\mathbf{k}). & (2.27) \end{aligned}$$

Substituting for $\mathbf{j}^\epsilon$ and $\mathbf{j}^n$ in Eq. (2.25), we find a thermal current density

$$\mathbf{j}^q = \sum_n \int \frac{d\mathbf{k}}{4\pi^3} [\varepsilon_n(\mathbf{k}) - \zeta] \mathbf{v}_n(\mathbf{k}) g_n(\mathbf{k}). \tag{2.28}$$

Using Eq. (2.12) in Eq. (2.28), we get

$$\mathbf{j}^q = \mathbf{L}^{21}(\mathbf{E} + \frac{\nabla\zeta}{e}) + \mathbf{L}^{22}(-\nabla T), \tag{2.29}$$

where the tensors $\mathbf{L}^{ij}$ are

$$\mathbf{L}^{21} = \left(-\frac{1}{e}\right) e^2 \int \frac{d\mathbf{k}}{4\pi^3} \left(-\frac{\partial f}{\partial \varepsilon}\right) \tau(\mathbf{k}) \mathbf{v}(\mathbf{k}) \mathbf{v}(\mathbf{k}) (\varepsilon(\mathbf{k}) - \zeta), \tag{2.30}$$

---

[4] Do not confuse the superscript n, indicating that j is the number current density, with the band index n.

$$\mathbf{L}^{22} = \left(\frac{1}{e^2 T}\right) e^2 \int \frac{d\mathbf{k}}{4\pi^3} \left(-\frac{\partial f}{\partial \varepsilon}\right) \tau(\mathbf{k})\mathbf{v}(\mathbf{k})\mathbf{v}(\mathbf{k})(\varepsilon(\mathbf{k}) - \zeta)^2. \tag{2.31}$$

Note that $\mathbf{L}^{21} = T\mathbf{L}^{12}$.

To deduce the electronic thermal conductivity $\mathbf{K}$ from these results, we note that $\mathbf{K}$ relates the thermal current to the temperature gradient under conditions in which no electric current flows. Under these conditions, Eq. (2.16) gives

$$\mathbf{E} + \frac{\nabla\zeta}{e} = -(\mathbf{L}^{11})^{-1}\mathbf{L}^{12}(-\nabla T). \tag{2.32}$$

Substituting this into Eq. (2.29) gives

$$\mathbf{j}^q = \mathbf{K}(-\nabla T), \tag{2.33}$$

where $\mathbf{K}$, the electronic thermal conductivity tensor, is given by

$$\mathbf{K} = \mathbf{L}^{22} - \mathbf{L}^{21}(\mathbf{L}^{11})^{-1}\mathbf{L}^{12}. \tag{2.34}$$

Chapter 3

One-band transport in 3D bulk materials

The expressions for σ, S and κ of a one-band material were derived in the previous chapter and can be summarized below. In general all three are tensors, and are denoted by $\boldsymbol{\sigma}$, $\mathbf{S}$ and $\mathbf{K}$, respectively.

$$\begin{aligned} \boldsymbol{\sigma} &= \mathbf{L}^{(0)}, && (3.1)\\ \mathbf{S} &= -\left(\frac{1}{eT}\right)(\mathbf{L}^{(0)})^{-1}\mathbf{L}^{(1)}, && (3.2)\\ \mathbf{K} &= \left(\frac{1}{e^2T}\right)(\mathbf{L}^{(2)} - \mathbf{L}^{(1)}(\mathbf{L}^{(0)})^{-1}\mathbf{L}^{(1)}), && (3.3) \end{aligned}$$

where

$$\mathbf{L}^{(\alpha)} = e^2 \int \frac{d\mathbf{k}}{4\pi^3}\left(-\frac{\partial f}{\partial \varepsilon}\right)\tau(\mathbf{k})\mathbf{v}(\mathbf{k})\mathbf{v}(\mathbf{k})(\varepsilon(\mathbf{k}) - \zeta)^{\alpha}. \tag{3.4}$$

For multi-band materials, each $\mathbf{L}^{(\alpha)}$ must be replaced by the sum of all the $\mathbf{L}$'s for all the partially filled bands.

3.1 Z for a 3D bulk material

In this chapter the figure of merit, Z, is calculated for a 3D bulk material. The calculations assume a one-band material.[1] This is because one-band materials (such as heavily-doped semiconductors) give the best Z for bulk materials. The reason for this is as follows. For a two-band material, the Seebeck coefficient tensor is (using Eq. (3.2))

$$\mathbf{S} = -\left(\frac{1}{eT}\right)(\mathbf{L}_1^{(0)} + \mathbf{L}_2^{(0)})^{-1}(\mathbf{L}_1^{(1)} + \mathbf{L}_2^{(1)}), \tag{3.5}$$

where the subscripts 1 and 2 denote the contributions from bands 1 and 2, respectively. Using Eq. (3.1), this can be rewritten as

$$S = \frac{\sigma_1 S_1 + \sigma_2 S_2}{\sigma_1 + \sigma_2}, \tag{3.6}$$

for an isotropic material. For anistropic materials, the measurement is assumed to be along a principal axis so that each tensor quantity can be replaced by its respective principal component. For S_1 and S_2 of opposite sign, S and Z are greatly reduced from either of their one-band values. This is the case for an intrinsic semiconductor, where the two bands are the conduction and valence bands containing electron and hole carriers, respectively. If S_1 and S_2 are of the same sign, then S is still reduced from the better of the one-band values.

The calculations are for a general, anisotropic, one-band material (assumed to be the conduction band). The only other assumptions are that of a constant relaxation time, τ, and that of parabolic bands. These assumptions are widely used in the relaxation-time approximation [4] and lead to results which are in good agreement with experiment, as shown later.

Note that the calculations are *not* restricted to semiconductors. The material can be a metal, semiconductor or semimetal, as long as it is effectively a one-band material.

---

[1] The calculation can be generalized for more than one carrier as shown in Chapter 6, where it is applied to a semiconductor with multiple carrier types.

Since parabolic bands are assumed, the electronic dispersion relation used is:

$$\varepsilon(k_x, k_y, k_z) = \frac{\hbar^2 k_x^2}{2m_x} + \frac{\hbar^2 k_y^2}{2m_y} + \frac{\hbar^2 k_z^2}{2m_z}, \tag{3.7}$$

where m_x, m_y, m_z are the effective mass components. Consider transport along a principal axis, taken to be the x-direction. From Eq. (3.4),

$$L_{xx}^{(\alpha)} = e^2 \int \frac{d^3k}{4\pi^3} \left(-\frac{\partial f}{\partial \varepsilon}\right) \tau v_x v_x (\varepsilon - \zeta)^\alpha. \tag{3.8}$$

Using $v_x = \hbar^2 k_x$, this gives

$$L_{xx}^{(\alpha)} = \frac{e^2 \tau \hbar^2}{4\pi^3 m_x^2 k_B T} \iiint k_x^2 dk_x dk_y dk_z \frac{e^{(\varepsilon-\zeta)/k_B T}}{(e^{(\varepsilon-\zeta)/k_B T} + 1)^2} (\varepsilon - \zeta)^\alpha. \tag{3.9}$$

Let $q_i^2 = \hbar^2 k_x^2 / 2m_i$, where $i = x, y, z$, then

$$dk_x dk_y dk_z = \frac{(8 m_x m_y m_z)^{\frac{1}{2}}}{\hbar^3} dq_x dq_y dq_z, \tag{3.10}$$

$$\varepsilon = q_x^2 + q_y^2 + q_z^2, \tag{3.11}$$

$$L_{xx}^{(\alpha)} = \frac{e^2 \tau \hbar^2}{4\pi^3 m_x^2 k_B T} \frac{(8 m_x m_y m_z)^{\frac{1}{2}}}{\hbar^3} \frac{2m_x}{\hbar^2} \iiint q_x^2 dq_x dq_y dq_z \frac{e^{(\varepsilon-\zeta)/k_B T}}{(e^{(\varepsilon-\zeta)/k_B T} + 1)^2} (\varepsilon - \zeta)^\alpha. \tag{3.12}$$

Going to spherical polar coordinates

$$\begin{aligned} q_x &= r \sin\theta \cos\phi, & (3.13) \\ q_y &= r \sin\theta \sin\phi, & (3.14) \\ q_z &= r \cos\theta, & (3.15) \end{aligned}$$

and doing the integral over all ϕ, θ,

$$L_{xx}^{(\alpha)} = \frac{e^2 \tau \hbar^2}{4\pi^3 m_x^2 k_B T} \frac{(8 m_x m_y m_z)^{\frac{1}{2}}}{\hbar^3} \frac{2m_x}{\hbar^2} \frac{4\pi}{3} \int_0^\infty r^4 dr \frac{e^{(r^2-\zeta)/k_B T}}{(e^{(r^2-\zeta)/k_B T} + 1)^2} (r^2 - \zeta)^\alpha. \tag{3.16}$$

Using the substitution $x = r^2/k_BT$ (x is dimensionless),

$$L_{xx}^{(\alpha)} = \frac{e^2\tau(k_BT)^{\frac{3}{2}+\alpha}}{3\pi^2 m_x}\frac{(8m_xm_ym_z)^{\frac{1}{2}}}{\hbar^3}\int_0^\infty dx\,\frac{x^{\frac{3}{2}}(x-\zeta^*)^\alpha e^{(x-\zeta^*)}}{(e^{(x-\zeta^*)}+1)^2}, \qquad (3.17)$$

where $\zeta^* = \zeta/k_BT$ is the reduced chemical potential. Integration by parts gives:

$$\begin{aligned} L_{xx}^{(0)} &= C_x\left[\frac{3}{2}F_{\frac{1}{2}}\right], && (3.18)\\ L_{xx}^{(1)} &= C_x(k_BT)\left[\frac{5}{2}F_{\frac{3}{2}} - \frac{3}{2}\zeta^*F_{\frac{1}{2}}\right], && (3.19)\\ L_{xx}^{(2)} &= C_x(k_BT)^2\left[\frac{7}{2}F_{\frac{5}{2}} - 5\zeta^*F_{\frac{3}{2}} + \frac{3}{2}\zeta^{*2}F_{\frac{1}{2}}\right], && (3.20) \end{aligned}$$

where

$$C_x = \frac{e}{3\pi^2}\left(\frac{2k_BT}{\hbar^2}\right)^{\frac{3}{2}}(m_xm_ym_z)^{\frac{1}{2}}\mu_x, \qquad (3.21)$$

μ_x is the mobility $e\tau/m_x$, and the Fermi-Dirac function F_i is given by

$$F_i = F_i(\zeta^*) = \int_0^\infty \frac{x^i dx}{e^{(x-\zeta^*)}+1}. \qquad (3.22)$$

Equations (3.1)-(3.3) can now be used to calculate the electrical conductivity σ, the Seebeck coefficient S, and the electronic contribution to the thermal conductivity κ_e:

$$\begin{aligned} \sigma &= \frac{e}{3\pi^2}\left(\frac{2k_BT}{\hbar^2}\right)^{\frac{3}{2}}(m_xm_ym_z)^{\frac{1}{2}}\mu_x\left(\frac{3}{2}F_{1/2}\right), && (3.23)\\ S &= -\frac{k_B}{e}\left(\frac{5F_{3/2}}{3F_{1/2}} - \zeta^*\right), && (3.24)\\ \kappa_e &= \frac{k_B^2T}{3\pi^2 e}\left(\frac{2k_BT}{\hbar^2}\right)^{\frac{3}{2}}(m_xm_ym_z)^{\frac{1}{2}}\mu_x\left(\frac{7}{2}F_{5/2} - \frac{25F_{3/2}^2}{6F_{1/2}}\right). && (3.25) \end{aligned}$$

Note that σ and κ_e are quadratic in charge e, but S is linear so it changes sign as $+e \rightarrow -e$. Equation (3.24) shows that the Seebeck coefficient is proportional to the difference between the average electronic energy and the chemical potential ζ. This means that for the conduction band, the Seebeck coefficient increases as ζ is lowered. If ζ lies significantly below the band edge, the material will have a very high S. This is confirmed by the fact that intrinsic semiconductors have a high S. Metals, which have ζ in the conduction band at a level comparable to the average electronic energy have a very low S. However, if one lowers ζ to increase S, the carrier density will decrease, reducing σ, so that the overall Z does not increase. So intrinsic semiconductors have a high S, but low σ. Metals have a high σ, but low S. Both have a relatively low Z. The materials with the highest Z are extrinsic (doped) semiconductors, in which ζ is within $k_B T$ of the band edge) [2]. The reduction in σ which results from an increase in S is one of the main reasons why it is difficult to increase $Z_{3D}T$ significantly and so it is not surprising that the best Z has not changed for three decades. The other reason is the Wiedermann-Franz law; an increase in σ will be accompanied by a corresponding increase in κ_e such that the resulting Z does not change significantly.

So, using

$$Z = \frac{S^2 \sigma}{\kappa_e + \kappa_{ph}}, \qquad (3.26)$$

where κ_{ph} is the phonon thermal conductivity gives

$$Z_{3D} = \frac{C_x (k_B^2/e^2) \left(\frac{5F_{3/2}}{3F_{1/2}} - \zeta^* \right)^2 \frac{3}{2} F_{1/2}}{C_x (k_B^2 T/e^2) \left(\frac{7}{2} F_{5/2} - \frac{25 F_{3/2}^2}{6 F_{1/2}} \right) + \kappa_{ph}}, \qquad (3.27)$$

or

$$Z_{3D}T = \frac{B_{3D} \left(\frac{5F_{3/2}}{3F_{1/2}} - \zeta^* \right)^2 \frac{3}{2} F_{1/2}}{B_{3D} \left(\frac{7}{2} F_{5/2} - \frac{25 F_{3/2}^2}{6 F_{1/2}} \right) + 1}, \qquad (3.28)$$

where the dimensionless quantity B_{3D} is given by

$$B_{3D} = \frac{1}{3\pi^2} \left(\frac{2 k_B T}{\hbar^2} \right)^{\frac{3}{2}} (m_x m_y m_z)^{\frac{1}{2}} \frac{k_B^2 T \mu_x}{e \kappa_{ph}}. \qquad (3.29)$$

These equations can be solved numerically. For a given value of B_{3D}, the reduced chemical potential $\zeta^* = \zeta / k_B T$ may be varied to change the value of $Z_{3D}T$. The maximum value of $Z_{3D}T$ occurs when ζ^* is equal to its optimal value, ζ^*_{opt}. See inset of Fig. 3-1) which shows a graph of ζ^*_{opt} against B_{3D}. A negative value for ζ^*_{opt} means

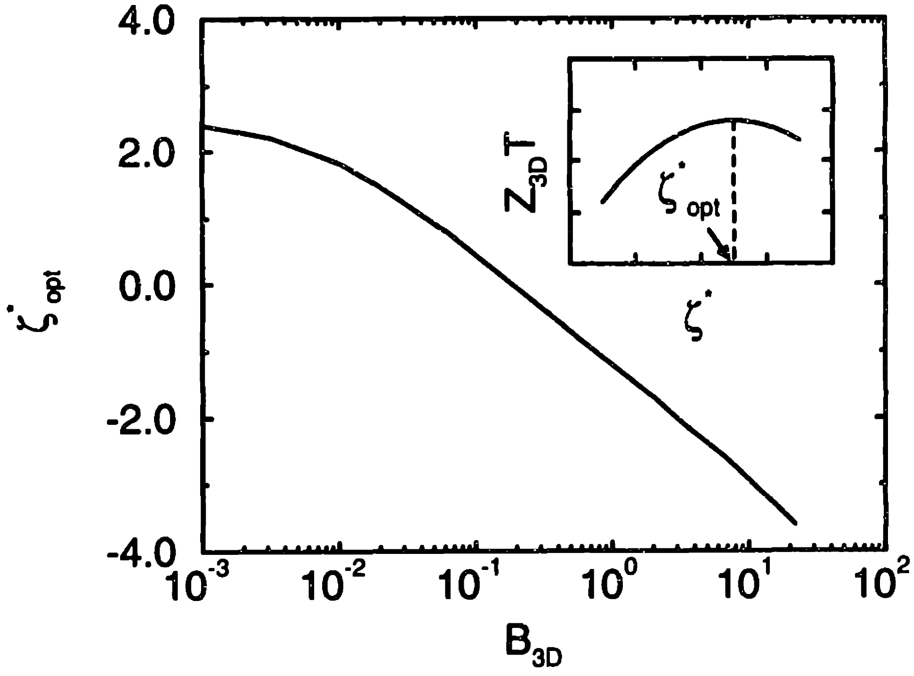

Figure 3-1: Plot of ζ^*_{opt} vs B_{3D}. The inset shows the variation of $Z_{3D}T$ with ζ^* at fixed B_{3D}.

that the optimum Fermi level is below the band edge.

In 3D bulk materials, B_{3D} is determined largely by the intrinsic properties of the material, but ζ^* may be varied by doping. To maximize $Z_{3D}T$ for a material, one first calculates B_{3D} for the intrinsic material, then uses Fig. 3-1 to determine the value of ζ^*_{opt} for this value of B_{3D}. The next step is to adjust ζ^* so that $\zeta^* = \zeta^*_{\text{opt}}$: this may be achieved by doping with suitable impurities. The maximum $Z_{3D}T$ attainable for this value of B_{3D} can be found from Fig. 3-2. Note that although doping changes ζ^* significantly, the corresponding change in B_{3D} is negligible unless the material is very heavily doped, resulting in significant changes in the band structure or mobility.

From the graph of $Z_{3D}T$ against B_{3D} in Fig. 3-2, it is clear that increasing B_{3D} increases $Z_{3D}T$. Therefore to obtain a high $Z_{3D}T$, one needs to find a material with a high B_{3D}. For a given anisotropic crystal in 3D, $Z_{3D}T$ varies with current direction and it is possible to increase B_{3D} and therefore to maximize $Z_{3D}T$ by choosing the current to flow along the direction x of highest mobility μ_x. One can often increase B_{3D} for a particular material by isoelectronic alloying to increase phonon scattering

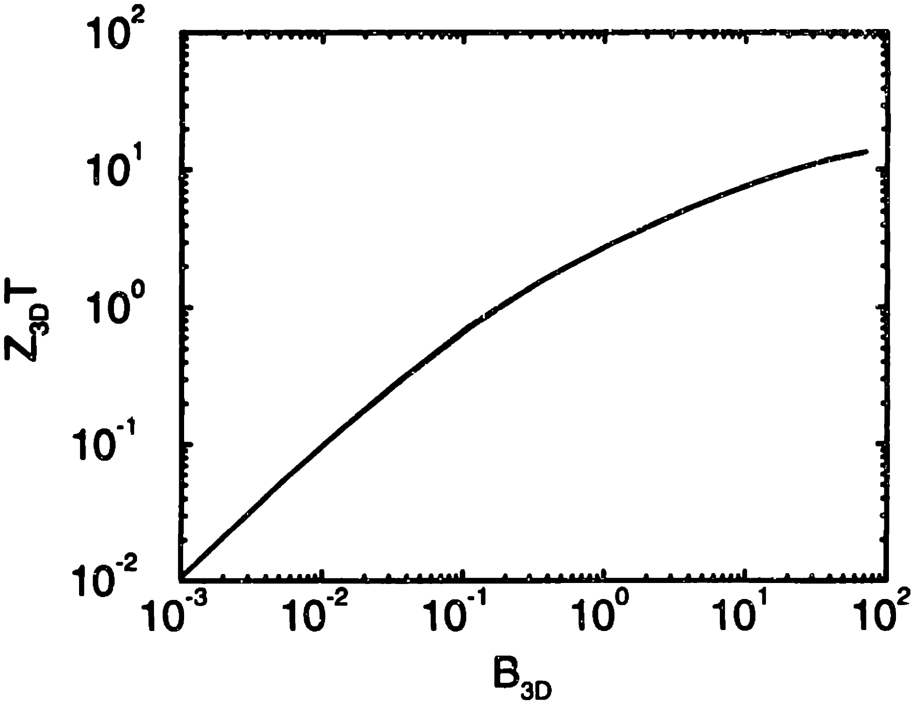

Figure 3-2: Plot of $Z_{3D}T(\zeta^{*}_{\text{opt}})$ vs B_{3D}.

and therefore to decrease κ_{ph}. However, too many impurities will reduce the mobility μ_x and decrease B_{3D}.

3.2 Calculated Z for 3D bulk Bi_2Te_3

One of the best materials for thermoelectric refrigeration is Bi_2Te_3, with a $Z_{3D}T = 0.67$ at 300K [2]. The expressions derived previously are now used to calculate $Z_{3D}T$ for bulk Bi_2Te_3.

The equations for ZT derived so far assumed a single constant energy ellipsoid in the Brillouin Zone. For multiple ellipsoids, the value of B_{3D} derived needs to be multiplied by a number of the order of the number of ellipsoids. Bi_2Te_3 has 6 ellipsoids [2], and multiplying B_{3D} by a factor of 6 gives a value of $Z_{3D}T$ in good agreement with experiment, as shown below. The exact multiplicative factor will be slightly different from 6 because not all ellipsoids are oriented in the same direction. However, since we will later compare similar calculations for 3D and 2D Bi_2Te_3, this factor should not significantly affect the comparison between $Z_{3D}T$ and $Z_{2D}T$.

Bi_2Te_3 has a trigonal structure, which can be expressed in terms of a hexagonal unit cell of lattice parameters $a_0 = 4.3$ Å and $c_0 = 30.5$ Å [2]. The compound has a highly anisotropic effective mass tensor, with effective mass components $m_x = 0.021m_0$, $m_y = 0.081m_0$ and $m_z = 0.32m_0$ [5]. The phonon thermal conductivity is $\kappa_{ph} = 1.5$ $Wm^{-1}K^{-1}$ and the direction of highest mobility is the along the a_0-axis, with $\mu_{a_0} = 1200$ $cm^2V^{-1}s^{-1}$ [2].

Substituting these values into Eq. (3.29), one obtains $B_{3D} = 0.076$ at 300K (after multiplying by 6). This gives a maximum $Z_{3D}T$ of $Z_{3D}T = 0.52$. This value is very close to the experimental result of $Z_{3D}T = 0.67$ [2]; it is slightly different because firstly the relaxation time τ may have a slight energy dependence, and secondly not all carrier pockets contribute equally, as mentioned previously. The maximum $Z_{3D}T$ occurs at $\zeta^*_{\mathrm{opt}} = 0.6$, a carrier density of about 10^{18} cm^{-3}, so the chemical potential is just above the conduction band edge and the material is a partially-degenerate n-type semiconductor.

Although the $Z_{3D}T$ of pure Bi_2Te_3 is 0.67 at 300 K, a higher $Z_{3D}T$ can be obtained by isoelectronic alloying with Sb_2Te_3. This alloying does leaves the electrical properties of Bi_2Te_3 virtually unchanged, but leads to a significant decrease in the lattice thermal conductivity κ_{ph}, due to point-defect scattering of phonons caused by the difference in masses of the Bi and Sb atoms. The lattice thermal conductivity of $Bi_{0.5}Sb_{1.5}Te_3$ is 1.0 $Wm^{-1}K^{-1}$ [2], down from 1.5 $Wm^{-1}K^{-1}$ for pure Bi_2Te_3. Thus $Bi_{0.5}Sb_{1.5}Te_3$ has a $Z_{3D}T$ of 1.0 at 300 K, and has been the material with the highest $Z_{3D}T$ for over 30 years.

In the next chapter, similar techniques will be used to calculate Z for a quantum-well superlattice structure, and the expressions derived will be used to calculate $Z_{2D}T$ for Bi_2Te_3.

material	ZT at 300 K	maximum ZT
$Bi_{0.5}Sb_{1.5}Te_3$	1.0	1.0 at 300 K
PbTe	0.4	0.8 at 600 K
$Bi_{0.88}Sb_{0.12}$	0.3	0.4 at 80 K
$Si_{0.7}Ge_{0.3}$	0.1	0.9 at 1200 K

Table 3.1: ZT values for materials commonly used in thermoelectric applications.

3.3 Other high Z materials

Although Bi_2Te_3 alloys have the highest ZT at 300 K, other materials are also used for thermoelectric applications, depending on the temperature range of interest. Table 3.1 shows the ZT of other commonly used thermoelectric materials [2], both at 300 K and at the temperature which gives the maximum ZT.

Recently, a ZT of 1.2 at 400 K [6] has been measured in a skutterudite compound, most likely $IrSb_3$ or $CoSb_3$ alloys. However the work is still at an early stage, and details have yet to be published.

Chapter 4

Two-dimensional quantum-well superlattices

A 2D quantum-well superlattice consists of alternating layers of a narrow-gap and a wide-gap semiconductor as shown in Fig. 4-1. The band offsets between the two materials are large enough so that electrons are confined to the narrow-gap material which is therefore the quantum well (Fig. 4-2). Because of the large potential barriers perpendicular to the layers, the electrons in the well form bound states (subbands) in the z-direction (Fig. 4-2) and are confined to 2D motion parallel to the layers in the x-y plane.

4.1 Z for a 2D quantum well

Expressions for S, σ, κ_e and Z are derived for transport in such quantum wells. In this section I present a general treatment for the thermoelectric figure of merit for quantum wells, while in Chapter 7 these results are applied to a specific quantum-well system PbTe/Pb$_{1-x}$Eu$_x$Te which was studied experimentally. The calculations assume that the electrons occupy only the lowest (n=1) conduction band subband of the quantum well (this is consistent with the optimization of Z arising from a one-band model), and also that there is no tunnelling through the wide-gap semiconductor (the quantum barrier).

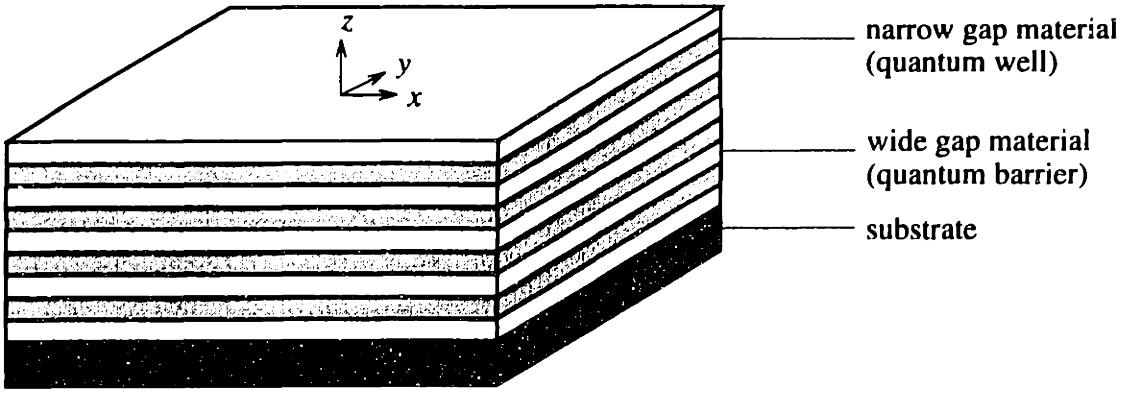

Figure 4-1: Quantum-well superlattice structure.

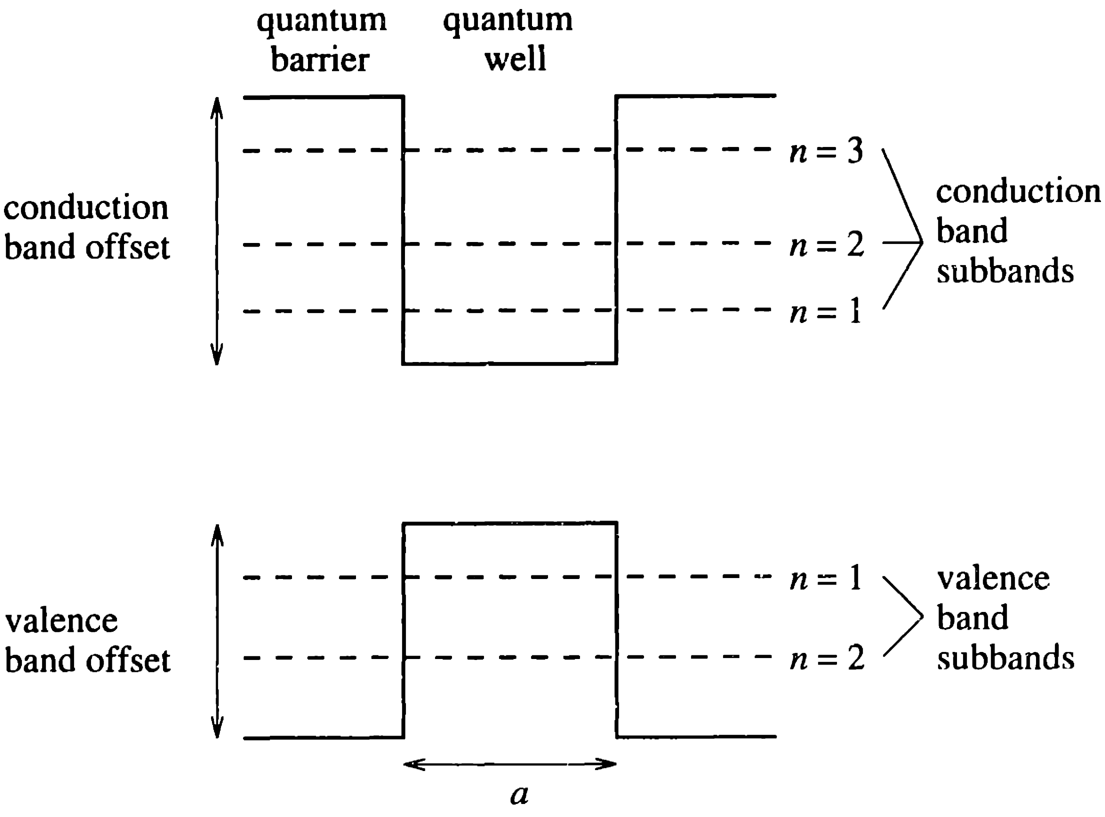

Figure 4-2: Quantum well energy levels.

Let the multilayers be parallel to the x-y plane and the currents flow in the x-direction. The general expressions Eqs. (3.1)-(3.3) can be applied to the 2D system. Since the system has a 2D density of states, the density of states per unit volume of a quantum well is now $d\mathbf{k}/2\pi^2 a$, where a is the thickness of the quantum well. So now $\mathbf{L}^{(\alpha)}$ (Eq. (3.4)) becomes

$$\mathbf{L}^{(\alpha)} = e^2 \int \frac{d\mathbf{k}}{2\pi^2 a} \left(-\frac{\partial f}{\partial \varepsilon}\right) \tau(\mathbf{k})\mathbf{v}(\mathbf{k})\mathbf{v}(\mathbf{k})(\varepsilon(\mathbf{k}) - \zeta)^\alpha, \tag{4.1}$$

where now $d\mathbf{k} = dk_x dk_y$. The electronic dispersion relation used is

$$\varepsilon(k_x, k_y) = \frac{\hbar^2 k_x^2}{2m_x} + \frac{\hbar^2 k_y^2}{2m_y}, \tag{4.2}$$

indicating free electron-like motion in the x-y plane. Note that here ε is measured relative to the band edge of the lowest subband, which for an infinite potential well is at energy $\hbar^2\pi^2/2m_z a^2$.

Using $v_x = \hbar k_x/2m_x$, Eq. (4.1) gives

$$L_{xx}^{(\alpha)} = \frac{e^2\tau\hbar^2}{2\pi^2 a m_x^2 k_B T} \iint k_x^2 dk_x dk_y \frac{e^{(\varepsilon-\zeta)/k_B T}}{(e^{(\varepsilon-\zeta)/k_B T} + 1)^2}(\varepsilon - \zeta)^\alpha. \tag{4.3}$$

Let $q_i^2 = \hbar^2 k_x^2/2m_i$, where $i = x, y$, then

$$dk_x dk_y = \frac{(4m_x m_y)^{\frac{1}{2}}}{\hbar^2} dq_x dq_y, \tag{4.4}$$

$$\varepsilon = q_x^2 + q_y^2, \tag{4.5}$$

$$L_{xx}^{(\alpha)} = \frac{e^2\tau\hbar^2}{2\pi^2 a m_x^2 k_B T} \frac{(4m_x m_y)^{\frac{1}{2}}}{\hbar^2} \frac{2m_x}{\hbar^2} \iint q_x^2 dq_x dq_y \frac{e^{(\varepsilon-\zeta)/k_B T}}{(e^{(\varepsilon-\zeta)/k_B T} + 1)^2}(\varepsilon - \zeta)^\alpha. \tag{4.6}$$

Going to polar coordinates

$$q_x = r\cos\theta, \tag{4.7}$$

$$q_y = r\sin\theta, \tag{4.8}$$

and doing the integral over all θ, we obtain

$$L_{xx}^{(\alpha)} = \frac{e^2\tau\hbar^2}{2\pi^2 a m_x^2 k_B T} \frac{(4m_x m_y)^{\frac{1}{2}}}{\hbar^2} \frac{2m_x}{\hbar^2} \pi \int_0^\infty r^3 dr \frac{e^{(r^2-\zeta)/k_BT}}{(e^{(r^2-\zeta)/k_BT}+1)^2} (r^2-\zeta)^\alpha . \tag{4.9}$$

Using the substitution $x = r^2/k_BT$,

$$L_{xx}^{(\alpha)} = \frac{e^2\tau(k_BT)^{1+\alpha}}{2\pi a m_x} \frac{(4m_x m_y)^{\frac{1}{2}}}{\hbar^2} \int_0^\infty dx \frac{x(x-\zeta^*)^\alpha e^{(x-\zeta^*)}}{(e^{(x-\zeta^*)}+1)^2}, \tag{4.10}$$

where $\zeta^* = \zeta/k_BT$ is the reduced chemical potential. Integration by parts gives:

$$\begin{aligned}
L_{xx}^{(0)} &= D_x\left[F_0\right], \qquad &(4.11)\\
L_{xx}^{(1)} &= D_x(k_BT)\left[2F_1 - \zeta^* F_0\right], \qquad &(4.12)\\
L_{xx}^{(2)} &= D_x(k_BT)^2\left[3F_2 - 4\zeta^* F_1 + \zeta^{*2} F_0\right], \qquad &(4.13)\\
& &(4.14)
\end{aligned}$$

where

$$D_x = \frac{e}{2\pi a}\left(\frac{2k_BT}{\hbar^2}\right)(m_x m_y)^{\frac{1}{2}}\mu_x \tag{4.15}$$

(the mobility $\mu_x = e\tau/m_x$), and the Fermi-Dirac function F_i is given by

$$F_i = F_i(\zeta^*) = \int_0^\infty \frac{x^i dx}{e^{(x-\zeta^*)}+1}. \tag{4.16}$$

Equations (3.1)-(3.3) can now be used to calculate the electrical conductivity σ, the Seebeck coefficient S, and the electronic contribution to the thermal conductivity κ_e:

$$\begin{aligned}
\sigma &= \frac{e}{2\pi a}\left(\frac{2k_BT}{\hbar^2}\right)(m_x m_y)^{\frac{1}{2}}\mu_x\left(F_0\right), \qquad &(4.17)\\
S &= -\frac{k_B}{e}\left(\frac{2F_1}{F_0} - \zeta^*\right), \qquad &(4.18)\\
\kappa_e &= \frac{k_B^2 T}{2\pi a e}\left(\frac{2k_BT}{\hbar^2}\right)(m_x m_y)^{\frac{1}{2}}\mu_x\left(3F_2 - \frac{4F_1^2}{F_0}\right). \qquad &(4.19)
\end{aligned}$$

Using Eq. (3.26) gives

$$Z_{2D} = \frac{D_x(k_B^2/e^2)\left(\frac{2F_1}{F_0} - \zeta^*\right)^2 F_0}{D_x(k_B^2 T/e^2)\left(3F_2 - \frac{4F_1^2}{F_0}\right) + \kappa_{ph}}, \tag{4.20}$$

or

$$Z_{2D}T = \frac{B_{2D}\left(\frac{2F_1}{F_0} - \zeta^*\right)^2 F_0}{B_{2D}\left(3F_2 - \frac{4F_1^2}{F_0}\right) + 1}, \tag{4.21}$$

where the dimensionless quantity B_{2D} is given by

$$B_{2D} = \frac{1}{2\pi a}\left(\frac{2k_BT}{\hbar^2}\right)(m_x m_y)^{\frac{1}{2}}\frac{k_B^2 T\mu_x}{e\kappa_{ph}}. \tag{4.22}$$

These expressions are evaluated numerically. For a given value of B_{2D}, ζ^* may be varied to change the value of $Z_{2D}T$. The variation of $Z_{2D}T$ with ζ^* at fixed B_{2D} is shown as in inset in Fig. 4-3. The maximum value of $Z_{2D}T$ occurs when $\zeta^* = \zeta^*_{\text{opt}}$. Figure 4-3 shows a graph of ζ^*_{opt} against B_{2D}, and Fig. 4-4 a graph of $Z_{2D}T(\zeta^*_{\text{opt}})$ against B_{2D}.

To maximize $Z_{2D}T$ for a given quantum well structure (and hence a fixed B_{2D}), one proceeds in a manner similar to the 3D case. B_{2D} is calculated from Eq. (4.22) and ζ^*_{opt} is determined from Fig. 4-3. $\zeta^* = \zeta^*_{\text{opt}}$ is achieved by doping.

Now as with the 3D case, $Z_{2D}T$ increases with increasing B_{2D}. In 3D, the only means available to increase B_{3D} in an anisotropic crystal is to choose the current direction to be the direction of highest mobility. For 2D quantum wells, the situation is more complex. There are more degrees of freedom available to increase B_{2D} and hence optimize $Z_{2D}T$. A higher mobility current direction will still give a higher B_{2D}, but significantly so will a narrower layer thickness a for the quantum well. It may also be possible to increase B_{2D} by a judicious choice of the crystallographic plane in which to make the layers. If the layers are made in the x-y plane and the currents flow along the x-direction, then B_{2D} will be the expression in Eq. (4.22). If the layers are made in the x-z plane and the currents still flow along the x-direction, then m_z will replace m_y in the expression for B_{2D}. In this orientation, B_{2D} and therefore $Z_{2D}T$

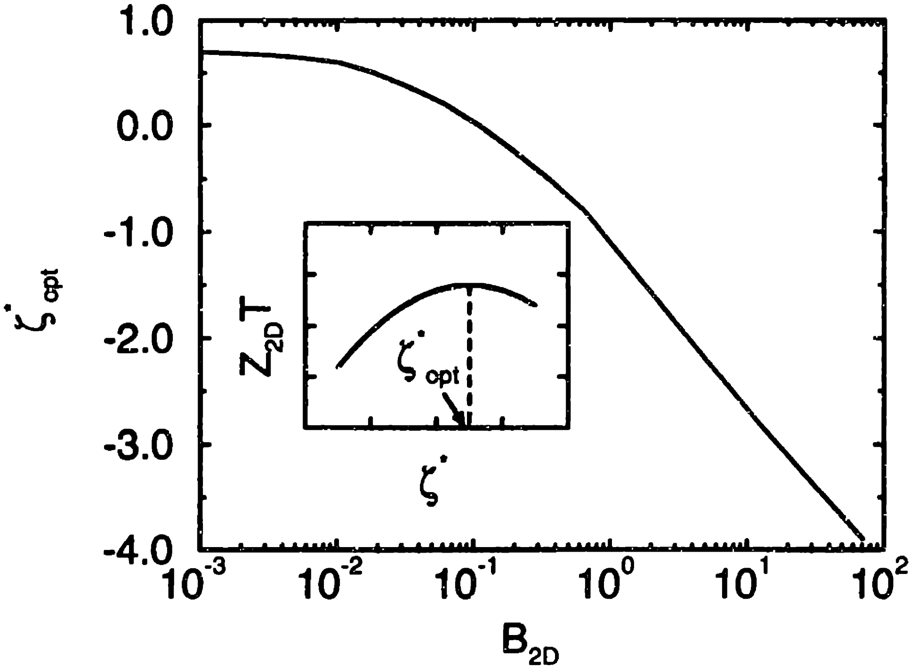

Figure 4-3: Plot of ζ^*_{opt} vs B_{2D} for a 2D quantum well. The inset shows the variation of $Z_{2D}T$ with ζ^* at fixed B_{2D}.

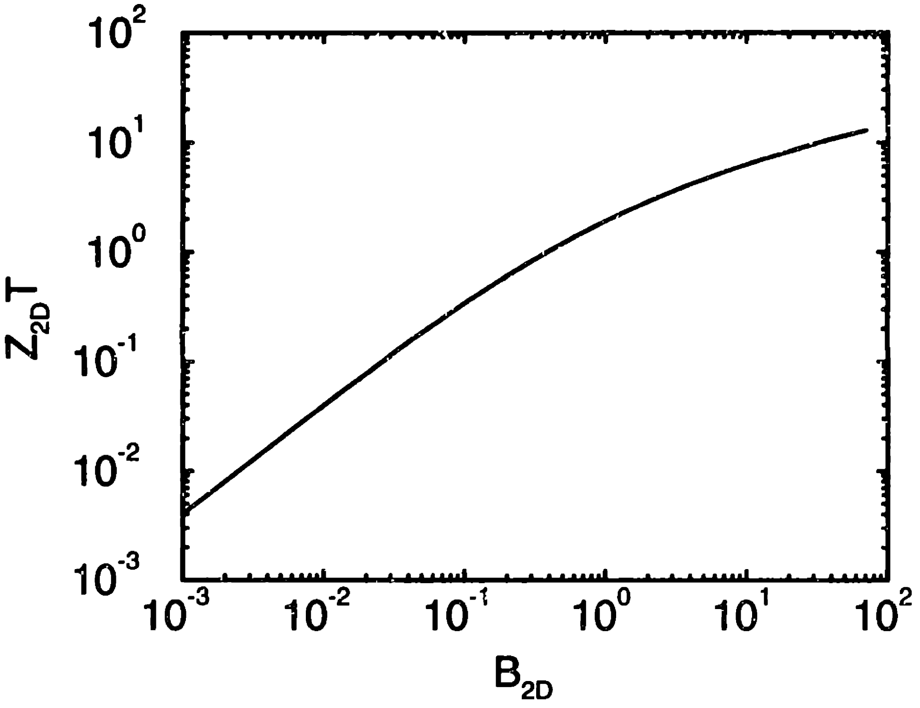

Figure 4-4: Plot of $Z_{2D}T(\zeta^*_{opt})$ vs B_{2D} for a 2D quantum well.

will be higher than the previous case if $m_z > m_y$. So one can increase $Z_{2D}T$ not only by choosing the optimum current direction, but also by using narrower layers and by choosing the best orientation in which to make the layers.

4.2 Calculated Z for Bi_2Te_3 layers in a quantum well superlattice structure

The expressions for $Z_{2D}T$ are now used to estimate what the figure of merit would be for a Bi_2Te_3 quantum well at 300 K.

In a quantum well structure, since the electrons are confined to 2D motion parallel to the layers, there is no scattering off the interface between layers, so the carrier mobility in a direction parallel to the layers is unchanged.[1] So if the a_0-axis is parallel to the layers, then $\mu_{a_0} = 1200\ \mathrm{cm^2s^{-1}V^{-1}}$ as before. However, phonons are not confined to move in 2D, so they can scatter off the interfaces. In thin layers this may reduce the phonon thermal conductivity κ_{ph}. Now

$$\kappa_{ph} = \frac{1}{3}C_v v l \tag{4.23}$$

where l is the phonon mean free path, C_v is the lattice heat capacity and v is the velocity of sound in the material. For Bi_2Te_3, $C_v = 1.2\times10^6\ \mathrm{JK^{-1}m^{-3}}$ and $v = 3\times10^3$ $\mathrm{ms^{-1}}$ [5], giving a value of l = 10 Å. If the layer thickness a is greater than 10 Å, then layering does not seriously affect the mean free path l and κ_{ph} should then be the same as its bulk value. This is a conservative assumption used to make numerical estimates for $Z_{2D}T$, as interface scattering will still occur for $a >$ 10 Å; this will cause a slight decrease in κ_{ph} and an increase in $Z_{2D}T$. However, if a is less than 10 Å, then l and κ_{ph} are limited by phonon scattering off the interfaces and a good estimate for κ_{ph} is obtained by setting $l = a$ and using Eq. (4.23). Again, this is a conservative

---

[1] This an approximation for an ideal quantum well system. In a real system, some electrons will move at an angle to the inferface, so some interface scattering can be expected to occur. However, as described in Chapter 7, the mobilities in some quantum well systems are comparable to bulk mobilities.

estimate because the surface roughness and imperfections are expected to reduce κ_{ph} further.

From the expression for B_{2D} in Eq. (4.22), decreasing the layer thickness a increases B_{2D} and therefore increases $Z_{2D}T$. Also, if $a < 10$ Å, then κ_{ph} is reduced from its bulk value, resulting in an even greater increase in $Z_{2D}T$. So to achieve the best $Z_{2D}T$, it is necessary to make the layers as thin as possible.

When calculating $\zeta^*_{\rm opt}$ for a material, one must check to make sure that it does not lie above the energy $E_{n=2}$ of the next to lowest subband of the quantum well. If $\zeta^*_{\rm opt}$ does lie above $E_{n=2}$, then both the n=1 and n=2 subbands would contribute significantly to $Z_{2D}T$: this is inconsistent with the assumption of a one-band system and one would need to extend the model in order to get meaningful results. In practice, this is not a problem for the following reasons. In order to obtain a high $Z_{2D}T$, one requires a low a. This raises the energy of the n=2 subband because $E_{n=2} = 2\frac{\hbar^2\pi^2}{m_z a^2}$. At the same time, a lower a results in a higher B_{2D} and from Fig. 4-3 this means a lower $\zeta^*_{\rm opt}$, moving it further away from the n=2 subband. So decreasing a moves $E_{n=2}$ up in energy and ζ down in energy. This means that for values of a below a certain characteristic thickness, ζ will always lie below $E_{n=2}$ and the model will be self-consistent. This characteristic thickness will usually be above the values of a which are of interest, as shown in the calculations for Bi_2Te_3 below.

$Z_{2D}T(\zeta^*_{\rm opt})$ was calculated as a function of a for superlattice layers of Bi_2Te_3 in 2 distinct orientations: (1) Layers parallel to the x-y plane (a_0-b_0 plane), (2) Layers parallel to the x-z plane (a_0-c_0 plane). The current was assumed to flow along the high mobility a_0-axis. The effective masses, mobility and lattice thermal conductivity used in the calculation of $Z_{3D}T$ in Chapter 3 were used in this calculation of $Z_{2D}T$.

If the layers are made parallel to the x-y plane, the minimum possible layer thickness is 10.2 Å, as this is the length of the smallest repeating distance in the z-direction [2]. Since this thickness is greater than 10 Å, we assume that $\kappa_{ph} = 1.5$ $\mathrm{Wm^{-1}K^{-1}}$ as in 3D. If the layers are parallel to the x-z (a_0-c_0) plane, the minimum possible layer thickness is 3.8 Å. This is because the shape of the hexagonal unit cell is a parallelepiped, and the height of the cell perpendicular to the a_0-c_0 plane (i.e., in

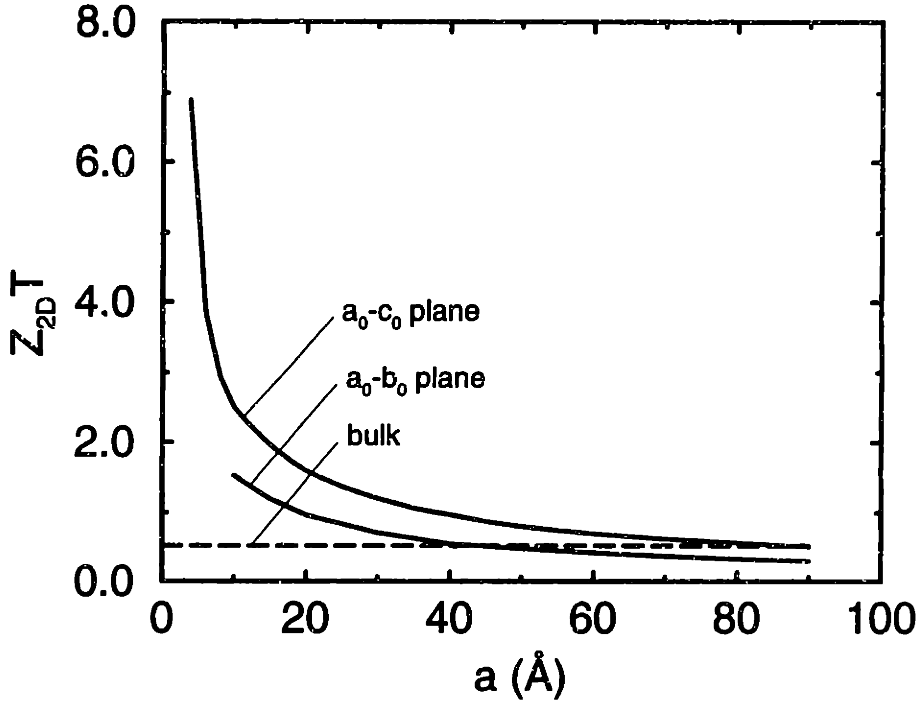

Figure 4-5: Plot of $Z_{2D}T(\zeta^*_{\rm opt})$ vs layer thickness a for (1) a_0-b_0 plane layers and (2) a_0-c_0 plane layers of Bi_2Te_3. The dashed line indicates the best ZT for 3D bulk Bi_2Te_3.

the y-direction) is $a_0 \sin 60^o = 3.8$ Å. So for $a > 10$ Å, $\kappa_{ph} = 1.5$ Wm^{-1}K^{-1}, while for $a < 10$ Å, $\kappa_{ph} = \frac{1}{3}C_v v l$ where $l = a$. Fig. 4-4 was used to calculate $Z_{2D}T(\zeta^*_{\rm opt})$, after multiplying B_{2D} by a factor of 6 for the 6 electron carrier pockets of Bi_2Te_3. Note that layering lowers the symmetry of the material, so the effective number of carrier pockets contributing to $Z_{2D}T$ may be less than that for $Z_{3D}T$. Since there is no reliable way to estimate the actual number, the 3D value of 6 was assumed. The results are shown in Fig. 4-5, togethei with a line indicating the best 3D figure of merit of $Z_{3D}T = 0.52$ estimated by calculation in Chapter 3. Experimentally $Z_{3D}T = 0.67$ for pure bulk Bi_2Te_3 [2], so agreement with theory for the bulk material is good.

Before any conclusions can be drawn, it is necessary to check the validity of the results by making sure that ζ does indeed lie below $E_{n=2}$ for the values of a in Fig. 4-5, i.e., for $a \leq 90$ Å. For the a_0-b_0 plane orientation, $B_{2D} = 0.085$ at $a = 90$ Å, giving $\zeta^*_{\rm opt} = 0.2$ from Fig. 4-3. This gives $\zeta = 0.2\hbar^2\pi^2/m_z a^2$, which is significantly less than the energy gap $3\hbar^2\pi^2/2m_z a^2$ between the first and second subbands, so the results for $a \leq 90$ Å are valid. Similarly, an a_0-c_0 plane layer of thickness $a = 90$ Å gives $B_{2D} = 0.17$ and $\zeta^*_{\rm opt} = -0.05$. As $\zeta^*_{\rm opt}$ is negative, ζ must be even lower than the n=1 subband, so the one-band model results are valid.

The results for both orientations show a significant increase in $Z_{2D}T$ as the quantum well thickness is lowered. This increase is due mainly to the enhancement of the density of electronic states per unit volume that occurs for small well widths. For a given value of a, $Z_{2D}T$ for the a_0-c_0 plane orientation is higher than for the a_0-b_0 plane. This is because the factor $(m_x m_z)^{1/2}$ in B_{2D} (proportional to the density of states) for the a_0-c_0 plane is higher than the factor $(m_x m_y)^{1/2}$ for the a_0-b_0 plane.

For layers parallel to the a_0-b_0 plane, $Z_{2D}T$ is higher than $Z_{3D}T$ for layers thinner than about 40 Å. The maximum $Z_{2D}T$ that can be obtained for this layer orientation is 1.5, which is about 3 times higher than the bulk value of 0.52. This value of $Z_{2D}T$ occurs at $a = 10.2$ Å, which is the minimum possible layer thickness.

For layers parallel to the a_0-c_0 plane, $Z_{2D}T$ is higher than $Z_{3D}T$ for layers thinner than 85 Å. As the layers are made even thinner, the increase in $Z_{2D}T$ becomes more significant, increasing sharply when $a < 10$ Å at which point phonon scattering off the interfaces becomes important. To estimate a maximum $Z_{2D}T$ that can be obtained for this layer orientation, we assume $a = 3.8$ Å, a single layer thick quantum well, for which $Z_{2D}T = 6.9$, a 14-fold increase over the bulk value.

Note that the assumptions for calculation depend on the use of effective mass theory which perhaps requires a few atomic layers to yield bulk values for the masses that I used in my calculations. However, the experimental results described in Chapter 7 show that effective mass theory appears to be valid for wells as narrow as 15 Åin some systems. Also, although the calculation is for electrons, the same approach also follows for holes. Chapter 6 shows calculations for a system which includes both holes and electrons.

So, in principle, a huge increase in ZT can be achieved by using superlattices of Bi_2Te_3, provided the Bi_2Te_3 layers are oriented in the a_0-c_0 plane. Even if the layers are prepared in the a_0-b_0 plane, a factor of 3 increase over $Z_{3D}T$ is still possible, provided that very thin layers are used. To realize these increases, a number of experimental difficulties must be overcome. It may be difficult to produce a_0-c_0 plane layers, since thin films of Bi_2Te_3 grow predominantly in the a_0-b_0 plane [7]. It may also be difficult prepare layers of uniform thickness if they are only a few unit cells thick. However, if these potential problems can be overcome, then a suitable lattice-matched wide-gap semiconductor must be found which will act as the quantum barrier in the superlattice. The band gap of the barrier material and the band offsets must be such that the electrons are confined to 2D motion in the Bi_2Te_3 layers.

Chapter 5

One-dimensional conductors

In the previous chapter, we considered the effect on ZT of using materials in two-dimensional structures such as 2D quantum well superlattices. We showed that this approach could yield a significant increase in ZT. Recently, new fabrication technology has made it possible to confine an electron gas to *one* dimension [8], thus making it possible to produce a one-dimensional conductor. Within the last few months, one-dimensional conductors were obtained by a different method: the encapsulation of metal filaments in carbon nanotubes [9, 10]. Some of these tubes are 1.5 nm in diameter [10], so it is now possible to fabricate very narrow quantum wires. In this paper, we investigate theoretically the effect on ZT of using materials in the form of 1D conductors or quantum wires. These structures will significantly alter ZT since the electrons are now confined to move in a single dimension. In addition, there will be increased phonon scattering from the surfaces of the wires. This will lead to a reduction in the lattice thermal conductivity and hence a further increase in ZT.

5.1 Z for a quantum wire

Expressions for S, σ and κ_e are derived for transport in a 1D quantum wire. The calculations are for a general one-band material (assumed again to be the lowest subband in the conduction band). Let the conductor be square in cross-section, with a side of length a. Let the current flow in the x-direction. The general expressions

Eqs. (3.1)-(3.3) can be applied to the 1D system. Since the system has a 1D density of states, the density of states per unit volume of a quantum wire is now $d\mathbf{k}/\pi a^2$. So now $\mathbf{L}^{(\alpha)}$ (Eq. (3.4)) becomes

$$\mathbf{L}^{(\alpha)} = e^2 \int \frac{d\mathbf{k}}{\pi a^2} \left(-\frac{\partial f}{\partial \varepsilon}\right) \tau(\mathbf{k})\mathbf{v}(\mathbf{k})\mathbf{v}(\mathbf{k})(\varepsilon(\mathbf{k}) - \zeta)^\alpha, \tag{5.1}$$

where now $d\mathbf{k} = dk_x$. The electronic dispersion relation used is

$$\varepsilon(k_x) = \frac{\hbar^2 k_x^2}{2m_x} \tag{5.2}$$

indicating free electron-like motion in the x-direction. Here ε is measured relative to the band edge of the subband, which for a quantum wire with infinite potential barriers is at energy $\hbar^2\pi^2/2m_y a^2 + \hbar^2\pi^2/2m_z a^2$.

Using $v_x = \hbar k_x/2m_x$, Eq. (5.1) gives

$$L_{xx}^{(\alpha)} = \frac{e^2\tau\hbar^2}{\pi a^2 m_x^2 k_B T} \int_{-\infty}^{\infty} k_x^2 dk_x \frac{e^{(\varepsilon-\zeta)/k_B T}}{(e^{(\varepsilon-\zeta)/k_B T} + 1)^2} (\varepsilon - \zeta)^\alpha. \tag{5.3}$$

Let $q_x^2 = \hbar^2 k_x^2/2m_x$, then

$$dk_x = \frac{(2m_x)^{\frac{1}{2}}}{\hbar} dq_x, \tag{5.4}$$

$$\varepsilon = q_x^2, \tag{5.5}$$

$$L_{xx}^{(\alpha)} = \frac{e^2\tau\hbar^2}{\pi a^2 m_x^2 k_B T} \frac{(2m_x)^{\frac{1}{2}}}{\hbar} \frac{2m_x}{\hbar} 2 \int_0^{\infty} q_x^2 dq_x \frac{e^{(\varepsilon-\zeta)/k_B T}}{(e^{(\varepsilon-\zeta)/k_B T} + 1)^2} (\varepsilon - \zeta)^\alpha. \tag{5.6}$$

Using the substitution $x = q_x^2/k_B T$, we obtain

$$L_{xx}^{(\alpha)} = \frac{2e^2\tau(k_B T)^{\frac{1}{2}+\alpha}}{\pi a^2 m_x} \frac{(2m_x)^{\frac{1}{2}}}{\hbar} \int_0^{\infty} dx \frac{x^{\frac{1}{2}}(x - \zeta^*)^\alpha e^{(x-\zeta^*)}}{(e^{(x-\zeta^*)} + 1)^2}, \tag{5.7}$$

where $\zeta^* = \zeta/k_B T$ is the reduced chemical potential. Integration by parts gives:

$$L_{xx}^{(0)} = E_x \left[\frac{1}{2} F_{-\frac{1}{2}}\right], \tag{5.8}$$

$$L_{xx}^{(1)} = E_x(k_B T) \left[\frac{3}{2} F_{\frac{1}{2}} - \frac{1}{2}\zeta^* F_{-\frac{1}{2}}\right], \tag{5.9}$$

$$L_{xx}^{(2)} = E_x(k_BT)^2\left[\frac{5}{2}F_{\frac{3}{2}} - 3\zeta^* F_{\frac{1}{2}} + \frac{1}{2}\zeta^{*2}F_{-\frac{1}{2}}\right], \tag{5.10}$$

where

$$E_x = \frac{2e}{\pi a^2}\left(\frac{2k_BT}{\hbar^2}\right)^{\frac{1}{2}} m_x^{\frac{1}{2}}\mu_x \tag{5.11}$$

(the mobility $\mu_x = e\tau/m_x$), and the Fermi-Dirac function F_i is given by

$$F_i = F_i(\zeta^*) = \int_0^\infty \frac{x^i dx}{e^{(x-\zeta^*)}+1}. \tag{5.12}$$

Equations (3.1)-(3.3) can now be used to calculate the electrical conductivity σ, the Seebeck coefficient S, and the electronic contribution to the thermal conductivity κ_e:

$$\begin{aligned} \sigma &= \frac{2e}{\pi a^2}\left(\frac{2k_BT}{\hbar^2}\right)^{\frac{1}{2}} m_x^{\frac{1}{2}}\mu_x\left(\frac{1}{2}F_{-1/2}\right), &(5.13)\\ S &= -\frac{k_B}{e}\left(\frac{3F_{1/2}}{F_{-1/2}} - \zeta^*\right), &(5.14)\\ \kappa_e &= \frac{2k_B^2T}{\pi a^2 e}\left(\frac{k_BT}{\hbar^2}\right) m_x^{\frac{1}{2}}\mu_x\left(\frac{5}{2}F_{3/2} - \frac{9F_{1/2}^2}{2F_{-1/2}}\right). &(5.15)\end{aligned}$$

Using Eq. (3.26) gives

$$Z_{1D} = \frac{E_x(k_B^2/e^2)\left(\frac{3F_{1/2}}{F_{-1/2}} - \zeta^*\right)^2 \frac{1}{2}F_{-1/2}}{E_x(k_B^2T/e^2)\left(\frac{5}{2}F_{3/2} - \frac{9F_{1/2}^2}{2F_{-1/2}}\right) + \kappa_{ph}}, \tag{5.16}$$

or

$$Z_{1D}T = \frac{B_{1D}\left(\frac{3F_{1/2}}{F_{-1/2}} - \zeta^*\right)^2 \frac{1}{2}F_{-1/2}}{B_{1D}\left(\frac{5}{2}F_{3/2} - \frac{9F_{1/2}^2}{2F_{-1/2}}\right) + 1}, \tag{5.17}$$

where the dimensionless quantity B_{1D} is given by

$$B_{1D} = \frac{2}{\pi a^2}\left(\frac{2k_BT}{\hbar^2}\right)^{\frac{1}{2}} m_x^{\frac{1}{2}}\frac{k_B^2T\mu_x}{e\kappa_{ph}}. \tag{5.18}$$

These expressions were evaluated numerically. For a given value of B_{1D}, the

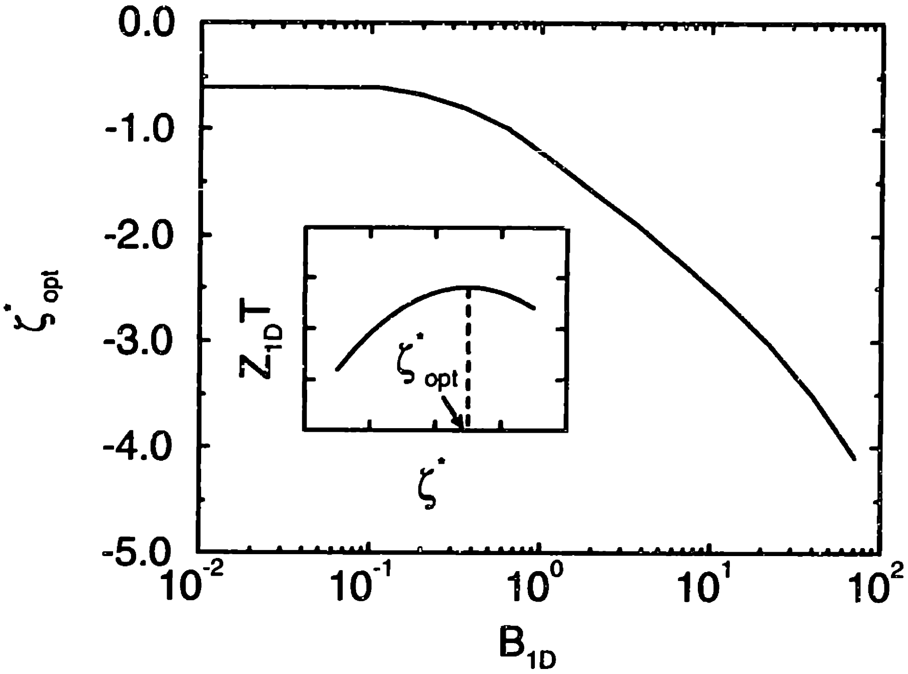

Figure 5-1: Plot of $\zeta^*_{\rm opt}$ vs B_{1D} for a 1D quantum wire. The inset shows the variation of $Z_{1D}T$ with ζ^* at fixed B_{1D}.

reduced chemical potential $\zeta^* = \zeta/k_BT$ may be varied to change the value of $Z_{1D}T$. The maximum value of $Z_{1D}T$ occurs when ζ^* is equal to its optimal value, $\zeta^*_{\rm opt}$ as shown in the inset of Fig. 5-1. B_{1D} is determined largely by the intrinsic properties of the material, but ζ^* may be varied by doping. To maximize $Z_{1D}T$ for a material, one first calculates B_{1D} for the intrinsic material, then determines the value of $\zeta^*_{\rm opt}$ which maximizes $Z_{1D}T$ for this value of B_{1D} from Fig. 5-1. The next step is to adjust ζ^* so that $\zeta^* = \zeta^*_{\rm opt}$: this may be achieved by doping. It may be necessary to keep the dopant ions spatially removed from the conduction path to avoid impurity scattering. This form of doping (modulation doping) has been used in 2D quantum well heterostructures. $Z_{1D}T(\zeta^*_{\rm opt})$ rises monotonically with increasing B_{1D} as shown in Fig. 5-2, so it is necessary to maximize B_{1D} in order to achieve the maximum $Z_{1D}T$.

Note that the factor B_{1D} varies as $(1/a^2)$. This means that $Z_{1D}T$ increases as the wire width is narrowed. Recall that for a quantum well, the corresponding factor B_{2D} varies as $(1/a)$, so the figure of merit for a 1D wire will increase more rapidly with

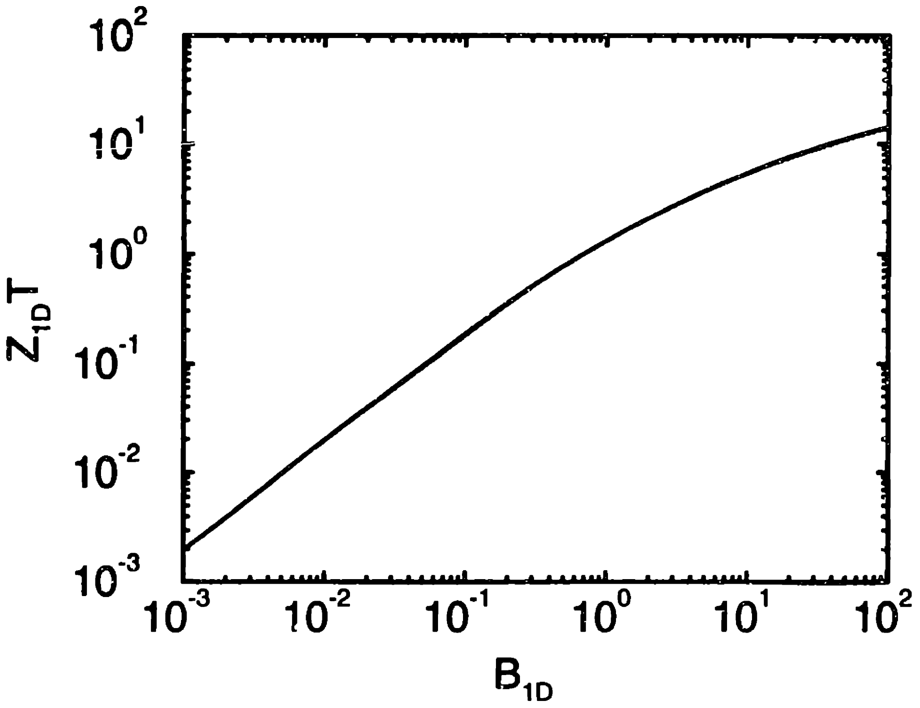

Figure 5-2: Plot of $Z_{1D}T(\zeta^*_{\mathrm{opt}})$ vs B_{1D} for a 1D quantum wire.

decreasing width than a quantum well.

5.2 Calculated Z for a quantum wire of Bi_2Te_3

The expressions derived previously are now used to calculate $Z_{1D}T$ for Bi_2Te_3 in a 1D quantum wire structure at 300 K.

Bi_2Te_3 has a trigonal structure, which can be expressed in terms of a hexagonal unit cell of lattice parameters $a_0 = 4.3$ Å and $c_0 = 30.5$ Å [2]. The compound has an anisotropic effective mass tensor, with components $m_x = 0.02m_0$, $m_y = 0.08m_0$ and $m_z = 0.32m_0$ [5]. The lattice thermal conductivity is $\kappa_{ph} = 1.5$ $\mathrm{Wm^{-1}K^{-1}}$ and the mobility along the a_0 or x axis is $\mu_x = 1200$ $\mathrm{cm^2V^{-1}s^{-1}}$ [2].

The equation for $Z_{1D}T$ derived so far assumed a single carrier pocket in the Brillouin zone of the bulk material. For multiple pockets, the value of B_{1D} in Eq. (5.18) needs to be multiplied by a number of the order of the number of pockets. Bi_2Te_3 has six carrier pockets, each with a slightly different orientation in the Brillouin zone [5].

In Chapters 3 and 4, in order to make simple numerical estimates of ZT for both bulk and superlattice Bi_2Te_3, we assumed that all six pockets have the same orientation. This assumption in fact gave a value for bulk $Z_{3D}T$ in good agreement with the experimental value. In order to make numerical estimates of ZT for one-dimensional Bi_2Te_3, we made the same assumption. This consistent approach enabled us to make direct comparisons between the calculated values of ZT for 3D, 2D and 1D Bi_2Te_3. The exact values of the parameters of Bi_2Te_3 are not of crucial importance since the material is used mainly as an illustration of the effect on ZT of going to lower dimensions. Since six carrier pockets are assumed for 1D Bi_2Te_3, the expression for B_{1D} becomes

$$B = 6\frac{2}{\pi a^2}\left(\frac{2k_BT}{\hbar^2}\right)^{\frac{1}{2}}\frac{k_B^2 T m_x^{\frac{1}{2}}\mu_x}{e\kappa_{ph}} \tag{5.19}$$

If the wire is fabricated for conduction along the y or z axes, then the variable $m_x^{\frac{1}{2}}\mu_x$ is replaced by $m_y^{\frac{1}{2}}\mu_y$ or $m_z^{\frac{1}{2}}\mu_z$, respectively.

When calculating ζ^*_{opt} for a material, one must check that it does not lie above the energy of the next to lowest subband of the quantum wire. If ζ^*_{opt} does indeed lie above the energy of the next subband, then more than one subband will contribute significantly to $Z_{1D}T$: this is inconsistent with the assumption of a one-band system and one would need to extend the model in order to get meaningful results.

$Z_{1D}(\zeta^*_{\text{opt}})$ was calculated as a function of width a for quantum wires of Bi_2Te_3 fabricated along the x, y and z directions. The mobilities μ_y and μ_z were estimated using the assumption that $m_x\mu_x = m_y\mu_y = m_z\mu_z$.[1] The results of the calculations are shown in Fig. 5-3, with the corresponding values of ζ^*_{opt} in Fig. 5-4. The calculations were done for values of a starting from 5 Å, since it is unlikely that much narrower wires can be made for Bi_2Te_3 since the a_0 dimension of the unit cell is 4.3 Å [2]. For values of $a < 10$ Å, phonon scattering off the surface will reduce κ_{ph} from the bulk value, so κ_{ph} was estimated using Eq. (4.23) with $l = a$ as with the 2D case.

---

[1] The bulk value of μ_x was used. This is actually a conservative estimate since it is likely that the 1D mobility will be higher than the 3D mobility due to the reduction in the range of phonon wave vectors that can participate in electron-phonon scattering. A higher μ_x will give a higher B and therefore a higher ZT than we have calculated.

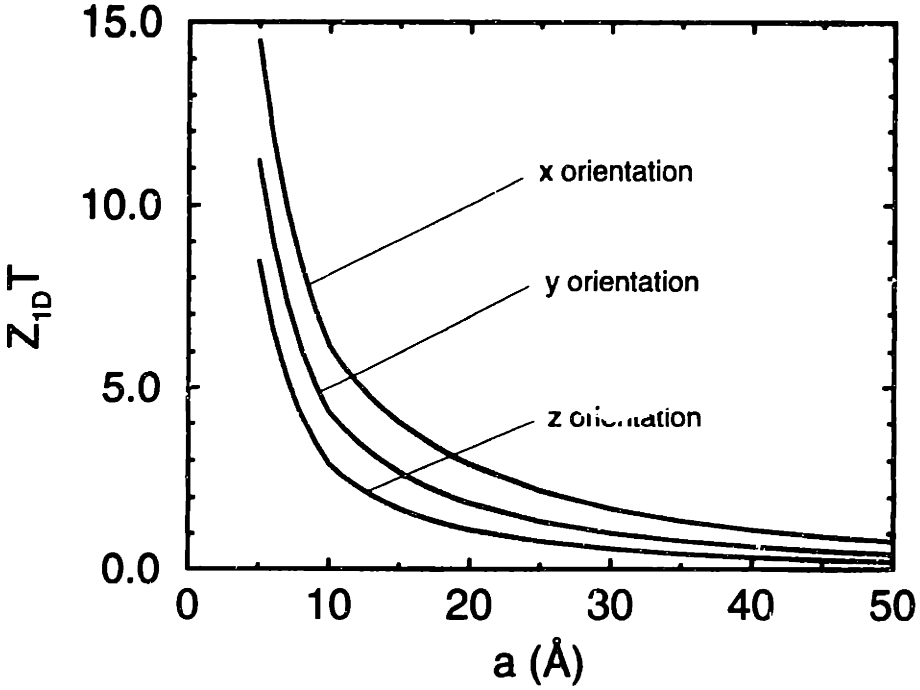

Figure 5-3: Plot of $Z_{1D}T(\zeta^*_{\text{opt}})$ vs wire width a for 1D wires of Bi_2Te_3 fabricated along the x, y and z directions.

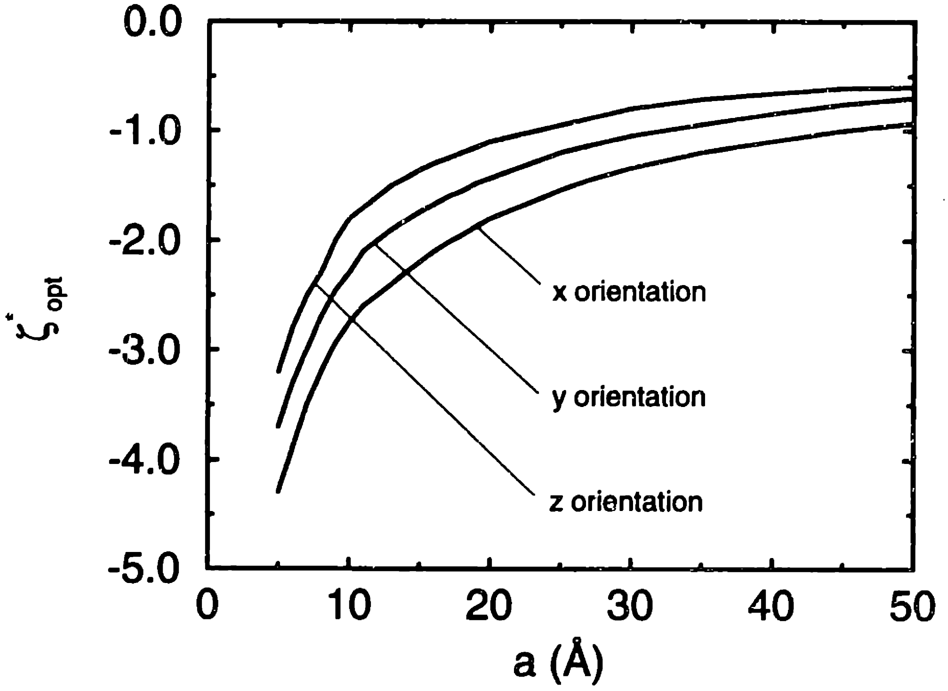

Figure 5-4: Plot of ζ^*_{opt} vs wire width a for 1D wires of Bi_2Te_3 fabricated along the x, y and z directions.

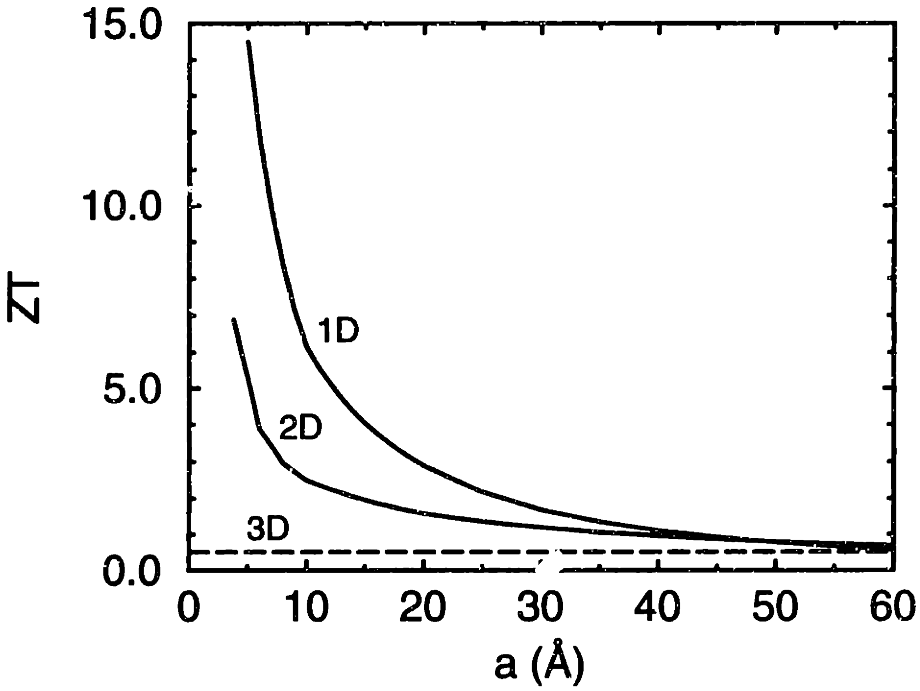

Figure 5-5: Comparison of the calculated ZT values for 1D quantum wire, 2D quantum well, and 3D bulk Bi_2Te_3. The 1D plot is for the highest ZT x-direction and the 2D plot is for the highest ZT a_0-c_0 orientation.

Before any conclusions can be drawn, it is necessary to check the validity of the results by making sure that $\zeta^*_{\rm opt}$ does indeed lie below the energy of the second subband. From Fig. 5-4, $\zeta^*_{\rm opt}$ is always negative, so it lies even lower than the lowest subband, so the results calculated using a one-band model are valid.

From Fig. 5-3, for a given value of a, $Z_{1D}T$ for the wire in the x direction is always higher than for the other two directions. This is expected since the highest mobility direction is along the x axis. For all three orientations, $Z_{1D}T$ increases significantly with decreasing a. A value of $Z_{1D} \simeq 14$ was calculated for a wire of width 5Å oriented in the x direction. Figure 5-5 shows a comparison of the calculated ZT values for 1D, 2D and 3D Bi_2Te_3. So the maximum ZT for a 1D wire is considerably greater than the maximum ZT for both the 3D bulk material and a 2D quantum well.

These results indicate that a significant increase in ZT can be achieved by going to lower dimensions, with the highest ZT occurring in 1D. This increase is due mainly to the change in the density of states, but an additional factor is the reduced lattice thermal conductivity due to increased phonon surface scattering. It may not be easy, however, to fabricate one-dimensional wires of Bi_2Te_3 of the required thickness. One possibility may be to encapsulate the thermoelectric material in a carbon nanotube type system, but one with a low thermal conductivity. In order to get sufficient cooling capacity from the use of quantum wires, one will need to use arrays of 1D quantum wires.

5.3 Zero-dimensional systems

Recently there has been much interest in the study of zero-dimensional (0D) systems, such as nanoparticles and quantum dots [11]. Although an increase in Z over bulk materials may be achieved by going to 2D and 1D structures, one is unlikely to find any increase in Z on going to 0D systems. This is because, by definition, there can be no transport in a perfect 0D system and so the Z is zero. In actual quantum-dot arrays, however, transport does occur by hopping or tunneling from one dot to the next [12]. When this transport occurs, the system is no longer a 0D system for transport, and it can be treated a 1D, 2D or 3D system, depending on the number of dimensions in which this transport occurs. However, the hopping and tunneling mechanisms result in a much lower mobility than the band transport I have considered in the last 3 chapters. This will result in a much lower Z for quantum dots than for the best 1D, 2D and 3D materials, which all have high mobility band transport.

Chapter 6

Superlattices of nonconventional thermoelectric materials

In Chapter 4, I considered the effect on ZT of using a one-band thermoelectric material such as Bi_2Te_3 in a two-dimensional (2D) quantum-well superlattice. My calculations showed that this approach could yield a significant increase in ZT within the quantum wells. In those earlier calculations, I assumed a one-band model since one-carrier systems give the best ZT for bulk materials. For two-band (mixed-conduction) materials such as semimetals, both electrons and holes contribute to the conduction. As described in Chapter 3, the contributions of equal numbers of electrons and holes to the Seebeck coefficient tend to cancel each other out (because they are of opposite sign), resulting in a low overall ZT. The positions of the conduction and valence bands for a semimetal are shown in Fig. 6-1. Note the overlap of the conduction and valence bands, with the Fermi level at a position resulting in approximately equal contributions of both electrons and holes to the conduction.

Although the overall ZT of mixed-conduction materials is low, the contribution of the conduction band or valence band individually to the ZT may be high. In fact, Gallo *et al.* [13] have shown that bismuth, a semimetal with a low ZT, could have a ZT of nearly 2 if it were somehow possible to remove the holes from the system. Quantum-well superlattices provide a mechanism to effectively remove the holes from the system, as described below.

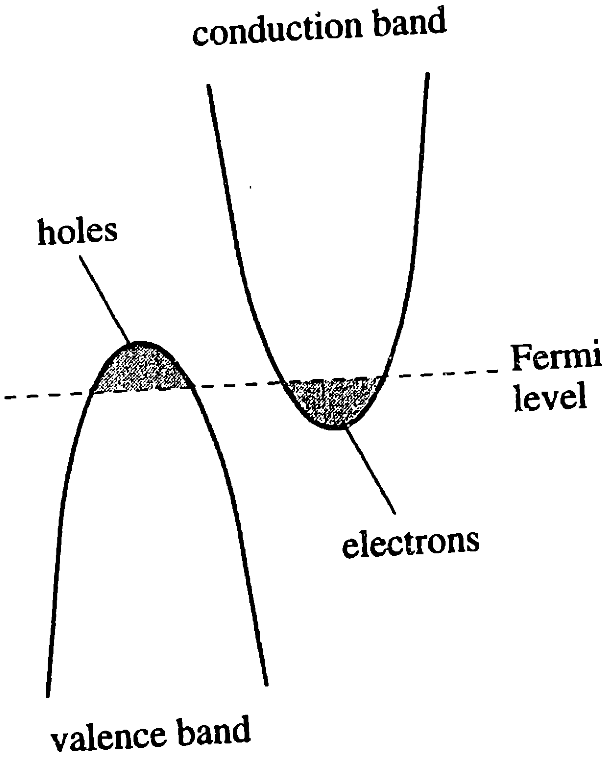

Figure 6-1: Conduction and valence bands in a semimetal.

When a material is prepared in a quantum well, the confinement effects result in electronic bound states in the confinement direction with energies

$$E_n = \frac{n^2\hbar^2\pi^2}{2m_z a^2}, \tag{6.1}$$

for infinite potential barriers along the z-direction. As the quantum well width a is reduced, the electrons energies E_n increase. For holes, the same effect occurs, except since holes can be thought of as negative energy electrons, this means that the hole energies become more negative as the quantum well width is reduced. This means that electron energies are pushed upward and hole energies are pushed downwards, as shown in Fig. 6-2 which shows the positions of the $E_{n=1}$ bound states of both the electrons and holes. Below a critical well width, the $E_{n=1}$ energy for the electrons will be higher than the hole $E_{n=1}$ energy. Since the $E_{n=1}$ state is the lowest electron energy and the highest hole energy, this means that the two bands have been separated

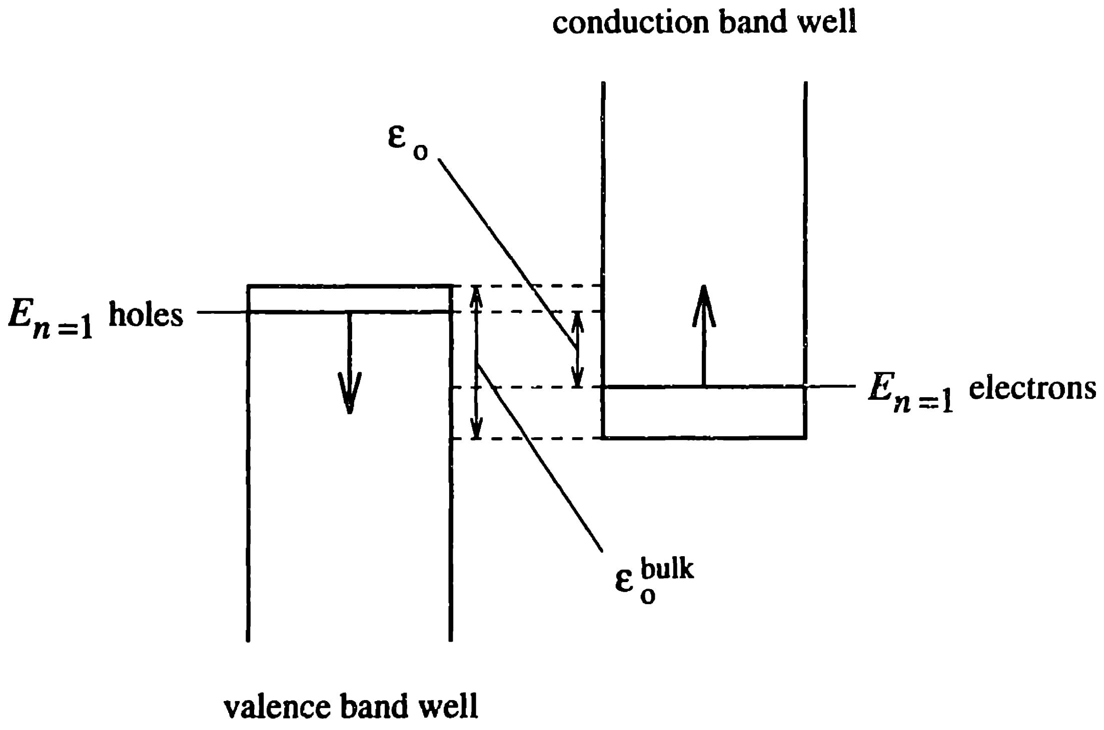

Figure 6-2: Semimetal-semiconductor transition occurs when $E_{n=1}$ for electrons crosses $E_{n=1}$ for holes.

and the material has undergone a semimetal-semiconductor transition. If the well is narrowed further, the electron and hole bands can be separated further and the Fermi level can be positioned by doping to lie closer to either the conduction or valence band to create an effectively one-band material. This semimetal-semiconductor transition has been demonstrated experimentally with HgTe/CdTe superlattices [14].

For Bi and other semimetals, this is a method to eliminate the contribution of the holes to the transport and take advantage of the especially good thermoelectric properties of the conduction band. Thus, some mixed conduction materials, which do not have a high bulk ZT, may be good thermoelectric materials in the form of 2D quantum-well superlattices.

In this chapter, calculations have been performed to investigate the effect on ZT of preparing a two-band material in the form of a 2D quantum well.

6.1 Z for a two-band material in a quantum-well

Equations (3.1)-(3.3) are now used to derive expressions for S, σ and κ_e for two-band material, taken to be the lowest subbands of the conduction band and valence band in a 2D quantum well. The layers are in the x-y plane and conduction is along the x-direction. Since this is a multiband system, each of the $\mathbf{L}^{(\alpha)}$'s in Eqs. (3.1)-(3.3) must be replaced by the sum of a contribution from the conduction band and one from the valence band. Equations (4.11)-(4.13) give the contribution of one band in a 2D quantum well to the total $\mathbf{L}^{(\alpha)}$. So for both bands, the total $\mathbf{L}^{(\alpha)}$'s are given by

$$
\begin{aligned}
L^{(0)}_{xx} &= D_{ex}[F_0^e] + D_{hx}[F_0^h], && (6.2)\\
L^{(1)}_{xx} &= (k_BT)\left(D_{ex}[2F_1^e - \zeta_e^* F_0^e] + D_{hx}[2F_1^h - \zeta_h^* F_0^h]\right), && (6.3)\\
L^{(2)}_{xx} &= (k_BT)^2\left(D_{ex}[3F_2^e - 4\zeta_e^* F_1^e + \zeta_e^{*2} F_0^e] + D_{hx}[3F_2^h - 4\zeta_h^* F_1^h + \zeta_h^{*2} F_0^h]\right), && (6.4)
\end{aligned}
$$

where the subscripts e and h are used to denote the contributions of the electrons and holes, respectively, and

$$
\begin{aligned}
D_{ex} &= \frac{e}{2\pi a}\left(\frac{2k_BT}{\hbar^2}\right)(m_{ex}m_{ey})^{\frac{1}{2}}\mu_{ex}, && (6.5)\\
D_{hx} &= \frac{-e}{2\pi a}\left(\frac{2k_BT}{\hbar^2}\right)(m_{hx}m_{hy})^{\frac{1}{2}}\mu_{hx}, && (6.6)
\end{aligned}
$$

where we note that D_{ex} and D_{hx} have opposite signs. The Fermi-Dirac functions F_i are given by

$$F_i = F_i(\zeta^*) = \int_0^\infty \frac{x^i dx}{e^{(x-\zeta^*)}+1}. \qquad (6.7)$$

In the above expressions, $F_i^e = F_i(\zeta_e^*)$ and $F_i^h = F_i(\zeta_h^*)$ where ζ_e^* and ζ_h^* are the reduced chemical potentials of the electrons and holes. ζ_e^* and ζ_h^* are related by the expression $\zeta_e^* + \zeta_h^* = \varepsilon_o/k_BT$, where ε_o is the energy overlap of the lowest electron and lowest hole bound states (Fig. 6-2). The energy overlap ϵ_o is positive for a semimetal and negative for a semiconductor and is related to the band overlap in the bulk material ϵ_o^{bulk} by

$$\epsilon_o = \epsilon_o^{\text{bulk}} - \frac{\hbar^2\pi^2}{2m_{ez}a^2} - \frac{\hbar^2\pi^2}{2m_{hz}a^2}. \tag{6.8}$$

Since

$$Z = \frac{S^2\sigma}{\kappa_e + \kappa_{ph}}, \tag{6.9}$$

Eqs. (3.1)-(3.3) give

$$Z_{2D} = \frac{(1/e^2T^2)\left(L_{xx}^{(1)}/L_{xx}^{(0)}\right)^2 L_{xx}^{(0)}}{(1/e^2T)\left(L_{xx}^{(2)} - L_{xx}^{(1)2}/L_{xx}^{(0)}\right) + \kappa_{ph}}, \tag{6.10}$$

or

$$Z_{2D}T = \frac{L_{xx}^{(1)2}}{\left(L_{xx}^{(2)} + \kappa_{ph}e^2T\right)L_{xx}^{(0)} - L_{xx}^{(1)2}}. \tag{6.11}$$

Dividing numerator and denominator by $k_B^2T^2D_{ex}$ gives the following expression for the figure of merit within the quantum well, assuming total carrier confinement within the quantum well:

$$Z_{2D}T = \frac{M_1^2}{M_2M_0 - M_1^2}, \tag{6.12}$$

where

$$M_0 = F_0^e + CF_0^h, \tag{6.13}$$

$$M_1 = (2F_1^e - \zeta_e^*F_0^e) - C(2F_1^h - \zeta_h^*F_0^h), \tag{6.14}$$

$$M_2 = (3F_2^e - 4\zeta_e^*F_1^e + \zeta_e^{*2}F_0^e) + C(3F_2^h - 4\zeta_h^*F_1^h + \zeta_h^{*2}F_0^h) + B^{-1}, \tag{6.15}$$

and

$$B = \frac{1}{2\pi a}\left(\frac{2k_BT}{\hbar^2}\right)(m_{ex}m_{ey})^{\frac{1}{2}}\frac{k_B^2T\mu_{ex}}{e\kappa_{ph}}, \tag{6.16}$$

$$C = \left(\frac{m_{hx}m_{hy}}{m_{ex}m_{ey}}\right)^{\frac{1}{2}}\left(\frac{\mu_{hx}}{\mu_{ex}}\right), \tag{6.17}$$

a is the layer thickness, m_{ex}, m_{ey}, m_{ez} and m_{hx}, m_{hy}, m_{hz} are the principal effective mass tensor components for the electrons and holes, respectively, μ_{ex} and μ_{hx} are the electron and hole mobilities, respectively, in the direction of conduction, and κ_{ph} is the lattice thermal conductivity.

The expression for B in Eq. (6.16) is identical to that of B_{2D} in Eq. (4.22) of Chapter 4, but that there is an extra parameter C in the expression for $Z_{2D}T$ related to the hole properties. For given values of B and C, the reduced electron and hole chemical potentials ζ_e^* and ζ_h^* may be varied to change the value of $Z_{2D}T$. The maximum value of $Z_{2D}T$ occurs when $\zeta_e^* = \zeta_{e(\mathrm{opt})}^*$ and $\zeta_h^* = \zeta_{h(\mathrm{opt})}^*$. B and C are determined largely by the intrinsic properties of the material, but ζ_e^* and ζ_h^* may be varied by doping. To maximize $Z_{2D}T$ for a material, one first calculates B and C for the intrinsic material, then determines the values of ζ_e^* and ζ_h^* which maximize $Z_{2D}T$ for these values of B and C. The next step is to adjust ζ_e^* and ζ_h^* by doping so that $\zeta_e^* = \zeta_{e(\mathrm{opt})}^*$ and $\zeta_h^* = \zeta_{h(\mathrm{opt})}^*$. Note that ζ_e^* and ζ_h^* are not independent since $\zeta_e^* + \zeta_h^* = \varepsilon_o/k_BT$. So one needs to optimize only one of ζ_e^* or ζ_h^* to optimize $Z_{2D}T$.

6.2 Calculated Z for a quantum well superlattice of semimetal Bi

As mentioned earlier, Bi would be a good thermoelectric material if it were not for the overlap of the conduction and valence bands, resulting in a relatively low ZT of about 0.1 [13]. Equations (6.12)-(6.17), suitably modified to take into account the anisotropic Fermi surface of Bi, are now used to calculate $Z_{2D}T$ for Bi in a 2D quantum well.

Bi has a rhombohedral lattice, which can be expressed in terms of a hexagonal unit cell of lattice parameters $a_0 = 4.5$ Å and $c_0 = 11.9$ Å [15]. Electrons are distributed in 3 equivalent ellipsoids at the L points of the Brillouin zone and the holes in a single ellipsoid at the T point [16]. The overlap energy of the electron and hole bands in bulk Bi is $\epsilon_0^{\mathrm{bulk}} = 0.038$ eV [17]. The principal effective mass tensor components are $m_{ex} = 0.00651m_0$, $m_{ey} = 1.362m_0$, $m_{ez} = 0.00993m_0$ for the electrons located at the three L point pockets, and $m_{hx} = 0.0644m_0$, $m_{hy} = 0.0644m_0$, $m_{hz} = 0.696$ for the holes [17] located at a single T point in the Brillouin zone (see Fig. 6-3). The

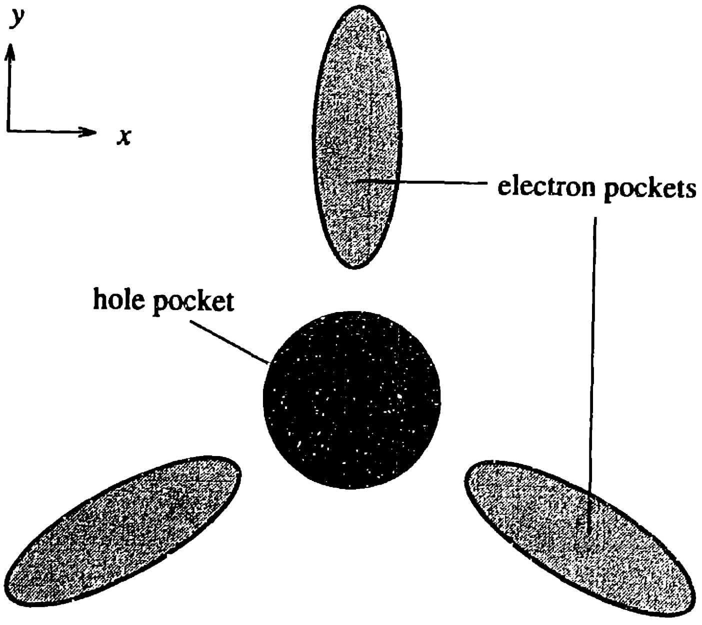

Figure 6-3: Bismuth carrier pockets.

principal mobility components (in $m^2V^{-1}s^{-1}$) at 300 K are $\mu_{ex} = 3.5$, $\mu_{ey} = 0.034$, $\mu_{ez} = 1.4$ for the electrons and $\mu_{hx} = 0.58$, $\mu_{hy} = 0.58$, $\mu_{hz} = 0.45$ for the holes [18]. The lattice thermal conductivity is $\kappa_{ph} = 0.9$ $Wm^{-1}K^{-1}$ [13].

The equation for $Z_{2D}T$ derived so far assumed a single electron pocket and a single hole pocket in the Brillouin zone. Bi has a single hole pocket, but has 3 electron pockets, each oriented at 120° to the other 2 pockets in the x-y (a_0-b_0) plane (Fig. 6-3). This will result in a slight change in the coefficients B and C [Eqs. (6.16) and (6.17)]. If we assume that the superlattice layers are made in the Bi x-y plane (the reasons for this are explained below), then after taking into account all 3 electrons pockets and solving for transport in the x-direction, $(m_{ex}m_{ey})^{\frac{1}{2}}$ becomes $3(m_{ex}m_{ey})^{\frac{1}{2}}$ and μ_{ex} becomes $(\mu_{ex} + \mu_{ey})/2$ in Eqs. (6.16) and (6.17).

Since $Z_{2D}T(\zeta^*_{e(\mathrm{opt})}, \zeta^*_{h(\mathrm{opt})})$ increases monotonically with B (Chapter 4), the orientation which will give the best $Z_{2D}T$ has the highest value for $\mu(m_{e1}m_{e2})^{\frac{1}{2}}$, where the subscripts 1 and 2 denote the x, y or z axes. The highest electron effective mass component for Bi is m_{ey} and the highest electron mobility component is μ_{ex}, so that

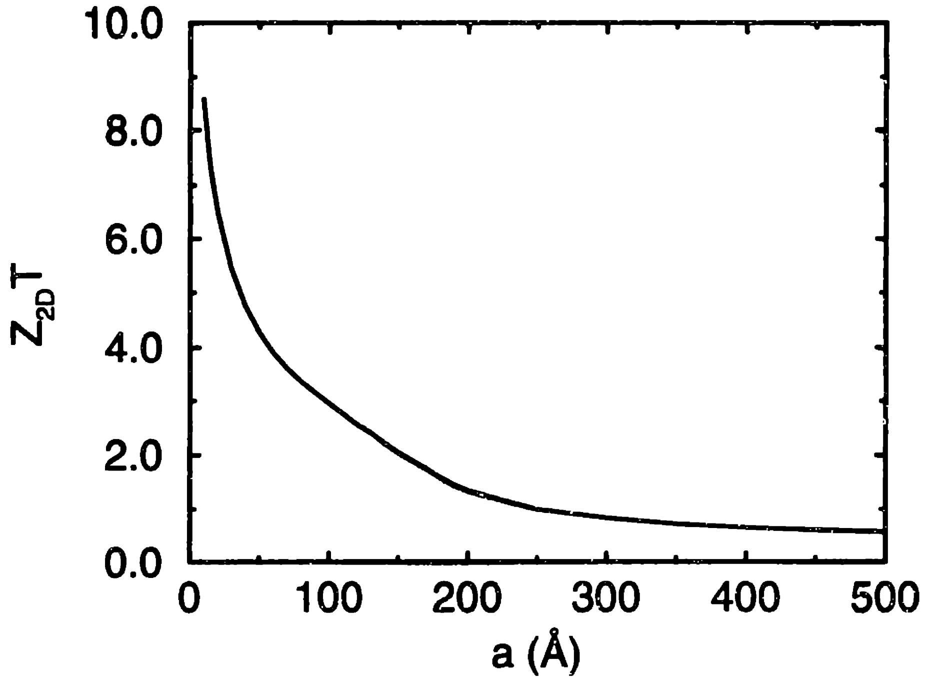

Figure 6-4: Plot of $Z_{2D}T$ vs layer thickness a for a quantum well of Bi fabricated in the x-y plane.

the best layer orientation is the one which contains both the x and y directions, the x-y plane. Fortunately, this orientation is also the preferred growth direction for Bi films [19].

The optimum figure of merit $Z_{2D}T$ was calculated numerically at 300 K as a function of layer thickness a for quantum wells of Bi fabricated in the x-y plane. The results for $Z_{2D}T$ for a Bi quantum well at 300 K are shown in Fig. 6-4. The calculations were done for values of a down to 10 Å, which is just less than the length of the c_0-axis lattice parameter. Bi layers of about this thickness have been deposited in a Bi/PbTe modulated structure [20]. However, the films were polycrystalline and disordered so work needs to be done to obtain high mobility 2D transport in Bi films.

From Fig. 6-4, $Z_{2D}T$ increases with decreasing a. $Z_{2D}T$ starts to increase when the electron and hole bands uncross at about 300 Å, reaching a value of over 8 for quantum wells of thickness 10 Å. Thus it may be possible to obtain a large increase in $Z_{2D}T$ within the quantum well over the bulk value. For Bi layers less than 100 Å thick, the optimum $Z_{2D}T$ is almost identical to that calculated by assuming transport by the electrons alone. This is not surprising since the partial ZT for the electrons is higher than that for the holes [13] and at these layer thicknesses the band gap is large enough to create an effectively one-carrier material. Note that there are now *two* different factors responsible for the large increase in $Z_{2D}T$ over the bulk value. The first is the separation of the two bands and the transformation of the material to an effectively one-band system. The second is the increase in $Z_{2D}T$ due to the 2D nature of the density of states. This density of states factor is responsible for the increase in $Z_{2D}T$ in one-band materials (Chapter 4). In Chapter 4, I calculated a $Z_{2D}T \simeq 5$ for a 10-Å-thick quantum well of Bi_2Te_3, the material with the best current bulk ZT. So even though Bi has a much lower bulk ZT than Bi_2Te_3, it has a *higher* $Z_{2D}T$ when both materials are used in quantum-well superlattices of equal well widths.

Another significant point to note from Fig. 6-4 is that Bi quantum wells exhibit a $Z_{2D}T > 1$ at relative wide quantum well thicknesses of 200 Å. From Fig. 4-5, Bi_2Te_3 quantum wells do not give a $Z_{2D}T$ above unity until they are narrower than 50 Å. Therefore it may be more experimentally feasible to grow and use Bi quantum wells for high ZT applications than Bi_2Te_3 quantum wells.

These results elucidate an important additional use of superlattices to obtain a high ZT. I have shown that to obtain a high $Z_{2D}T$, it may not be necessary to use materials which already have a high bulk ZT. This opens the possibility of using a new class of thermoelectric materials as refrigeration elements, and one does not necessarily have to be restricted to materials which already show a high bulk ZT.

6.3 $Bi_{1-x}Sb_x$ alloys

Although Bi has poor thermoelectric properties, the addition of some Sb to form $Bi_{1-x}Sb_x$ alloys improves ZT considerably [2]. This is because the addition of a small amount of Sb reduces the overlap of the conduction and valence bands. For a range of compositions the bands are uncrossed and there is a positive energy gap. This means that even though Bi is a semimetal, $Bi_{1-x}Sb_x$ is a semiconductor for a range of x. The band structure of $Bi_{1-x}Sb_x$ alloys is shown in Fig. 6-5 [21].

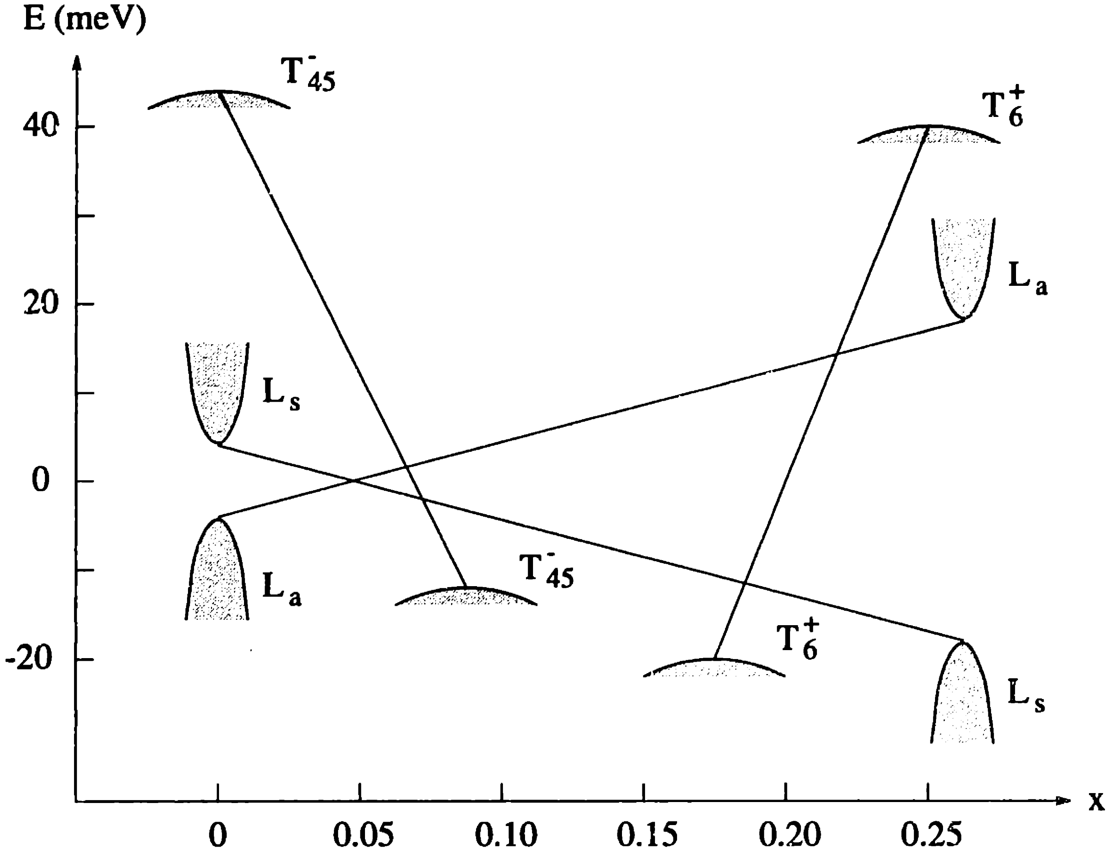

Figure 6-5: Variation of the energy spectrum of $Bi_{1-x}Sb_x$ alloys in the range $0 < x < 0.25$.

Figure 6-5 shows that the band edge of the overlapping hole band T_{45}^{-} is lowered on addition of Sb to Bi until at about $x = 0.065$, it moves below the L-point conduction band edge, making the material a semiconductor. Further addition of Sb causes the T_6^{+} hole band to rise until at about $x = 0.22$, it rises above the L-point conduction band edge and the material is once again a semimetal. The material remains a semimetal for $x > 0.22$. The L-point electron and hole bands also move with increasing x. As Sb is added to Bi, the L-point band gap decreases until is reaches zero at $x = 0.05$. At this point, the bands invert and move apart again as shown in Fig. 6-5.

In the semiconducting region $0.065 < x < 0.22$, the thermoelectric properties are much more favorable since the electrons and holes no longer cancel each other out in their contribution to S, so ZT is higher than for pure Bi. The highest ZT obtained is 0.3 at 300 K [2] in $\text{Bi}_{0.88}\text{Sb}_{0.12}$. This corresponds to the point where the T-point hole bands are furthest away from the L-point conduction band. ZT is even higher at low temperatures (0.4 at 80 K [2]), so $\text{Bi}_{1-x}\text{Sb}_x$ alloys with $0.065 < x < 0.22$ are commonly used in applications, especially at low temperature.

Another reason why the addition of Sb causes an increase in ZT is the reduction in thermal conductivity due to point-defect scattering caused by the difference in masses of the Bi and Sb atoms. The addition of 12% Sb to Bi reduces the thermal conductivity by 20% [22].

Since $\text{Bi}_{1-x}\text{Sb}_x$ alloys have similar physical properties to pure Bi, but have a higher band gap and lower thermal conductivity, they would likely have a higher ZT in a 2D quantum-well superlattice than pure Bi in a similar superlattice. ZT was calculated for a $\text{Bi}_{0.88}\text{Sb}_{0.12}$ quantum well at 300 K and the results are shown in Fig. 6-6 together with the results for pure Bi. $\text{Bi}_{0.88}\text{Sb}_{0.12}$, with a band gap of 14 meV [2], is the best alloy in bulk form and is also likely to be the best 2D material since it is the composition where the T-point holes are furthest away from the L-point conduction band. Although the effective masses of $\text{Bi}_{0.88}\text{Sb}_{0.12}$ are slightly different from those for Bi, this does not affect the ZT since the change is canceled by the corresponding change in the mobility as shown in Eq. 6.17. Figure 6-6 shows that

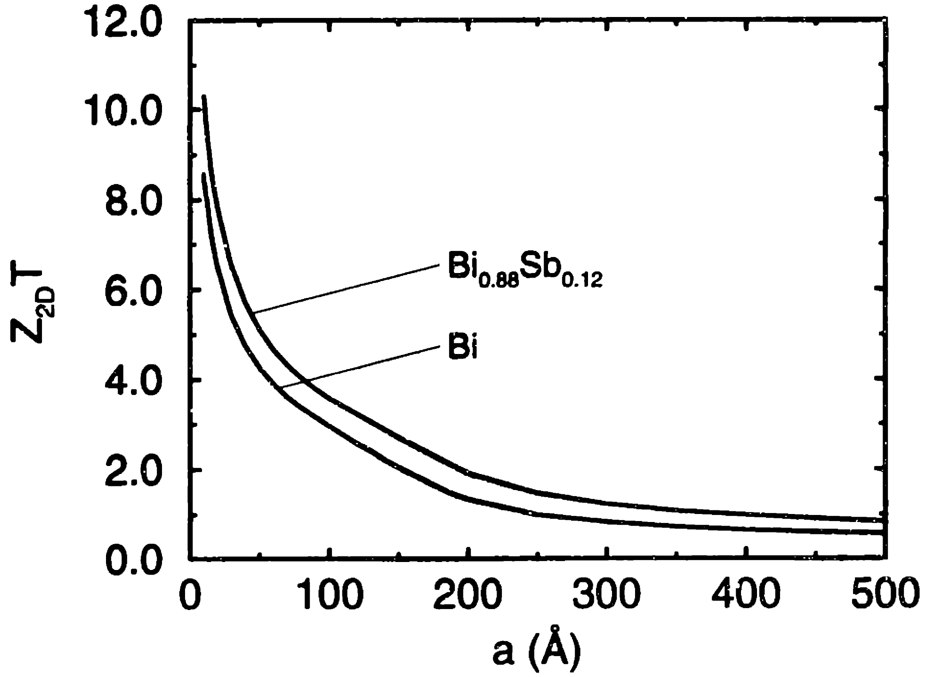

Figure 6-6: Calculated ZT for both $Bi_{0.88}Sb_{0.12}$ and pure Bi.

the calculated ZT for $Bi_{0.88}Sb_{0.12}$ is higher than for Bi at all thicknesses. There are two reasons for this increase. Since the quantum well enhancement of ZT in Bi relies on using quantum-confinement effects to separate the bands, a $Bi_{1-x}Sb_x$ alloy well will have a higher ZT than a Bi well of equal thickness because for $Bi_{1-x}Sb_x$ alloys with $0.065 < x < 0.22$ the bands are already separated. In addition, the thermal conductivity for $Bi_{1-x}Sb_x$ alloys is less than for pure Bi, resulting in a higher ZT.

Chapter 7

Experimental Investigation

In the preceding chapters, I have shown theoretically that it may be possible to increase Z of certain materials by preparing them in the form of 2D quantum-well superlattices. I have also conducted an experimental investigation to test my theoretical predictions.

7.1 Choice of system

Since Bi_2Te_3 is the best thermoelectric bulk material, it would appear to be a natural candidate for use in a thermoelectric quantum-well system. However, I have shown in Chapter 6 that Bi or $Bi_{1-x}Sb_x$ would be a better 2D thermoelectric material than Bi_2Te_3 due to the band separation that occurs in quantum-confined systems, so a Bi quantum well would seem to be the ideal system. However, no one has yet succeeded in growing 2D quantum wells of Bi, $Bi_{1-x}Sb_x$ or Bi_2Te_3, and significant materials science and growth problems remain to be overcome. The main problem is the appropriate choice of barrier material. A good barrier material for thermoelectric superlattices is one which satisfies the following criteria:

- Lattice-matching with the well material and a similar thermal expansion coefficient to the well material. These are needed to provide sharp interfaces which do not degrade the well mobility.

- A sufficiently large band gap and thickness to confine electrons in the quantum well.
- Does not degrade the electronic properties of the quantum well material.
- Low thermal conductivity to minimize barrier heat conduction which would decrease the overall Z compared to the Z of the well alone.

In collaboration with Dr. Ted Harman of M.I.T. Lincoln Laboratory, we tried using PbTe and $\mathrm{PbTe}_{1-x}\mathrm{Se}_x$ as the barrier material in Bi/PbTe and $\mathrm{Bi}_{1-x}\mathrm{Sb}_x/\mathrm{PbTe}_{1-x}\mathrm{Se}_x$ structures grown by molecular beam epitaxy. PbTe is closely lattice-matched with Bi and has a very low thermal conductivity. Unfortunately, we were unable to obtain any degree of carrier control in the system since it appeared that the PbTe would dope the Bi and vice versa. This lack of control of carrier density meant that we were unable to obtain the optimum doping needed to test the thermoelectric theories. Therefore, we decided to use the $\mathrm{PbTe}/\mathrm{Pb}_{1-x}\mathrm{Eu}_x\mathrm{Te}$ system for the experimental investigation.

7.2 $\mathrm{PbTe}/\mathrm{Pb}_{1-x}\mathrm{Eu}_x\mathrm{Te}$ superlattices

The multiple-quantum-well (MQW) superlattice system used for the investigation is the $\mathrm{PbTe}/\mathrm{Pb}_{1-x}\mathrm{Eu}_x\mathrm{Te}$ system. This system was chosen for our thermoelectric investigation for the following reasons. Firstly, the fabrication technology is relatively well-developed, making it possible to grow samples with high mobility, 2D transport and to have precise control over the carrier density. Secondly, bulk PbTe is a relatively good thermoelectric material with a ZT of 0.4 at 300 K, so that a reasonable increase in Z due to 2D effects could perhaps result in a Z higher than the best bulk $\mathrm{Bi}_2\mathrm{Te}_3$ alloys. In the $\mathrm{PbTe}/\mathrm{Pb}_{1-x}\mathrm{Eu}_x\mathrm{Te}$ system, the PbTe is the quantum well and $\mathrm{Pb}_{1-x}\mathrm{Eu}_x\mathrm{Te}$ is the barrier material. Such structures have a type I band alignment and a nearly symmetric offset between valence and conduction bands [23] as shown in Fig. 7-1. The energy gap of the $\mathrm{Pb}_{1-x}\mathrm{Eu}_x\mathrm{Te}$ barrier increases strongly with x, the Eu content as shown in Fig. 7-2 [24], so only about 5% Eu can give large confinement

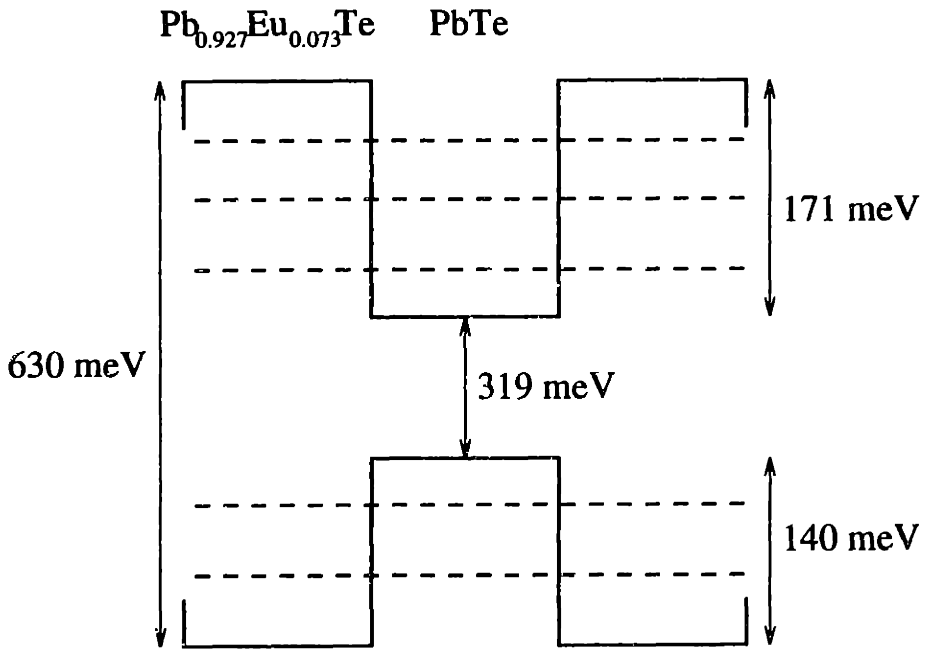

Figure 7-1: Conduction and valence bands in a PbTe/$Pb_{0.927}Eu_{0.073}Te$ superlattice. The band gaps for the quantum well and for the barrier are given, as well as the band offsets (using results from Ref. [23]) for the valence and conduction bands. The dashed lines schematically indicate bound states for the valence and conduction bands.

energies and yield 2D transport for electrons in the PbTe quantum wells [25]. The mobility of $Pb_{1-x}Eu_xTe$ also decreases rapidly with increasing Eu content [25].

7.3 Sample preparation

My proposed increase in Z in MQW structures occurs in the quantum wells alone. In order to extract easily the well transport properties from the MQW results, we needed to grow samples for which transport is dominated by 2D conduction in the wells, with negligible tunneling through the barriers or parallel barrier conduction. Two factors control the extent of electron confinement in the quantum well. The first is the band gap of the barrier. A wide band gap leads to large potential barriers and increased confinement for the well electrons. The second factor is the barrier thickness. As the barrier thickness is increased, the overlap of wavefunctions between adjacent wells is reduced, leading to predominantly 2D transport in the well with

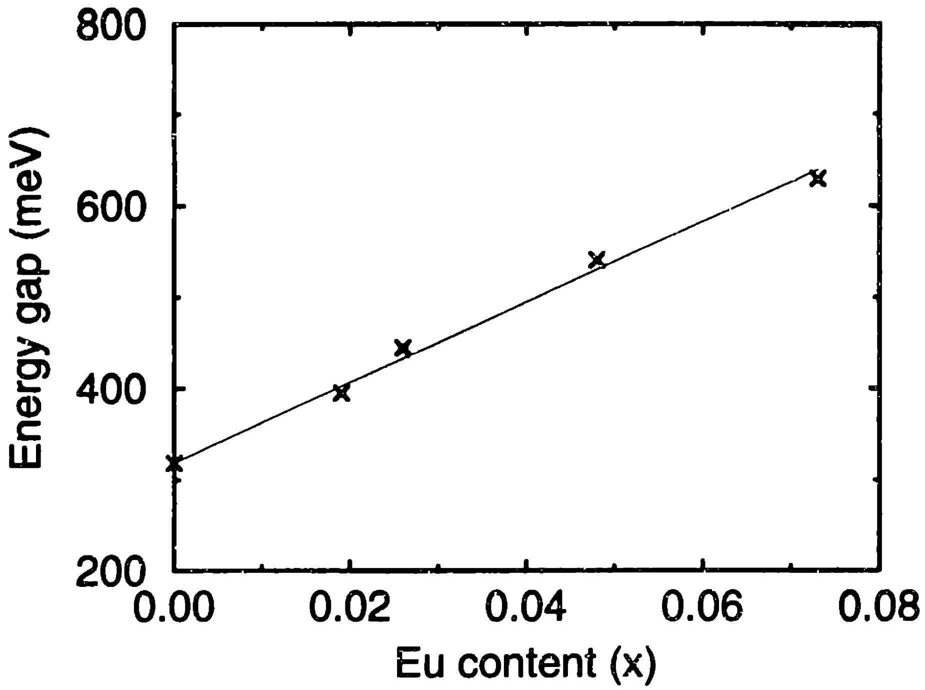

Figure 7-2: Bandgap of $Pb_{1-x}Eu_xTe$ at 300 K as a function of Eu content x. The point at $x = 0.073$ was obtained by infrared transmission measurements, and the other points were obtained from Ref. [24].

and minimal tunnelling through the barriers. Since the barriers do not contribute to the electronic transport, but reduce the overall Z by contributing to the lattice thermal conductivity, it is desirable to find the minimum barrier thickness which will result in predominantly 2D conduction. Clearly this minimum thickness will decrease as the barrier band gap increases so we would want as large a barrier bandgap as possible. The band gap of $Pb_{1-x}Eu_xTe$ can be increased by increasing Eu content x [24] (see Fig. 7-2). However, we found experimentally that above about $x = 7.3$ %, the increased lattice mismatch between the barrier and PbTe well results in interfacial dislocations and reduced mobilities for MQW samples [26]. For an $x = 0.073$ barrier, we measured the mobilities of samples with a constant well thickness of 20 Å and a gradually increasing barrier thickness from 70 Å to 560 Å. We found that the mobility of the MQW samples increased as the barrier thickness was increased up to about 400 Å, after which the mobility remained unchanged as shown in Fig. 7-3. Since the mobility of our bulk PbTe samples (1600 $cm^2V^{-1}s^{-1}$) is much greater

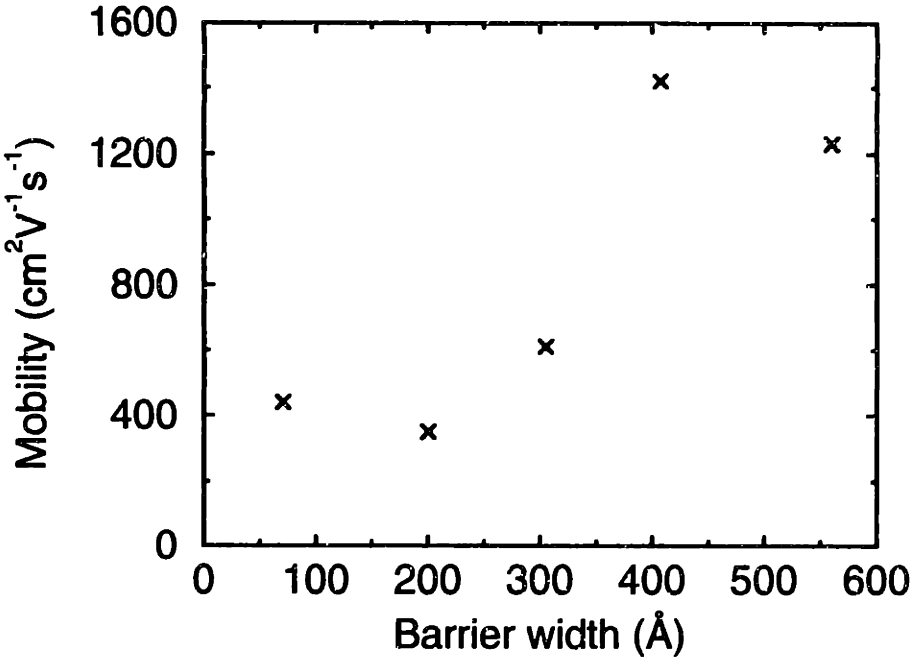

Figure 7-3: Mobilities of carriers in PbTe/Pb$_{1-x}$Eu$_x$Te superlattices with 20 Å wells and different barrier widths.

than that of our bulk Pb$_{1-x}$Eu$_x$Te (45 cm^{2}V^{-1}s^{-1}), these results show that at lower barrier thicknesses, there is still tunneling and transport in the barrier material, which results in a significantly lower overall MQW mobility than bulk PbTe. However as the barrier thickness is increased, there is less tunneling and the mobility increases until it is comparable to bulk PbTe at a barrier thickness of about 400 Å. Above 400 Å thickness, there is no further increase showing that all the electronic transport is now in the well alone and that the barrier thickness has no influence on the overall MQW mobility. So for all our samples used for thermoelectric measurements, we used a barrier composition of Pb$_{0.927}$Eu$_{0.073}$Te and a barrier thickness of at least 400 Å.

Samples of PbTe/Pb$_{1-x}$Eu$_x$Te MQW superlattices were grown by Dr. Harman of M.I.T. Lincoln Laboratory using molecular beam epitaxy (MBE) in a modified Varian 360 MBE system. Details of the sample preparation and characterization are given elsewhere [27]. Briefly, first a Pb$_{0.958}$Eu$_{0.042}$Te buffer of about 2000 Å was deposited on a freshly cleaved BaF$_2$(111) substrate to ensure complete strain relaxation and high structural perfection of the layer. Next, samples with periods of 100 to 150 of

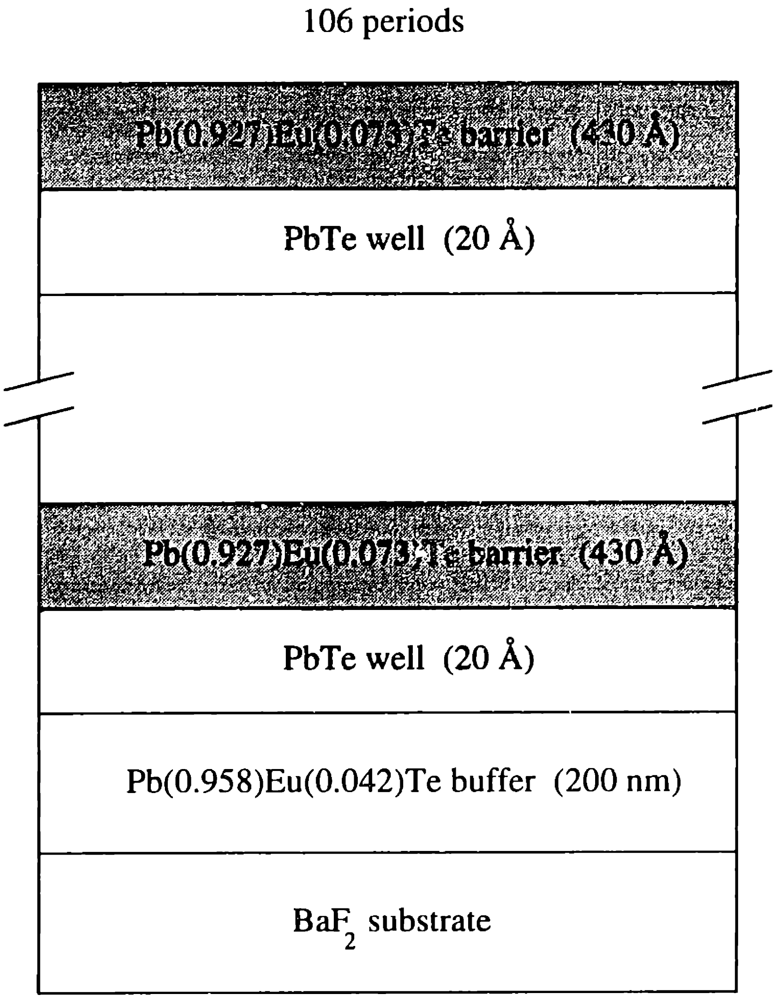

Figure 7-4: A 106-period 20Å/430Å PbTe/$Pb_{0.927}Eu_{0.073}Te$ superlattice grown on a BaF_2 substrate and a relatively thin $Pb_{0.958}Eu_{0.042}Te$ layer.

PbTe/$Pb_{0.927}Eu_{0.073}Te$ MQW structures were grown, with PbTe well widths varying between 17 Å and 55 Å, separated by wide $Pb_{0.927}Eu_{0.073}Te$ barriers of about 450 Å. Each layer was a single crystal with the (111) plane parallel to the layers. The carrier density was varied by using Bi donor atoms in the barrier material. This resulted in an n-type material so that all the electrical conduction is in the conduction band quantum well. A typical sample is shown in Fig. 7-4.

7.4 Transport measurements

According to the model, the increase in Z due to 2D effects arises mainly from an increase in the power factor $S^2\sigma$, while the lattice thermal conductivity is assumed to be unchanged from the bulk value except for well widths less than about 10 Å. However, even with well widths above than 10 Å, boundary scattering at the quantum well interfaces is expected to decrease the thermal conductivity, so that our estimate of the enhancement of Z is expected to be conservative. I also assumed in my calculations that the mobility of the quantum well would be the same as the best bulk value - an assumption which we confirmed experimentally as described above - so any increase in Z would arise through the factor S^2n (recall that $\sigma = ne\mu$), where n is the carrier density in the quantum well. Therefore, according to the model, we should be able to observe an increase in S^2n as the well width is narrowed.

The electrical conductivity, Seebeck coefficient and Hall coefficient of the MQW samples were measured at 300 K. The experimental setup for the conductivity and Seebeck measurements is shown in Fig. 7-5. This setup was designed to enable measurement of both σ and S on the same sample in the same orientation. It was used to measure temperature dependence (described later) from 300 K down to 4 K. The sample is soldered (using indium) between the heater and the copper heat sink. The heater is a copper block with 100 Ω of twisted pair resistance wire coiled tightly around it. The heater is supported by two low thermal conductivity ceramic rods. Wires A and F are gold wires used to carry the current for conductivity measurements. The wire pair B and C is a thermocouple: B is a chromel wire and C is a AuFe(0.07%) alloy wire. Wires D (chromel) and E (AuFe(0.07%)) are a second chromel-AuFe(0.07%) thermocouple. All wires are attached to the sample with indium, which results in excellent ohmic contacts. The other ends of the wires are connected to a copper plate to provide a common temperature reference. Care was taken to ensure that the wires attached to the copper plate are in good thermal contact but have no electrical contact with the copper plate. Copper wires are then used to connect the wires attached to the plate with the measuring devices (e.g. voltmeters). The diode is used to measure the temperature of the copper plate reference.

Conductivity measurements employed the four-probe technique: with the heater off, a d.c. current was passed though wires A and F and the voltage measured using wires C and E. The potential drop was measured for both forward and reverse currents to eliminate any thermoelectric effects. For Seebeck measurements, the heater was used to apply a temperature difference of several degrees to the sample and the specimen enclosure was evacuated to minimize heat loss. The two thermocouples were used to measure both the temperature difference (ΔT) between the two junctions on the sample, and the resulting Seebeck voltage (ΔV) between the junctions. The temperature difference was varied, the corresponding Seebeck voltage measured, and the Seebeck coefficient found from the slope of the line (after subtracting the contribution of the thermocouple wires). The setup for Hall measurements (used to determine carrier density and mobility) is shown in Fig. 7-6. The potentiometer was adjusted so as to give zero voltage V across the sample in the absence of the magnetic field. The Hall coefficient R_H was found from $R_H = E_y/j_x B$, where E_y is the transverse field (found from the potential difference V) induced across the sample by current j_x in field B. The field direction was reversed and E_y measured again to eliminate any errors due to longitudinal magnetoresistance.

Since we had already established that virtually all the conduction in our MQW samples is in the PbTe well and that barrier electronic conduction can be neglected, we were able to focus our attention on the transport properties of the quantum well alone. Thus the carrier density in the quantum wells could be calculated directly from the Hall coefficient and the well width. Also, the Seebeck coefficient of the wells was equal to the measured S of the MQW sample. For each sample, the value of the well S^2n was obtained and the results are shown as full circles in Fig. 7-7. Fig. 7-7(a) shows the results as a function of well thickness, and Fig. 7-7(b) shows S^2n as a function of carrier density. This shows that the optimum doping for the superlattices is about 10^{19} cm^{-3}; the optimum increases slightly with decreasing well thickness. The corresponding results for bulk single crystal PbTe obtained from Ref. [27] are also shown on these plots. The data points in Fig. 7-7(a) show an increase in S^2n as

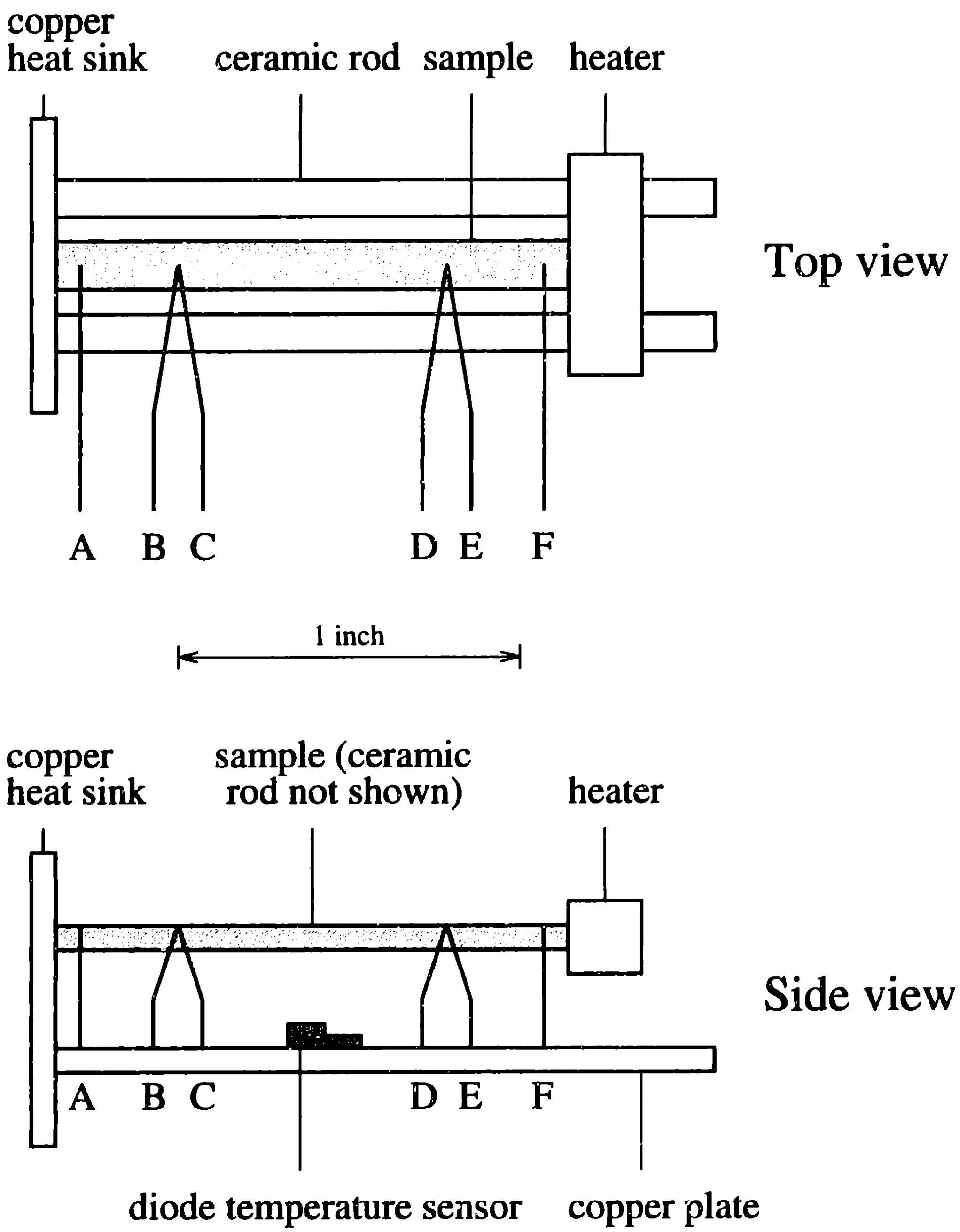

Figure 7-5: Experimental setup for measuring σ and S of superlattice samples.

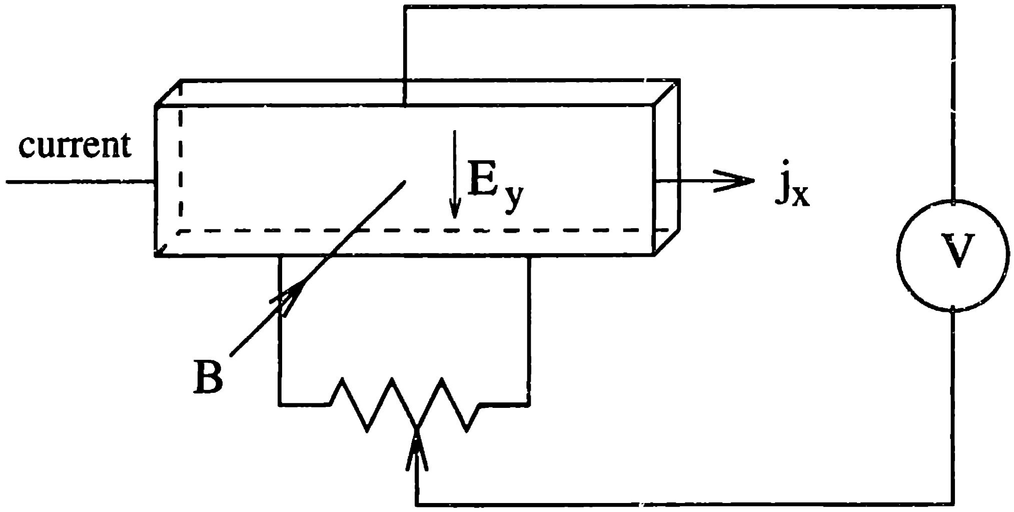

Figure 7-6: Arrangement of current and potential leads to the sample for Hall coefficient measurements.

the well width is narrowed, and the well S^2n may reach as much as four times the bulk value for small well widths. This result is predicted by the theoretical model and therefore gives qualitative support to the idea that MQW structures may be used to improve Z over bulk values. To obtain a quantitative comparison between experiment and theory, I used my model to calculate values of S^2n vs a and vs n for the $Pb_{0.927}Eu_{0.073}Te$ MQW system as described below.

In the original model (Chapter 4), I considered a quantum well in which only a single subband contributes to the transport and to Z. However, in a PbTe quantum well there are two sets of subbands which may contribute to the transport, arising from the four degenerate carrier pockets at the L points of the Brillouin zone in bulk cubic PbTe which have their main axes along the <111> directions as shown in Fig. 7-8. Since growth occurs along the [111] direction, one set of subbands is associated with the pocket along the [111] axis and has a circle as a surface of constant energy in the (k_x,k_y) plane. These are the longitudinal subbands. The other three pockets, with their main axis oriented obliquely to the [111] growth direction, yield three ellipses as surfaces of constant energy in the two-dimensional case [23]. Even though the Fermi level may lie just above the lowest energy conduction band subband, which is a longitudinal one, the oblique subbands may still contribute significantly to S^2n

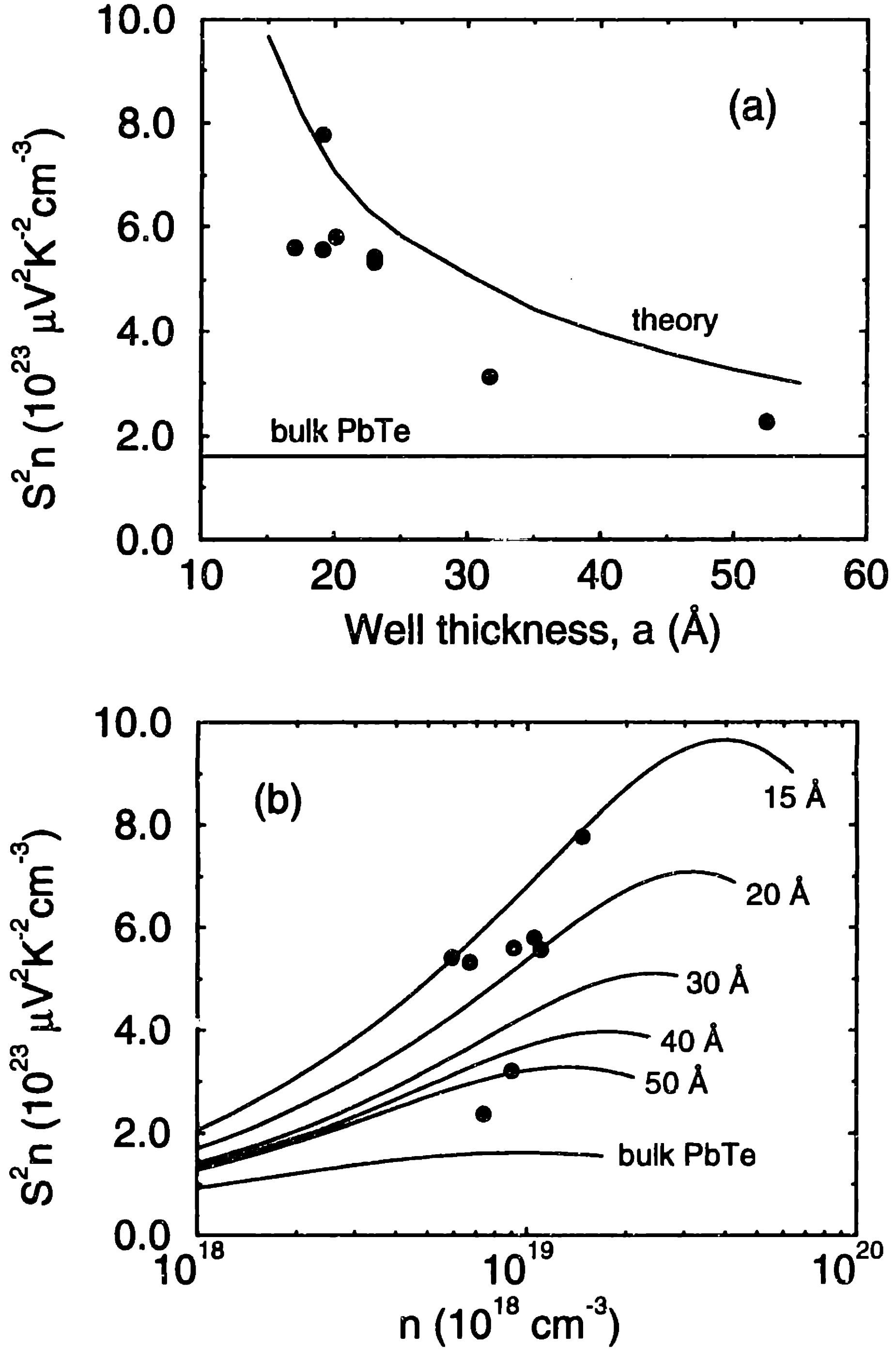

Figure 7-7: (a) Experimental S^2n results for PbTe/Pb$_{0.927}$Eu$_{0.073}$Te MQWs (full circles) as a function of well width a at 300 K. For comparison, the best experimental bulk PbTe value is also shown. Calculated results for optimum doping using the model are shown as a solid line. (b) Experimental S^2n results for the same PbTe/Pb$_{0.927}$Eu$_{0.073}$Te MQW samples (full circles) as a function of carrier density n at 300 K. Calculated results using my model for different well widths are shown as solid lines.

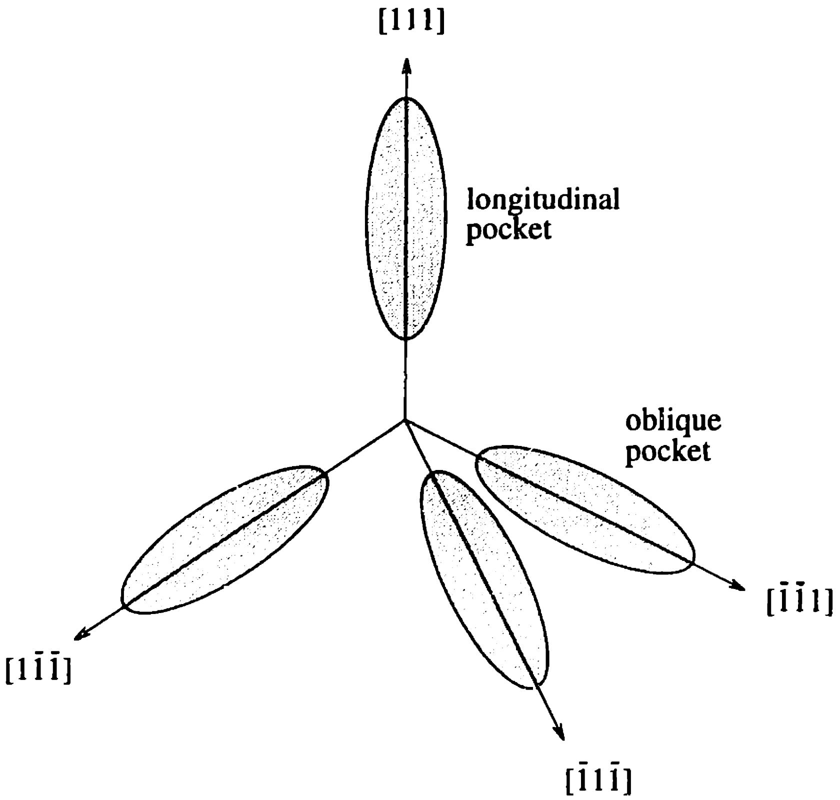

Figure 7-8: Carrier pockets in PbTe.

even though they are further from the Fermi level since they have a much higher density of states. Thus, to do a realistic calculation of the transport properties of PbTe quantum wells, it is necessary to know the relative energies of all four subband extrema and then to include all subbands in calculating the overall S and n.

7.5 Envelope Function Approximation

The Envelope Function Approximation (EFA) was used to calculate the positions of the energy levels in the MQW structures. The EFA calculation involves solving for the bulk electron eigenstates in both the well and barrier materials separately, then matching the wavefunctions at the interface with appropriate boundary conditions to find the energy levels and dispersion relations in the quantum well [28]. Yuan *et al.* [23] applied the EFA method to the PbTe/$Pb_{1-x}Eu_xTe$ MQW system with great success and used it to reproduce their experimental optical data, without any fitting parameters.

The effective mass Hamiltonian for bulk PbTe or bulk $Pb_{0.927}Eu_{0.073}Te$ [1] is given by [23]:

$$H = \begin{bmatrix} h_{cc} & h_{cv} \\ h_{vc} & h_{vv} \end{bmatrix} \tag{7.1}$$

where

$$h_{cc} = \left\{ E_c + \frac{\hbar^2(k_1^2 + k_2^2)}{2m_t^-} + \frac{\hbar^2 k_3^2}{2m_l^-} \right\} \begin{bmatrix} 1 & 0 \\ 0 & 1 \end{bmatrix}, \tag{7.2}$$

$$h_{vv} = \left\{ E_v - \frac{\hbar^2(k_1^2 + k_2^2)}{2m_t^+} - \frac{\hbar^2 k_3^2}{2m_l^+} \right\} \begin{bmatrix} 1 & 0 \\ 0 & 1 \end{bmatrix}, \tag{7.3}$$

$$h_{cv} = h_{vc} = \begin{bmatrix} P_l k_3 & P_t(k_1 - ik_2) \\ P_t(k_1 + ik_2) & -P_l k_3 \end{bmatrix}, \tag{7.4}$$

with $k_i = -i\partial/\partial r_i$, where r_i is in the pocket coordinate system. E_c and E_v denote the conduction and valence band edges, and P_l and P_t denote the longitudinal and transverse momentum matrix elements.

The Schrödinger equation

$$\sum_{b'} H_{bb'} f_{b'} = E f_b, \tag{7.5}$$

with $b, b' = 1, 2, 3, 4$, is a set of couple differential equations. By extending the EFA to an MQW superlattice, the material parameters become position dependent. At the interfaces, they will change abruptly. The solutions of Eq. (7.5) in each layer have to be joined at the interfaces.

The appropriate conditions are obtained by integrating Eq. (7.5) along the z-direction (superlattice growth direction) across an interface,

$$\int_{z^-}^{z^+} dz(H - E)f_b = 0, \tag{7.6}$$

---

[1] The bandstructures of PbTe and $Pb_{1-x}Eu_xTe$ are similar for small x [23].

yields the four conditions

$$f_b(z^-) = f_b(z^+), \tag{7.7}$$

where $b = 1, 2, 3, 4$ and z^-, z^+ are the coordinates at opposite sides of the interface. Since Eq. (7.5) contains second-order derivatives, conditions for joining the derivatives of f_b are necessary for specifying the solution to Eq. (7.5) uniquely. However, it turns out that the conditions for joining the derivatives are of negligible influence [29]. The periodicity in the z-direction, D, implies

$$f_b(z + D) = \exp(iKD) f_b(z), \tag{7.8}$$

with a superlattice Bloch vector K, $-\pi/D < K \leq \pi/D$, which defines a superlattice Brillouin zone.

In IV-VI materials, the effects of charge transfer (mobile carriers) across the interfaces do not cause substantial electric potentials due to the enormously high dielectric constants [28]. In this case, i.e., piecewise constant material parameters, the solutions to Eq. (7.5) in each layer are plane waves with wave vectors **k**. Due to the continuity conditions Eq. (7.7), the components of k vectors in the x-y plane have to be the same in each layer of the MQW superlattice. Thus, we obtain the quantum numbers k_x, k_y, and K characterizing the solution of the Schrödinger equation an a MQW superlattice. In each layer, the energy dependence on arbitrary k_x, k_y and k_z is obtained from Eq. (7.5). Solving this equation for k_z gives a polynomial of degree 4, the coefficients of which will depend on k_x, k_y and E. Of the four possible solutions for k_z, only the smallest two are reasonable within the framework of the EFA [28]. Thus, in each layer, we have two evanescent or propagating waves in the z-direction. The general solution to Eq. (7.5) in each layer is a linear combination of the two spin orientations and the two k_z values, defining four amplitudes for each layer. The superlattice dispersion relation $E(K, k_x, k_y)$ is determined as follows. The four continuity [Eq. (7.7)] and periodicity [Eq. (7.8)] conditions yield the eight conditions for the four amplitudes in both layers defining an 8×8 system of homogeneous equations. In order to have a nontrivial solution, the coefficient determinant has to vanish. From

Eq. (7.5), we obtain

$$\begin{bmatrix} f_3 \\ f_4 \end{bmatrix} = -(h_{vv} - E)^{-1} h_{cv} \begin{bmatrix} f_1 \\ f_2 \end{bmatrix} \tag{7.9}$$

where according to the spin state either f_1 or f_2 is chosen to be zero. The wave vectors are transformed from the superlattice coordinate system (x, y, z) to the pocket axis system (1, 2, 3) via the orthogonal transformation

$$\begin{pmatrix} k_1 \\ k_2 \\ k_3 \end{pmatrix}_{A,B}^{\mathrm{I,II}} = M \begin{pmatrix} k_x \\ k_{y\mathrm{I,II}} \\ k_{zA,B} \end{pmatrix}. \tag{7.10}$$

A and B denote the two constituents and I and II denote the two solutions for k_z to a given k_x, k_y and E. Using Eq. (7.9) and taking the interfaces at $z = 0$, $z = d_A$ with the individual layer thicknesses d_A, d_B, the determinant reads

$$\begin{vmatrix} \mathrm{I} & \mathrm{I} & \mathrm{I} & \mathrm{I} \\ a\mathrm{I} & b\mathrm{I} & c\mathrm{I} & d\mathrm{I} \\ R & S & T & U \\ aR & bS & cT & dU \end{vmatrix} = 0. \tag{7.11}$$

I is the 2 × 2 unit matrix,

$$a = \exp(ik_{zA}^{\mathrm{I}} d_A), \tag{7.12}$$

$$b = \exp(ik_{zA}^{\mathrm{II}} d_A), \tag{7.13}$$

$$c = \exp(-ik_{zB}^{\mathrm{I}} d_B + iKD), \tag{7.14}$$

$$d = \exp(-ik_{zB}^{\mathrm{II}} d_B + iKD), \tag{7.15}$$

$$R = (H_{33}^{A,\mathrm{I}} - E)^{-1} \begin{bmatrix} P_l k_{3A}^{\mathrm{I}} & P_t(k_{1A}^{\mathrm{I}} - ik_{2A}^{\mathrm{I}}) \\ P_t(k_{1A} + ik_{2A}^{\mathrm{I}}) & -P_l k_{3A}^{\mathrm{I}} \end{bmatrix}, \tag{7.16}$$

$$S = (H_{33}^{A,\mathrm{II}} - E)^{-1} \begin{bmatrix} P_l k_{3A}^{\mathrm{II}} & P_t(k_{1A}^{\mathrm{II}} - ik_{2A}^{\mathrm{II}}) \\ P_t(k_{1A} + ik_{2A}^{\mathrm{II}}) & -P_l k_{3A}^{\mathrm{II}} \end{bmatrix}, \tag{7.17}$$

$$T = (H_{33}^{B,\mathrm{I}} - E)^{-1} \begin{bmatrix} P_l k_{3B}^{\mathrm{I}} & P_t(k_{1B}^{\mathrm{I}} - ik_{2B}^{\mathrm{I}}) \\ P_t(k_{1B} + ik_{2B}^{\mathrm{I}}) & -P_l k_{3B}^{\mathrm{I}} \end{bmatrix}, \tag{7.18}$$

$$U = (H_{33}^{B,\mathrm{II}} - E)^{-1} \begin{bmatrix} P_l k_{3B}^{\mathrm{II}} & P_t(k_{1B}^{\mathrm{II}} - ik_{2B}^{\mathrm{II}}) \\ P_t(k_{1B} + ik_{2B}^{\mathrm{II}}) & -P_l k_{3B}^{\mathrm{II}} \end{bmatrix}, \tag{7.19}$$

where H_{33} denotes the corresponding element of the Hamiltonian matrix of Eq. (7.5).

The zeros of this determinant define the solutions $E(K, k_x, k_y)$. The superlattice still has a center of inversion, and so the solutions obtained are doubly degenerate. For k_x and k_y equal to zero, one obtains

$$k_{z,A,B}^{\mathrm{II}} = -k_{z,A,B}^{\mathrm{I}}, \tag{7.20}$$

so that the superlattice dispersion is obtained from

$$\cos(KD) = -\frac{1}{2}\left(\frac{Q}{P} + \frac{P}{Q}\right) \sin(k_{zA} d_A) \sin(k_{zB} d_B) + \cos(k_{zA} d_A) \cos(k_{zB} d_B) \tag{7.21}$$

with

$$P = \frac{k_{3A}}{(H_{33}^A - E)}, \tag{7.22}$$

$$Q = \frac{k_{3B}}{(H_{33}^B - E)}. \tag{7.23}$$

The superlattice energy levels satisfy dispersion relation Eq. (7.21). Within each layer, the electrons also satisfy Eq. (7.5). For Eq. (7.5) to have a nontrivial solution, the coefficient determinant $|H - E|$ must vanish. This leads to

$$\begin{aligned} &\left(E_c + \frac{\hbar^2(k_1^2 + k_2^2)}{2m_t^-} + \frac{\hbar^2 k_3^2}{2m_l^-} - E\right)\left(E_v - \frac{\hbar^2(k_1^2 + k_2^2)}{2m_t^+} - \frac{\hbar^2 k_3^2}{2m_l^+ - E}\right) \\ &= P_t^2(k_1^2 + k_2^2) + P_l^2 k_3^2. \end{aligned} \tag{7.24}$$

To find the allowed superlattice energy levels, one proceeds in the following manner. Let $k_x = k_y = 0$ in Eq. (7.24) and find $k_z(E)$. Substitute this $k_z(E)$ in Eq. (7.21) to eliminate k_z. Now the right hand side of Eq. (7.21) is a function only of energy

E. On the left hand side $-1 < \cos(KD) < 1$, so this restricts the possible value of E and leads to the discrete energy levels of the superlattice.

For the longitudinal levels, the longitudinal axis of the carrier pocket is parallel to the z-axis of the superlattice, so one can choose

$$k_1 = k_x, \tag{7.25}$$

$$k_2 = k_y, \tag{7.26}$$

$$k_3 = k_z, \tag{7.27}$$

for use in Eq. (7.24). For the oblique levels, one can use Eq. (7.10) with

$$M = \begin{pmatrix} 1 & 0 & 0 \\ 0 & -1/3 & -2\sqrt{2}/3 \\ 0 & 2\sqrt{2}/3 & 1/3 \end{pmatrix} \tag{7.28}$$

to get

$$k_1 = k_x, \tag{7.29}$$

$$k_2 = -\frac{1}{3}k_y - \frac{2\sqrt{2}}{3}k_z, \tag{7.30}$$

$$k_3 = \frac{2\sqrt{2}}{3}k_y - \frac{1}{3}k_z, \tag{7.31}$$

for one oblique pocket, and similarly for the other two oblique pockets.

To use the EFA method for the PbTe/$\mathrm{Pb}_{1-x}\mathrm{Eu}_x\mathrm{Te}$ system, the band gaps, band offsets, interband momentum matrix elements and far band parameters for both bulk PbTe and bulk $\mathrm{Pb}_{1-x}\mathrm{Eu}_x\mathrm{Te}$ must be known. The band gap of PbTe is 319 meV at 300 K [24]. I determined the band gap for our $\mathrm{Pb}_{0.927}\mathrm{Eu}_{0.073}\mathrm{Te}$ barrier material to be 630 meV from infrared transmission measurements of thick film samples (Fig. 7-9). The band offsets were estimated by assuming the relation determined experimentally by Yuan *et al.* [23]: $\Delta E_c/\Delta E_g = 0.55$, where ΔE_c is the conduction band offset and ΔE_g is the difference in band gap between the well and barrier materials, giving

	E_g (meV)	$2P_t^2/m_0$ (eV)	P_t/P_l	m_t^-/m_0	m_l^-/m_0	m_t^+/m_0	m_l^+/m_0
PbTe	319	6.02	3.42	0.060	0.505	0.102	0.920
$Pb_{0.927}Eu_{0.073}Te$	630	8.23	3.86	0.060	0.505	0.102	0.920

Table 7.1: Band parameters used for bulk PbTe and bulk $Pb_{0.927}Eu_{0.073}Te$. The effective masses were obtained from Ref. [23].

the offsets shown in Fig. 7-1. Finally, the momentum matrix elements and far band parameters were obtained from Ref. [23]; these values are shown in Table 7.1. The positions of the quantum well energy levels in the conduction and valence bands were thus obtained for several of our samples, and the results for a sample with a 53 Å well and a sample with a 20 Å well are shown as insets in Fig. 7-10(a) and Fig. 7-10(b), respectively.

7.6 Infrared transmission measurements

For an experimental check of my calculations, I did infrared transmission measurements (using a UV-vis machine) on the same 53 Å well and 20 Å samples and the results are shown in Fig. 7-10. Transmission was measured relative to the BaF_2 substrate. Yuan *et al.* [23] showed that for the $PbTe/Pb_{1-x}Eu_xTe$ MQW system, there is a significant decrease in transmission when the incident energy equals the energy for the interband transition from the lowest oblique subband in the valence band to the lowest oblique subband in the conduction band, the $(1\text{-}1)^o$ transition. For the two samples shown in Fig. 7-10, the lowest oblique subband is the second subband in both the conduction and valence bands. Figure 7-10 shows that for both samples, there is a steplike decrease in transmission at an energy almost exactly at that calculated for the $(1\text{-}1)^o$ transition (see inset). The transition occurs at about 470 meV for the 53 Å well sample and at about 580 meV for the 20 Å well sample. For both samples, the transmission goes to zero (over an energy range k_BT) at about 630 meV, which corresponds to the band gap of the barrier. It is very difficult to

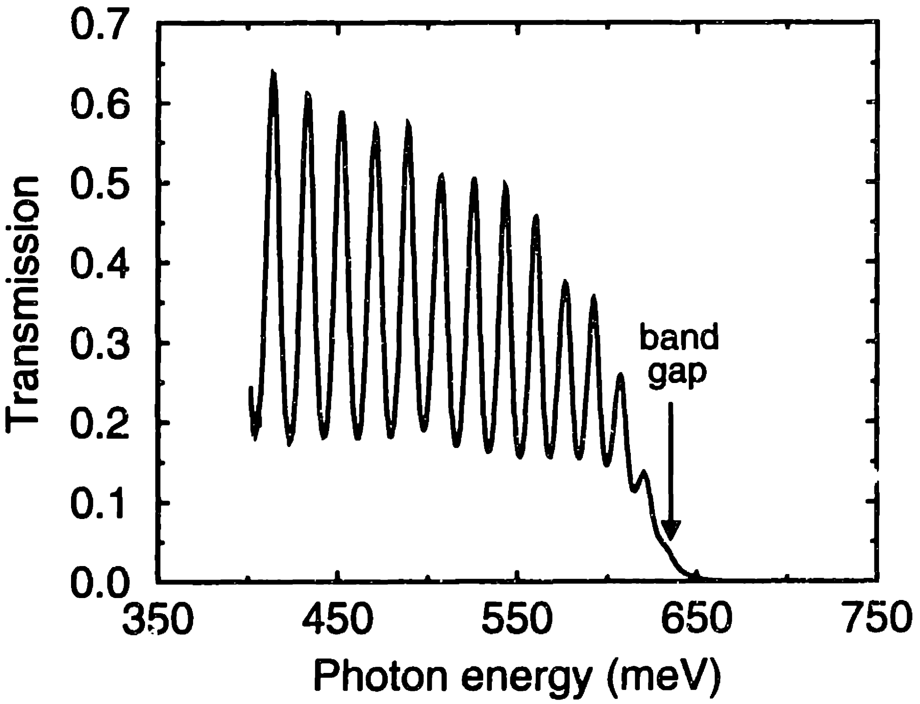

Figure 7-9: Transmission vs frequency at 300 K for a 5.4 μm $Pb_{0.927}Eu_{0.073}Te$ thick film. For incident photon energy below the band gap, the sample transmits IR radiation and interference fringes result between transmitted and reflected waves. Above the band gap, the transmission goes to zero; the falloff occurs over an energy range k_BT.

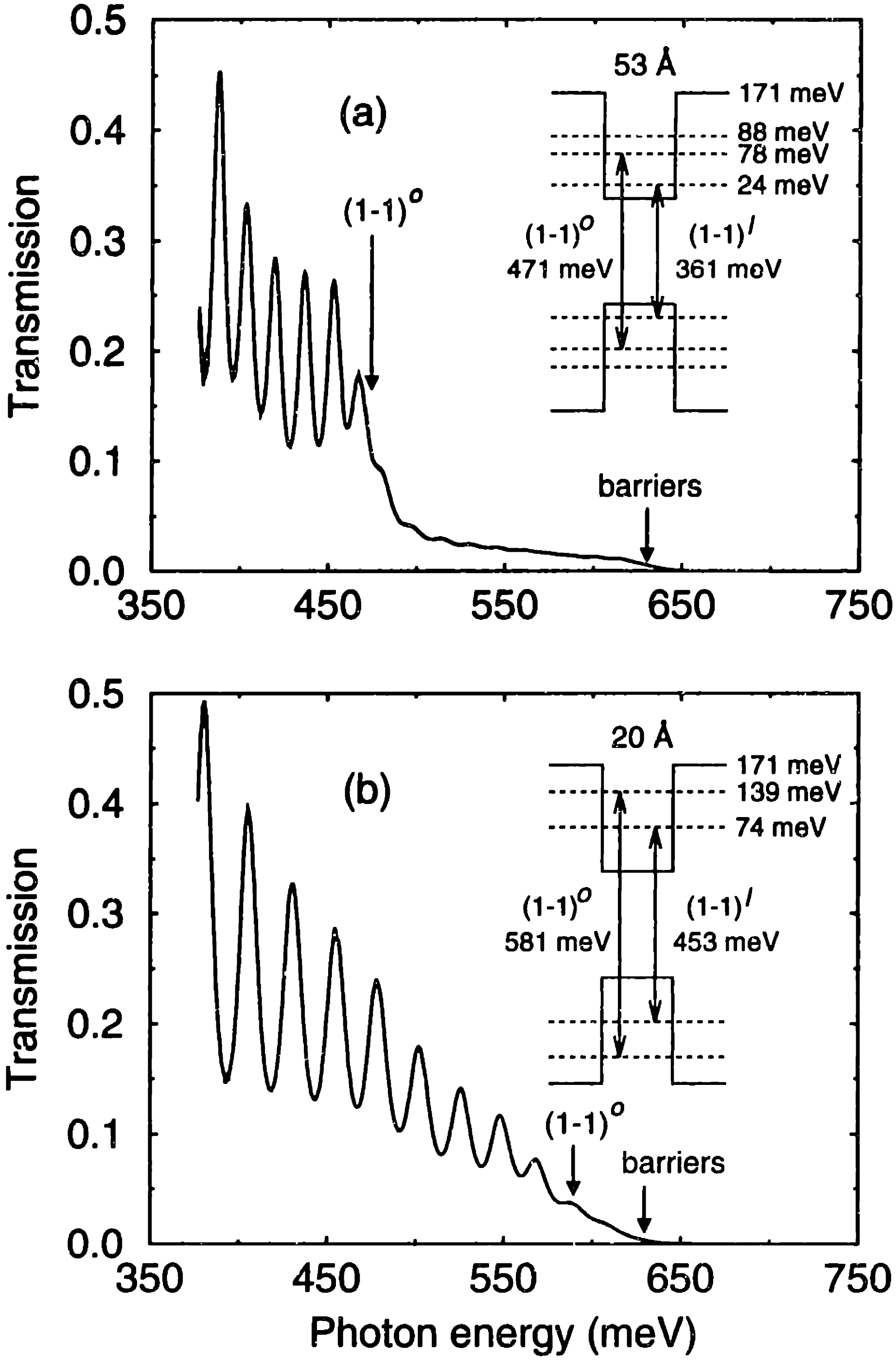

Figure 7-10: Transmission vs frequency at 300 K for (a) a MQW sample with a 53 Å well and a 560 Å barrier and (b) a MQW sample with a 20 Å well and a 430 Å barrier. Insets show the results of EFA calculations of the quantum well energy levels and the interband transition energies.

observe the $(1\text{-}1)^l$ transition between the first longitudinal subbands in the valence and conduction bands because the longitudinal subbands have a very low density of states, much lower than that for the oblique subbands [23]. The very good agreement between the infrared transmission results and the EFA calculations confirm that EFA calculations can be used to determine the positions of the subband energy levels in our samples. The calculations also show very little dispersion in the direction normal to the layers, which is expected for 2D transport.

7.7 Comparison of transport results with theory

Once I had calculated the positions of the energy levels in the quantum wells, the next step was to calculate values for the Seebeck coefficient and carrier density within the framework of the theoretical model, using expressions for the Seebeck coefficient S_i and carrier density n_i of the i-th subband (Eqs. (4.18) and (4.17) given by:

$$n_i = \frac{1}{2\pi a}\left(\frac{2k_BT}{\hbar^2}\right)(m_1m_2)^{\frac{1}{2}}F_0(\zeta_i^*) \tag{7.32}$$

$$S_i = -\frac{k_B}{e}\left(\frac{2F_1(\zeta_i^*)}{F_0(\zeta_i^*)} - \zeta_i^*\right) \tag{7.33}$$

where the Fermi-Dirac function F_j is given by

$$F_j(\zeta_i^*) = \int_0^\infty \frac{x^j dx}{e^{(x-\zeta_i^*)}+1}, \tag{7.34}$$

a is the width of the quantum well, m_1 and m_2 are the principal effective mass components parallel to the layers, $\zeta_i^* = (\zeta - E_i)/k_BT$ is the reduced Fermi level measured relative to E_i, the minimum energy of each subband (calculated using the EFA method), and ζ is the Fermi level. For multiple subbands, we use the expressions (3.1) and (3.2) with each $\mathbf{L}^{(\alpha)}$ replaced by the sum of contributions from each subband. This leads to the following expressions for the total carrier density (n) and Seebeck coefficient (S), assuming all subbands to have the same mobility as a first approximation and for lack of better experimental knowledge.

$$n = \sum_i n_i, \tag{7.35}$$

$$S = \frac{\sum_i S_i n_i}{\sum_i n_i}. \tag{7.36}$$

For the S and n calculations, a constant barrier thickness of 460 Å was used, which is the average thickness of all our samples shown in Fig. 7-7. Calculations were done for different well thicknesses varying from 15 Å to 50 Å. Since parabolic bands were assumed for the transport calculations, the effective masses were extracted from the two-band momentum matrix elements P_l and P_t in Table 7.1 [23] using the relations

$$\frac{m_{\|}}{m_0} = \frac{E_g m_0}{2P_l^2}, \tag{7.37}$$

$$\frac{m_{\perp}}{m_0} = \frac{E_g m_0}{2P_t^2}. \tag{7.38}$$

For PbTe, this gave a bulk longitudinal effective mass $m_{\|} = 0.620m_0$ and a bulk transverse effective mass $m_{\perp} = 0.053m_0$. For the 2D quantum well, this gives $m_1 = m_2 = m_{\perp}$ for the longitudinal subbands, and $m_1 = m_{\perp}$, $m_2 = 0.283m_0$ for the oblique subbands. For each well thickness, the EFA calculation was used to get the positions of the energy levels, E_i. S and n were then calculated as a function of Fermi level ζ and thus S and S^2n were found as a function of n. The calculated results of S^2n vs n for different well widths are shown as solid lines in Fig. 7-7(b). The calculated maximum S^2n for each well width (the peak of each curve in Fig. 7-7(b)) is shown vs well width as a solid line in Fig. 7-7(a), while Fig. 7-7(b) shows that the optimum doping increases as the quantum well width is decreased. As can be seen from Figs. 7-7(a) and 7-7(b), there is very good agreement between experiment and theory, especially considering that *no* adjustable parameters were used in the calculation. The theory predicts the observed variation of S^2n with carrier density n and also the variation of the optimum S^2n with well width a. Therefore the experimental results appear to confirm the predictions of my theoretical model, showing that MQW structures may indeed be used to obtain a high Z.

So far, I have considered only S and n since it is through these properties that the theory predicts an increase in Z. However, Z depends also on the thermal conductivity, κ. If we assume that the quantum well κ is the same as bulk κ, the experimental results in Fig. 7-7 imply that the quantum well Z may be up to 5 times greater than the bulk, giving a value of $ZT = 2.0$ at 300 K, twice the value of the best bulk thermoelectric materials. However, this value is for the quantum well alone, and even though all of the electronic transport is in the quantum well, the barrier layers do contribute to the total lattice thermal conductivity. Due to the thick barriers, this will make the overall Z of the MQW structures about a factor of 20 less than the well values alone if we assume that the $Pb_{0.927}Eu_{0.073}Te$ has the same κ as bulk PbTe. It is likely, however, that due to alloy [30] and interface scattering, the barrier κ is significantly less than the bulk value, in which case the overall Z may be close to a useful value, even with thick barriers. Recent experimental [31, 32] and theoretical results [33] appear to confirm a reduction in κ in superlattices compared to the constituent bulk materials. Work is underway to measure κ of our MQW samples to determine the overall Z. In general, it is difficult to measure κ for thermoelectric thin films since κ is very low, leading to significant errors due to heat loss. Also, κ of the substrate is often much greater than that of the film, leading to another source of difficulty. Although we have needed wide barriers to ensure 2D well transport, it may be possible to increase the barrier Eu content to give a higher band gap so that thinner barriers can be used to confine the electrons in the wells. Graded barrier layers, with high values of x in the middle of the layer and lower values of x close to the interface, may have to be used to avoid lattice mismatch problems.

7.8 Temperature dependence

All the measurements and calculations so far have been for 300 K. For thermoelectric cooling applications, it may be interesting to see how our superlattice samples behave in the temperature range from 300 K down to 4 K. By placing the specimen enclosure in a cryostat, I have done several temperature-dependent measurements of σ and S

from 300 K down to 4 K. Two superlattice samples and a single 13 μm layer of bulk PbTe were measured and the results are shown in Figs. 7-11 and 7-12. The resulting power factor temperature dependence is shown in Fig. 7-13. The theory derived in this thesis makes no predictions about temperature dependence since it assumed a constant relaxation time τ. Also, at lower temperatures the relaxation time approximation is no longer valid [4]. However, some general points may be noted. As T is decreased, both the superlattice and bulk samples show an increase in σ and a decrease in S typical of doped semiconductors [2]. σ for the thick film sample is lower than σ for both the superlattices samples at 300 K, but increases much more rapidly than the superlattice samples as the temperature is decreased, becoming higher than σ for both the superlattice samples at about 110 K. This can be explained by the presence of interface dislocations in the superlattice samples causing their mobility and hence σ at low temperatures to be much lower the thick film sample, which has many fewer defects. At higher temperatures, the mobility and σ of the superlattices is comparable to bulk since the mobility no longer limited by defects but by phonon scattering as PbTe has a Debye temperature of 136 K [34]. There is not as much difference in the between the bulk and superlattice samples in the temperature dependence of S. This is because as shown in Eqs. (3.24) and (4.18), there is no mobility dependence in S, so it is less affected by changes in the scattering mechanism.[2] The results in Fig. 7-13 also suggest that PbTe superlattices may be more useful at temperatures higher than 300 K than at room temperature.

7.9 Conclusions

The experimental results presented in this chapter are in good agreement with my calculations, confirming my theoretical model which predicts an increase in Z in MQW superlattices. This thesis shows that superlattices may indeed be used to attain an enhanced thermoelectric figure of merit.

---

[2] Significant changes in the scattering mechanism will, however, invalidate the relaxation-time approximation used to derive Eqs. (3.24) and (4.18).

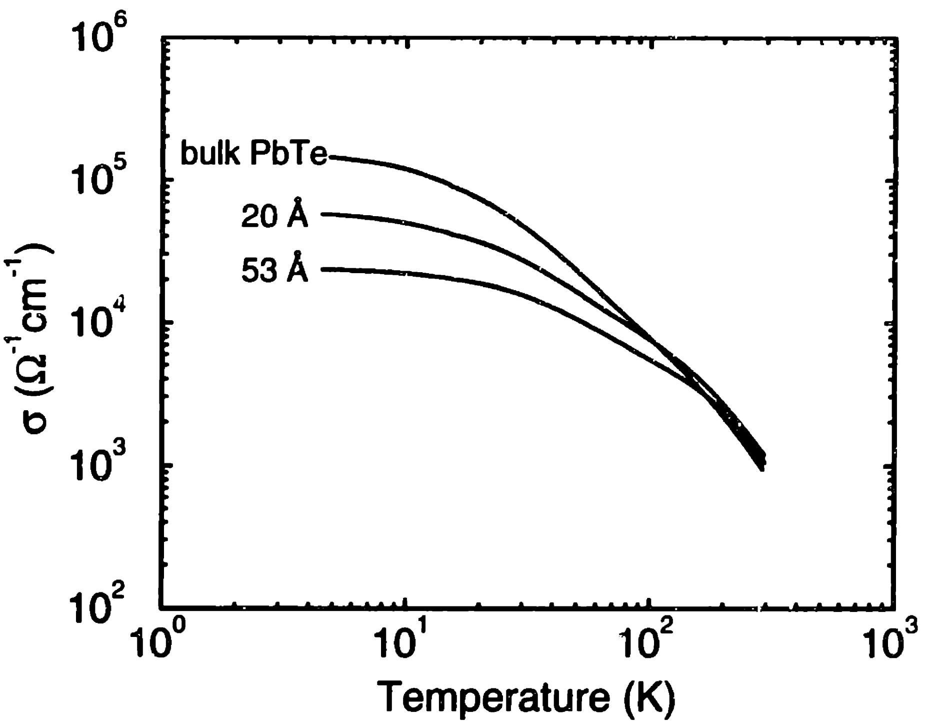

Figure 7-11: Electrical conductivity temperature dependence for PbTe/$Pb_{1-x}Eu_xTe$ superlattice samples and a 13 μm bulk PbTe film.

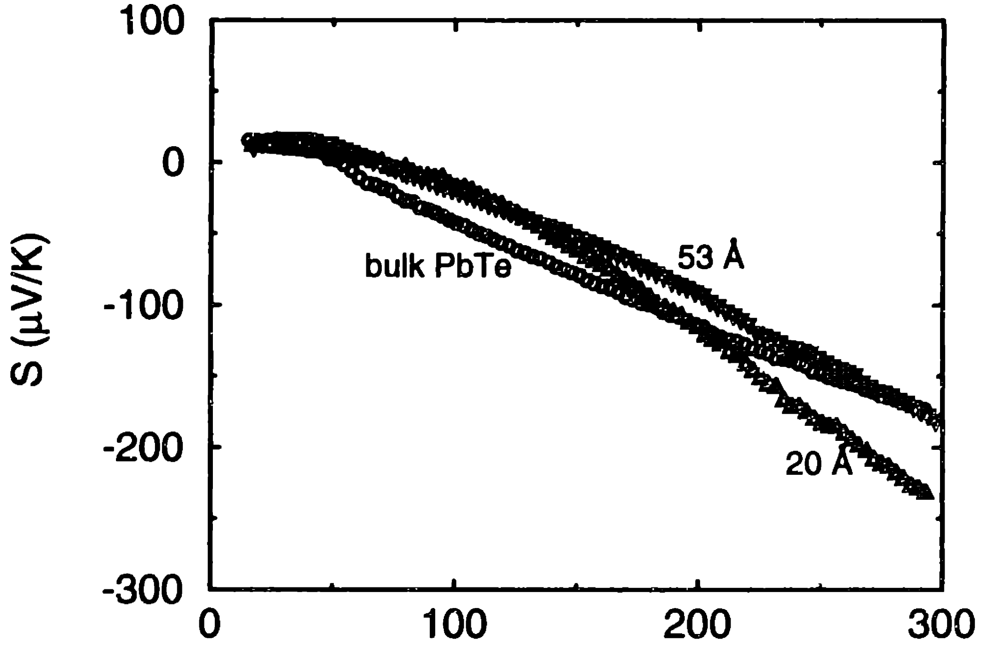

Figure 7-12: Seebeck coefficient temperature dependence for PbTe/$Pb_{1-x}Eu_xTe$ superlattice samples and a 13 μm bulk PbTe film.

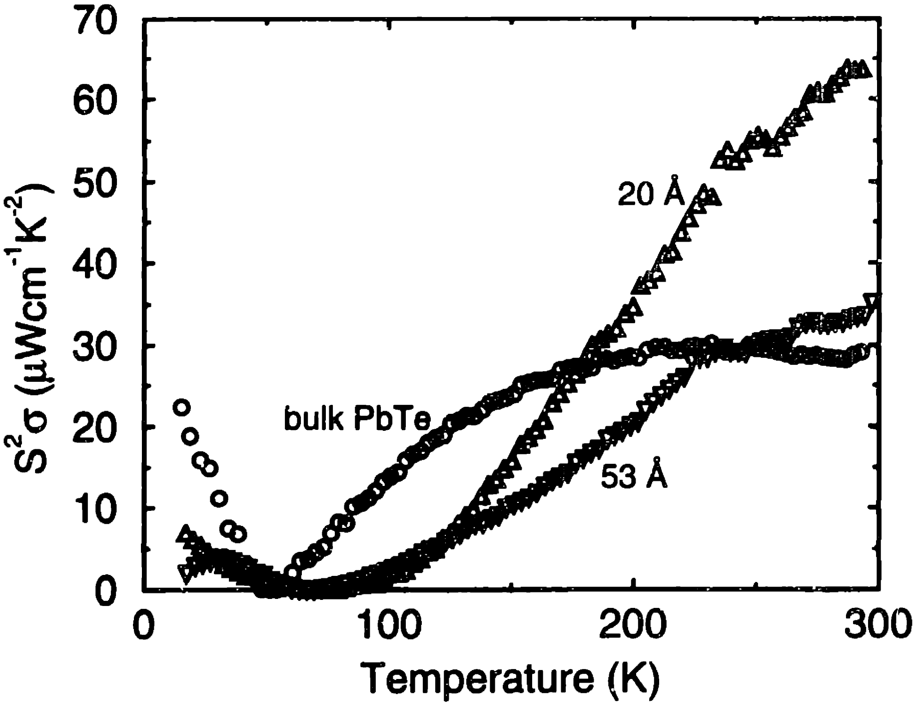

Figure 7-13: Power factor ($S^2\sigma$) temperature dependence for PbTe/Pb$_{1-x}$Eu$_x$Te superlattice samples and a 13 μm bulk PbTe film.

7.10 Future directions

In this thesis I have predicted an increase in Z in MQW superlattices and experimentally verified my theory. However, some work still needs to be done before superlattices can be used in thermoelectric applications.

- A method must be developed for an accurate measurement of the thermal conductivity.

- The contribution of the barrier material in PbTe/Pb$_{1-x}$Eu$_x$Te superlattices may need to be reduced to increase the overall Z. This may be done by increasing the Eu content x which will increase the barrier height allowing thinner barrier layers to be used which will still confine electrons in the quantum well. In order to avoid lattice mismatch problems caused by the increased x, graded barrier layers will have to be used, with a high x value in the middle region of the barrier and lower x values in the barrier region close to the interface.

- Although PbTe/$Pb_{1-x}Eu_xTe$ superlattices proved to be a good system to test the theory, Bi or $Bi_{1-x}Sb_x$ superlattice are still the ideal system for obtaining a high Z for applications. A suitable barrier material, however, needs to be found for the $Bi_{1-x}Sb_x$ system.

Bibliography

[1] A. F. Ioffe, in *Semiconductor Thermoelements and Thermoelectric Cooling*, chapter 1, (Infosearch, London, 1957).

[2] H. J. Goldsmid, *Thermoelectric Refrigeration* (Plenum, New York, 1964).

[3] S. B. Horn, in *Proceedings of the 1st National Thermogenic Cooler Conference*, (Center for Night Vision and Electro-Optics, Fort Belvoir, 1992).

[4] N. W. Ashcroft and N. D. Mermin, in *Solid State Physics*, chapter 13, (Saunders College, Philadelphia, 1976).

[5] H. H. Landolt and R. Börnstein, in *Numerical Data and Functional Relationships in Science and Technology*, pages 272–278, (Springer-Verlag, Berlin, 1983), Vol. 17f.

[6] J. P. Fleurial. Invited talk at American Physical Society meeting in St. Louis, MO, March 1996.

[7] J. George and B. Pradeep, Solid State Commun. **56**, 117 (1985).

[8] U. Meirav, M. A. Kastner, M. Heiblum, and S. J. Wind, Phys. Rev. B **40**, 5871 (1989).

[9] R. S. Ruoff, D. C. Lorents, B. Chan, R. Malhotra, and S. Subramoney, Science **259**, 346 (1993).

[10] P. M. Ajayan and S. Iijima, Nature **361**, 333 (1993).

[11] C. W. J. Beenakker and A. A. M. Staring, Phys. Rev. B **46**, 9667 (1992).

[12] G. Kirczenow, Phys. Rev. B **46**, 1439 (1992).

[13] C. F. Gallo, B. S. Chandrasekhar, and P. H. Sutter, J. Appl. Phys. **34**, 144 (1963).

[14] J. M. Berroir, Y. Guldner, J. P. Vieren, M. Voos, and J. P. Faurie, Phys. Rev. B **34**, 891 (1986).

[15] D. Schiferl and C. S. Barrett, J. Appl. Crystallogr. **2**, 30 (1969).

[16] M. S. Dresselhaus, in *The Physics of Semimetals and Narrow-Gap Semiconductors*, pages 16–17, edited by D. L. Carter and R. T. Bate (Pergamon, Oxford, 1971).

[17] R. T. Isaacson and G. A. Williams, Phys. Rev. B **185**, 682 (1969).

[18] G. A. Saunders and Z. Sümengen, Proc. R. Soc. London Ser. A **329**, 453 (1972).

[19] D. L. Partin, J. Heremans, D. T. Morelli, C. H. Olk C. M. Thrush, and T. A. Perry, Phys. Rev. B **38**, 3818 (1988).

[20] S. C. Shin, J. E. Hilliard, and J. B. Ketterson, Thin Solid Films **111**, 323 (1984).

[21] N. B. Brandt, S. M. Chudinov, and V. G. Karavaev, Sov. Phys. JETP **34**, 368 (1972).

[22] T. Yazaki, J. Phys. Soc. Jpn. **1054**, 25 (1968).

[23] S. Yuan, G. Springholz, G. Bauer, and M. Kriechbaum, Phys. Rev. B **49**, 5476 (1994).

[24] S. Yuan, H. Krenn, G. Springholz, and G. Bauer, Phys. Rev. B **47**, 7213 (1993).

[25] G. Springholz, G. Ihninger, G. Bauer, M. M. Olver, J. Z. Pastalan, S. Romaine, and B. B. Goldberg, Appl. Phys. Lett. **63**, 2908 (1993).

[26] T. C. Harman. Unpublished.

[27] T. C. Harman, D. L. Spears, and M. J. Manfra. Submitted to J. Electron. Mater.

[28] M. Kriechbaum, P. Kocevar, H. Pascher, and G. Bauer, IEEE J. Quantum Electron. **QE-24**, 1727 (1988).

[29] M. Kriechbaum, in *Solid State Sciences 67*, pages 120–129, (Springer, New York, 1986).

[30] S. Adachi, J. Appl. Phys. **54**, 1844 (1993).

[31] T. Yao, Appl. Phys. Lett. **51**, 1798 (1987).

[32] K. L. Wang. Private communication.

[33] G. Mahan. Invited talk at American Physical Society meeting in St. Louis, MO, March 1996.

[34] D. H. Parkinson and J. E. Quarrington, Proc. Phys. Soc. **67**, 569 (1954).